LOW FREQUENCY PLASMA INSTABILITY FOR THE GENERATION OF IONOSPHERIC IRREGULARITIES

By

TADAHIKO OGAWA

March 1972

Department of Electronics
Kyoto University
Kyoto, Japan

LOW FREQUENCY PLASMA INSTABILITY FOR THE GENERATION OF IONOSPHERIC IRREGULARITIES

By

TADAHIKO OGAWA

March 1972

Department of Electronics

Kyoto University

Kyoto, Japan

Doctoral Thesis

Abstract

In this thesis we describe a theoretical study of well-developed density irregularities in the ionosphere. Our interest is the formation mechanism of irregularities observed in sporadic E layers, auroral arcs, and plasma cloud experiments in the ionosphere and observed even in reflex arcs.

The ionosphere seems to be susceptible to a number of plasma instabilities. Now, it is well-known that among them a particular type of fluid-like plasma instability takes place in the lower ionosphere under certain conditions. One calls this instability by the name of cross-field instability.

By a linearized version, one found that the cross-field instability played an important role in producing of enhanced irregularities of electron concentration. Recent, rapid progress of measuring techniques by sounding rockets and radio-frequency scattering experiments, however, has disclosed quantitatively the fine structure of irregularities. Therefore, it is necessary to study the nonlinear evolution of the cross-field instability, in order to know the fine structure of the irregularities caused by the instability and to compare the theoretical results with the observed ones.

From a viewpoint of plasma physics, nonlinear cross-field instability presents an attractive example of wave-wave interactions which can lead to a large transport of the plasma.

The thesis consists of the following five chapters: In chapter 1, we review qualitatively the present status of the cross-field instability in linear and nonlinear regimes, and point out some relations between the theory and observation. Chapter 2 describes the time evolution of one-dimensional nonlinear cross-field instability. This work may be called an extension of previous works by other authors, in the sense that the instability condition is more strengthened than the previous ones. The cross-field instability is essentially two-dimensional phenomenon, judging from its physical picture. Thus, we study the time evolution of two-dimensional nonlinear cross-field instability as an initial-boundary value problem, in chapter 3. New appearances never seen in the one-dimensional model are recognized; the deformation of the background quantities which sustain the instability, and consequently the cyclic growth and decay of the instability. As an application of the cross-field instability to the auroral ionosphere, we present a new mechanism of quiet auroral arcs in chapter 4. It is suggested that the leading part of arc formation is played by the ionosphere. The theory basically consists of two stages: Firstly, it is shown that the ionosphere is subject to the cross-field instability resulting in a wavy irregularity of ionization whose characteristics are coincident with those of auroral arcs. Secondly, a model is presented that such an irregularity (arc-to-be) develops into auroral arcs under the influence of field-aligned current triggered by an induced potential across an arc-to-be. The model is numerically examined for a number of parameters sets to find that the ionospheric irregularity can certainly result in auroral arcs. The calculated results are compared with recent experiments of auroral arcs. Deformation of an arc is also discussed in terms of the cross-field instability.

Chapter 5 summarizes this thesis.

Contents

Acknowledgments

I would like to thank, from the bottom of my heart, Professor Susumu Kato for giving me constant guidance, many discussions, and suggestions throughout the work. I am deeply indebted to Dr. Tetsuya Sato who araised the interest in the relation between ionospheric irregularities and plasma physics, and had a long argument with me about this work. It would have been impossible to show this thesis without his help and stimulating discussions. I would like particularly to thank Professor Ken-ichi Maeda, Professor Toru Ogawa and Professor Iwane Kimura for their valuable suggestions and discussions. I was much enlightened on ionospheric electrodynamics by them.

I would like also to thank Professor Hiroshi Oya for his many suggestions and discussions on nonlinear wave-wave interactions and on electrodynamics in space. I am indebted to Dr. Kunitomo Sakurai, now at Goddard Space Flight Center of NASA, for his continual encouragement throughout the work.

I wish to acknowledge other staffs of Ionosphere Research Laboratory and Prof. Kimura's group for their discussions.

Numerical calculations in this work were performed by the digital computer (model FACOM 230-60) at the Data

Processing Center of Kyoto University.

Chapter 1

IONOSPHERIC IRREGULARITIES

and

CROSS-FIELD INSTABILITY

1. Introduction

A weakly ionized plasma is susceptible to a number of low frequency electrostatic instabilities. Of these we are here concerned with the cross-field instability, sometimes one called the "$\underset{\sim}{E} \times \underset{\sim}{B}$", "neutral drag", or "gradient drift" instability. It has been shown that this instability takes place in a weakly ionized plasma immersed in crossed electric and magnetic fields in the presence of a density gradient across the magnetic field. If the product of E by the density gradient is positive and if E exceeds a critical value, the energy dissipation by classical diffusion is overcome by the energy input to set up the instability. This instability is confirmed to occur in the ionosphere and in a reflex arc (for example, Sato, 1968; Hooper, 1970).

We here present the observed results of ionospheric irregularities and review the cross-field instability associated with density irregularities in a qualitative fashion, in order to know the present status. Attention is focused mainly on nonlinear behaviors of the instability which are of our concern.

II. Observations of Ionospheric Irregularities

We first present ionospheric density irregularities observed recently by sounding rockets, in order to clarify the objective of this study.

Smith(1966) observed structural features of the electron density profile of sporadic E in midlatitudes. These were obtained using the Langmuir probe having a resolution of about 10 m in height and about 1 % in electron density. Fig. 1.1 shows enlarged sections of electron density profiles by four rockets in daytime. The profile of 1513 CST shows very clearly an irregular region between 101.0 and 103.9 km. The relative amplitude in electron density is ± 18 % and the amplitude in height is about 0.4 km. Smith says that the sharpness of the boundaries of the region, the altitude of the center (102.5 km), and the thickness (2.9 km) strongly suggest an association with sporadic E.

Oya(1967) measured the micro-structure of the electron density profile by a rocket-borne gyro-plasma probe which has a resolution of about a few hundred meters in height and about ± 3 % in density. Fig. 1.2 shows detailed features of

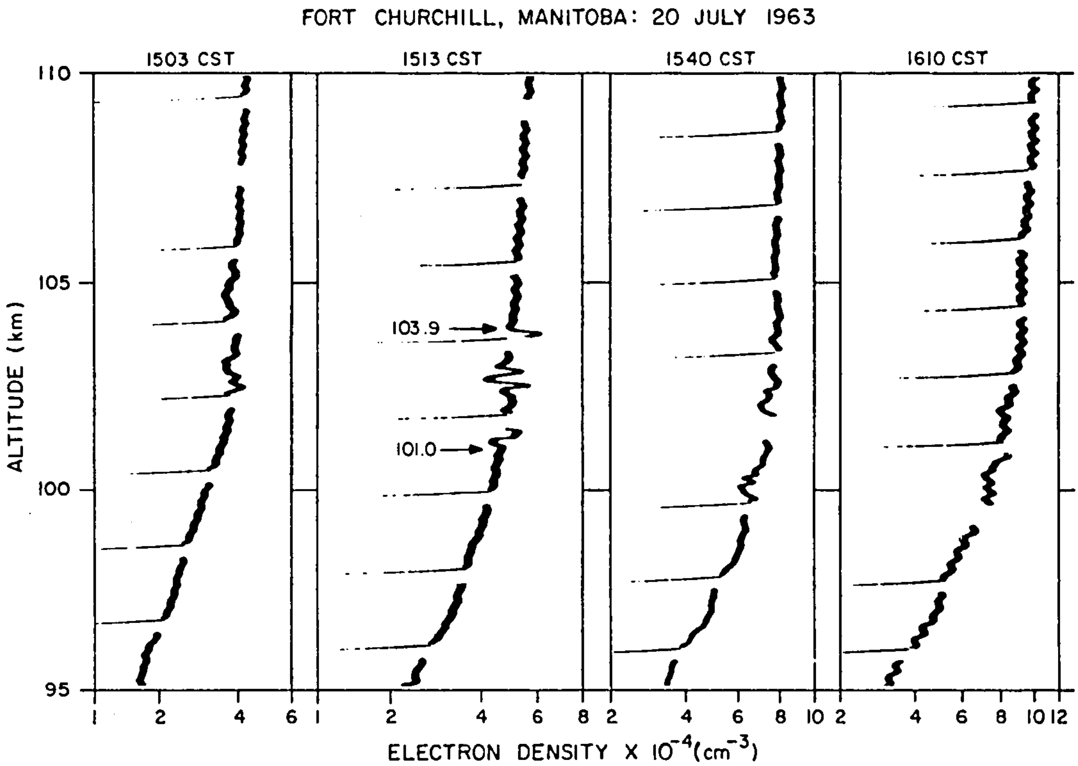

Fig. 1.1. Irregularities in electron density profiles, 20 July, 1963 (Smith, 1966). The regular small ripple is an effect of rocket spin.

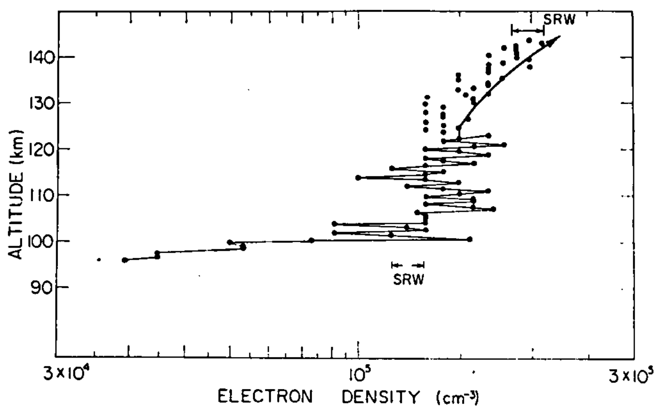

Fig. 1.2. Measured irregularity of electron density obtained at 1100 JST on December 5, 1966 at Uchinoura, Japan (Oya, 1967). SRW is the scattering range due to the wake effect of rocket motion.

the observed electron density in the daytime at midlatitudes. Note the density irregularity fluctuating within ± 20 % in the amplitude and having the altitude ranges of 100-120 km. This irregularity was identified with the radio scattering source of diffuse type sporadic E layer on the ionogram.

Prakash et al.(1970) revealed the existence of electron densities varying between 10^3 and 10^4 /cm^3 in the height ranges of 95-120 km. The observation by the Langmuir probe was done in the night time ionosphere near the geomagnetic equator, i.e., the night time equatorial E region. Fig. 1.3 shows the density profile obtained by Prakash et al.. They point out that the irregularities with scale sizes in the ranges of 30-300 m and 1-15 m and with their amplitudes varying by factors lying between 4 and 25 existed during the rocket flight. While these irregularities were found to occur randomly and in the form of bursts, most of them were observed in regions where the background electron density exhibits large negative gradients(see Fig. 1.3). Further they note that the positions of occurrence of the 30-300 m irregularities were found to regard qualitatively the cross-field instability under a background density gradient with a specific sign as a generation mechanism of irregularities, and that while the smaller scale size irregularities of 1-15 m also occur in regions where the cross-field instability can operate they cannot be directly explained on the basis

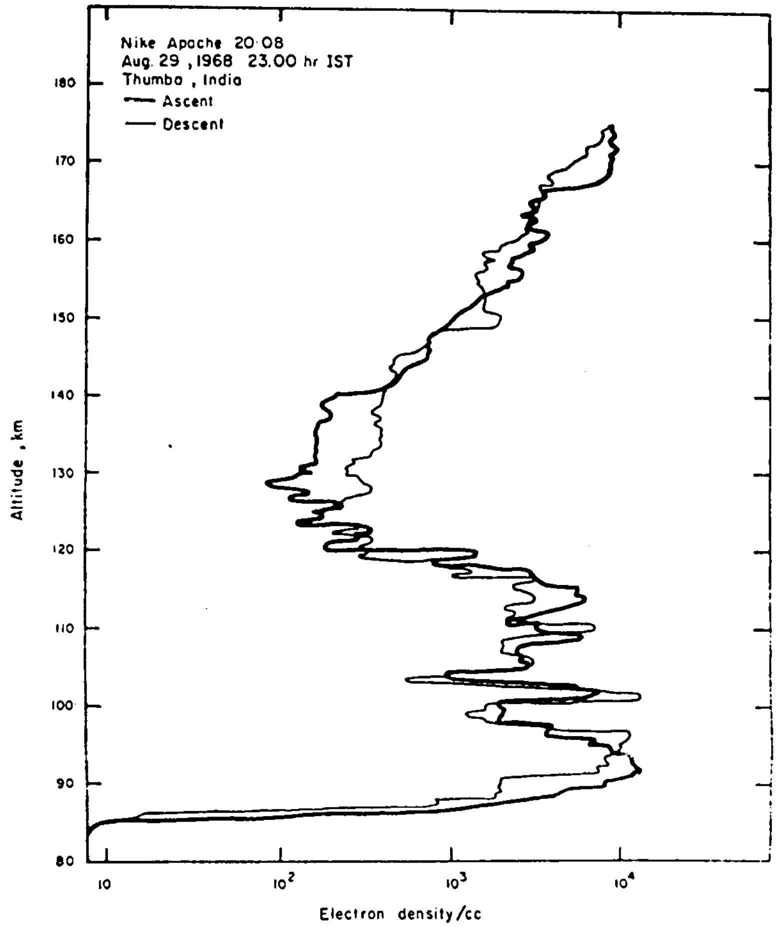

Fig. 1.3. Electron density profile obtained at 2300 IST on August 29, 1968 at Thumba, India (Prakash et al., 1970).

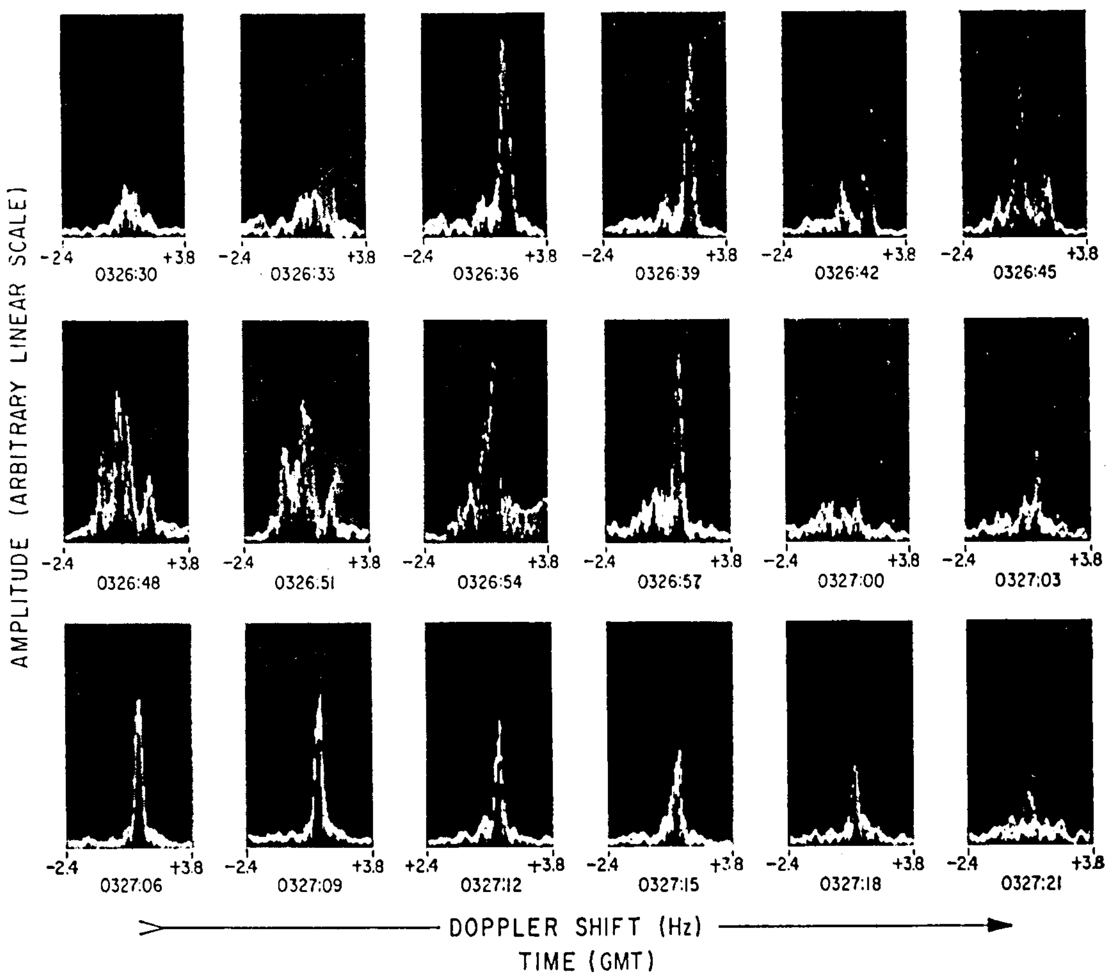

Fig. 1.4. Amplitude spectrum for typical low-altitude (87.5 km) cesium release (Davis, 1971).

of the present theories of the cross-field instability*).

Ionospheric irregularities as shown above may be, so to speak, produced by a freak of nature under certain ionospheric conditions. Now, however, we have another diagnostics of ionospheric plasmas by an active means, i.e., artificial plasma clouds. Davis(1971) described an attempt to study the circumstances under which the cross-field instability occur by injecting alkali plasma clouds into the lower E region and observing them with radio frequency scattering technique(coherent-pulse-Doppler radar). The typical example in appearance of plasma cloud evolution at lower extreme of the E layer is illustrated in Fig. 1.4 which shows a collection of spectral displays acquired by placing a 0.3 H_z resolution analysis filter at a succession of points in time, seperated by 3 sec each, during the lifetime of the plasma cloud. The first photograph, at o3h 26m 30s, in the figure shows the prerelease condition, with a small radar clutter echo just above zero apparent Doppler-shift. We see the rapid growth and subsequent decay of the spectrum, and coexisting discrete spectral components. Comparing with the nonlinear numerical calculations(for example, Sato and Tsuda, 1967),

---

*) We might, however, infer that even such small irregularities could be produced by the well developed cross-field instability at nonlinear stage, as will be seen in chapter 4.

Davis finds that the cross-field instability can indeed explain the observed behavior of the plasma cloud evolution.

Thus, we can suppose observationally that the cross-field instability plays an important role in the formation of ionospheric irregularities. We remind here that further nonlinear analysis of the instability would give a stronger support.

We have described above the observed results of irregularities at the equatorial and midlatitude ionosphere. Let us extend our consideration to the auroral ionosphere where the dynamical display, i.e., aurora is seen. Aurora is a complex, mixed-up phenomenon in spite of its simple visibility, and was treated as a challenging problem by many authors. However, many problems remain to be unsolved as yet. This may be due to the fact that the auroral ionosphere is closely linked with the entire magnetosphere by the lines of force,thereby exchanging informations each other. Therefore, it is very difficult to explain the auroral phenomena by a unified theory. Before this will be achieved, we must accumulate more observational and theoretical works.

As one step to this end, we confine ourselves to the electrodynamic coupling between the auroral ionosphere and the magnetosphere, in magnetically quiet times which may mean the quiet magnetosphere. Recent, important finding by sounding rocket penetrating auroral arcs which are often

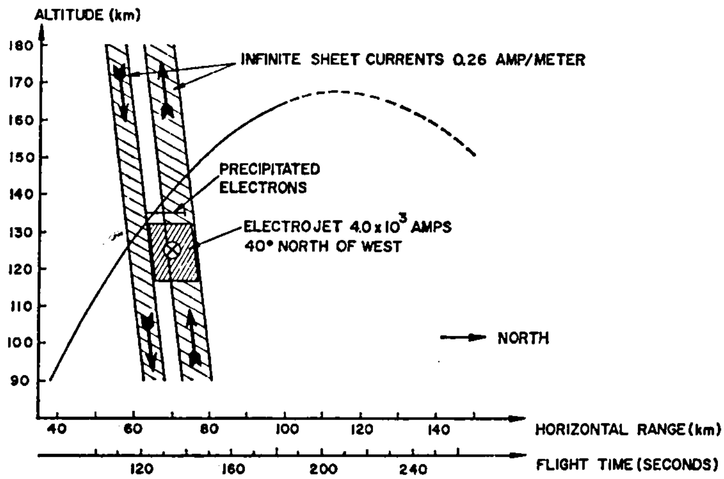

Fig. 1.5. Schematic representation of the vehicle trajectory and the relationship of the horizontal electrojet, the magnetically aligned sheet currents, and the precipitated electron profile (Cloutier et al., 1970).

seen in quiet times, is the field-aligned current sheets, i.e., the Birkeland currents. Cloutier et al.(1970) and Park and Cloutier(1971) presented the observational evidence by the rocket-borne experiment consisting of a vector magnetometer system and energetic charged particle detectors that there exists geomagnetically aligned sheet currents associated with the visible auroral arcs, and that precipitated energetic electrons in the range 2 to 18 kev carry a significant fraction of the total upward field-aligned current, but energetic particles in this range are apparently unimportnat in the downward sheet current. Fig. 1.5 illustrates schematically the spatial relationship of the model current configuration used to fit the observed data. Cloutier et al.(1970) point out that the upward current flows through the horizontal westward electrojet, with the downward current displaced to the south side of the electrojet, and that the place of precipitated electrons is coincident with electrojet and upward current sheet. Thus, we have no doubt of the close relationship between auroral arcs and field-aligned currents. Why and how is such a current system formed ?

Among many potential candidates, we suggest the possibility that the ionospheric irregularity produced by, for example, the cross-field instability triggers such field-aligned currents as shown in Fig. 1.5. Once homogeneous auroral arcs are formed, they seem to be unstable for a

Fig. 1.6. Small-scale folding structure (of order 20 km) recorded by all sky camera at Baker Lake(Akasofu and Kimball, 1964).

variety of plasma instability, resulting in irregular arcs. Typical example of a larger scale folding (of 20 km) which is one of several active features added to a quiet and homogeneous arc is shown in Fig. 1.6. Though it is controversial whether this structure has its origin in the ionosphere or the magnetosphere, we may suggest that small-scale structure of the order of a few km is, more or less, formed by the action of the cross-field instability in the ionosphere.

Next, we describe the experimental results in a reflex arc. Hooper(1970) reported the characteristics of turbulence to be identified as the mode of the cross-field instability in a reflex arc plasma. He observed the transition from coherence to turbulent oscillation when the instability condition is strengthened. Fig. 1.7 shows an example of the probe ion current and floating potential in turbulent state. Note that this complicated waveform is due to strong nonlinear mode coupling which generates several beats between the modes. Another observational evidence given by Hooper is that the cross-field instability is limited by a quasilinear feedback effect which will reduce the background density gradient. This is shown in Fig. 1.8. We can regard that such a flattening of density profile gives an important clue to understanding of quenching mechanism of the cross- field instability. Ionospheric irregularities are also destined to stay at finite level, more or less. As yet, we do not

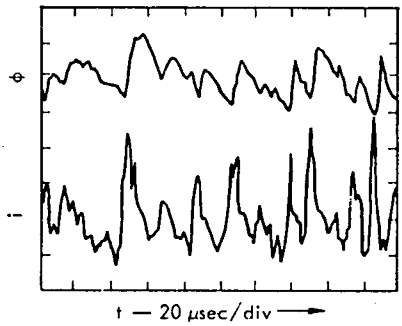

Fig. 1.7. Characteristics of probe ion current(lower curve) and floating potential (upper curve) observed in a reflex arc (Hooper and Girvin, 1971).

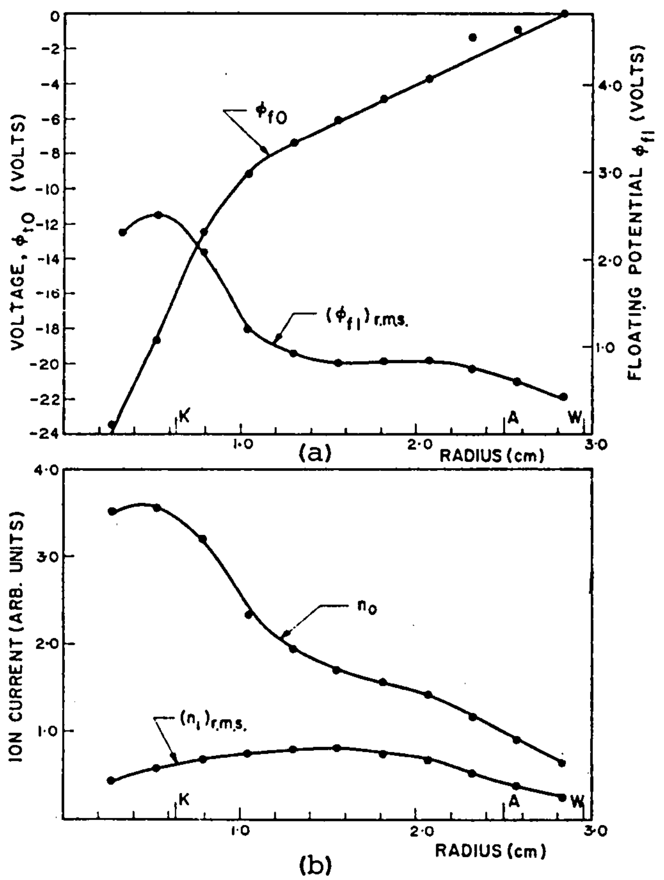

Fig. 1.8. Plasma characteristics versus radius of a reflex arc (Hooper, 1970). (a) Average floating potential and r.m.s. oscillating floating potential. (b) Average ion current and r.m.s. oscillating ion current.

know clearly the quenching mechanism of density irregularities in the ionosphere. However, it is easy to see that nonlinear behavior holds the keys of time evolution of irregularities.

We have presented typical examples of density irregularities observed in the ionosphere and laboratory, seemingly caused by the nonlinear cross-field instability. Now, we can point out the importance of nonlinear analysis of the cross-field instability , in order to have consistency of the observed results with the analysis.

In the following two sections, we review qualitatively the cross-field instability in linear and nonlinear regimes.

III. Linear Analysis

The cross-field instability was first predicted by Simon (1963) and Hoh(1963) independently, in laboratory plasmas of Penning-type discharge. Morse(1965) extended analysis to a more generalized form, i.e., two dimensional linear analysis.

In the ionosphere, the primitive idea of the cross-field instability was suggested first in the study of Martyn(1959), who inferred that ionozation irregularities might grow in the presence of a gradient of the ambient ionization density. Maeda et al.(1963) suggested that the same type of instability would occur at the geomagnetic equator, since the geometory of the equatorial E layer resembles to that of laboratory experiment. This study was extended to the formation of sporadic E layers at temperate latitudes by Tsuda et al.(1966).

Ths cross-field instability results from the Hall or Pedersen drift of charged particles in the presence of a plasma density gradient. In the lower ionosphere, the Hall mobility is much higher than the Pedersen mobility, and the instability mechanism is determined mainly by the (electron) Hall motion (Hall mode). On the other hand, in the upper E layer the Pedersen mobility dominates, so that the instability is controlled by the (ion) Pedersen motion (Pedersen mode). Since, however, we have no remarkable density gradient in this layer in a normal state, the Pedersen mode does not seem so essential for irregualrity formation as the Hall mode in the lower E layer.

Linear analysis under circumstances appropriate to the ionosphere was analysed by many other authors; for example Kato(1965, 1972), Whitehead(1967, 1968, 1970a, 1970b, 1971), Kato and Hirata(1967), Reid(1968), Chimonas(1969), and Cunnold(1969). Here it is worth noting that in linear analysis cited above a specific type of perturbation is assumed. Using a perturbation for different from that of Tsuda et al.(1966), Whitehead argued incorrectly that the cross-field instability could exist at the equator, but would not occur outside the equatorial region. The objection to this argument was given by Kato(1972) and Sato and Tsuda(1972) who showed that this difference of theories is not essential and we can expect the cross-field instability to exist also in midlatitudes as well as the equatorial regions.

Recently, it is said that this mechanism would be relevant to plasma cloud evolution in the ionosphere(for example, Wescott et al.(1969), Linson and Workman(1970), Rao and Russell(1971), and Davis(1971)). Further, Hooper and Walker (1971) and Ogawa and Sato(1971) almost simultaneously suggested that this instability would play some important role in formation and deformation of auroral arcs.

IV. Nonlinear Analysis

Linear analysis fails to tell the ultimate fate of an initial perturbation, although many aspects of laboratory plasma, ionospheric irregularities and plasma cloud experiment are brought to light by linear analysis. Unstable plasma in nature is destined to result in a turbulent state, in which energy supply to a plasma may be in harmony with energy dissipation from it. In such a state we may encounter new appearance which can never be recognized at the linear stage.

From a theoretical point of view, fluctuating state of a system may be divided into two categories; one is 'weak turbulence' and the other is 'strong turbulence'. In the cross-field instability, a turbulent state appears when the external electric field E_{ext} exceeds a critical value E_c. The concept 'weak turbulence' is useful under the condition of $\Delta = (E_{ext} - E_c)/E_c \ll 1$. When $\Delta \gtrsim 1$, however, system remains no more at a level of weak turbulence but develops into 'strong turbulence' where mode coupling becomes dominant. At this stage, mathematical approach becomes quite difficult. A high speed electronic computer in current use will give us a powerful means to unravel such a complicated process.

Nonlinear theory of the cross-field instability was developed by Kim and Simon(1969) and Hooper(1970) in the quasilinear regime, and Sato(1971) in both the quasilinear and mode coupling regimes. Kim and Simon obtained the mode amplitude, frequency shift, electric field change, flattening of background density distribution, and anomalous plasma transport in terms of a small parameter Δ implying mode coupling corrections to be small. Hooper analysed an anomalous transport in the quasilinear regime and compared with experimental results obtained in a reflex arc. His experimental result is compatible with the quasilinear calculation of Kim and Simon as far as the density flattening is concerned.

It was pointed out by Sato and Tsuda(1967) that since the dispersion relation of the cross-field instability is a decay type, three-wave interactions between different wavenumber components belonging to the same branch in the dispersion curve might be an important process in determining the turbulent state. It is further noted that the frequency of the instability is far below the ion-cyclotron frequency and the plasma frequency, so that neither cyclotron damping nor Landau damping are involved; this indicates that the resonant interaction of the waves with particles is not important, and hence, as a cause of nonlinear damping, only the wave-wave interaction is essential.

Viewed in this light, Sato(1971) has made an attractive study in which discussions are not confined to such limited cases as Kim and Simon(1969) and Hooper(1970) but a more general case is treated. In his theory, mode coupling plays an important role in the nonlinear evolution of the cross-field instability when $\Delta \gtrsim 1$. It is found that mode coupling can lead to an explosive instability, namely, an amplitude of unstable wave diverges within a finite time: When E_{ext} is below a critical value E_{c1}, the system behaves so gently that unstable waves always retain a finite level because both the quasilinear and mode coupling processes stabilize them. Beyond E_{c1} the system results in a strong turbulence. By this Sato's work, both the quasilinear and mode coupling effects on nonlinear state have become clear to some extent.

Williams and Weinstock(1970) developed the nonlinear theory of strong turbulence of the cross-field instability, applying to F region irregularities in the ionosphere (spread F). Based on the so-called "particle trapping" method, they derived the nonlinear dispersion relation, from the macroscopic Vlasov equation. However, this theory is so sophisticated that it is questionable how relevant to the actual plasma it is.

In order to study the competing behavior between the quasilinear and mode coupling effects and also to observe the deformation of the background quantities (background density and electric field), electronic computer must be a powerful tool. Computer analysis enables us to show the nonlinear evolution of plasma wave instability which otherwise might be intractable by conventional analytical methods. Also it has the advantage that we do not rely on misleading ad hoc assumptions.

Sato and Tsuda(1967), Tsuda and Sato(1968), Sato et al. (1972) performed numerical analysis of the cross-field instability in one-dimensional model appropriate to the lower ionospheric E layer. Sato and Tsuda(1968) and Tsuda et al. (1969) extended the analysis to two-dimensional model. Sato et al. found the cross-field instability to develop into a completely and rather stationary turbulent state, through the mode coupling. Relative amplitude of density fluctuations amounted to 30 - 50 % under the situation concerned there, and a phase mixing of each mode occurred, resulting in the prominent deformation of an initial fluctuation. Also they demonstrated that in the turbulent state energy supplied continuously from the unstable long wavelength was dissipated at short wavelength owing to collisional diffusion which becomes important at short wavelength. Sato et al. (1968) suggested in the light of the results described above that the formation mechanism of diffuse nonblanketing type sporadic E layers of midlatitudes might be attributed to the well-developed cross-field instability. Rocket observations of irregularity type E_s made by Smith(1966), Oya(1967), and Prakash et al.(1970) showed the existence of electron density irregularities with the amplitude of about a few tens percent, the wavelength of a few hundred meters, in the height range of a few or a few tens of kilometers. These observations were well explained in terms of the cross-field instability in a strong turbulent state.

In his recent paper, Davis(1971) has succeeded in observing nonlinear evolution of artificial alkali plasma clouds into the lower ionospheric E region by means of decameter and meter wavelength, coherent-pulse-Doppler radar. After an initial expansion, plasma cloud undergoes a period of irregular behavior, in which a number of discrete echoes from reflectors appear superimposed on the generally diffuse plasma radar echo. He indicates that, in this phase of plasma cloud evolution intense, nearly monochromatic echoes grow with growth time of a few tenths of seconds and decay with decay time of a few seconds; these echoes repeatedly appear and decay, and the recurrence lasts several minutes. Davis finds that this evolution of clouds is consistent with that of the nonlinear instability analysis of Sato et al..

From viewpoint of plasma physics, nonlinear analysis of the cross-field instability presents an attractive example where mode coupling plays an important role. Sato et al. (1972) extended their one-dimensional nonlinear instability analysis for a number of different external electric fields to know how the nonlinear evolution depends on this parameter. Their finding is as follows. When $E_{ext} < E_{c1}$, E_{c1} being cited above, the system behaves gently and wave form is sawtooth like. When $E_{ext} > E_{c1}$, however, the system becomes violent and develops into strong turbulence; the waveform becomes soliton-like and density power spectrum obeys approximately a k^{-3} law, k being wavenumber. These results are rather consistent with those of Sato's prediction(1971) of the nonlinear theory.

Some turbulent structures of the system have been corroborated by one-dimensional nonlinear analysis. It must be, however, pointed out that the cross-field instability is essentially two-dimensional phenomenon judging from the mechanism of instability. Therefore, one must take into account not only interactions between growing modes but also feedback of wave energy into the background quantities which sustain the initial growth of the instability. The two-dimensional numerical analysis was performed by Sato and Tsuda(1968) and Tsuda et al.(1969). They obtained the following two important features. First, in the early phase of evolution a rather localized, spatially coherent density irregularity is formed. Second, the nonlineer quenching of unstable waves is established through the cancellation of the external electric field. This latter features contrasts with the result of the one-dimensional calculations where the quenching is achieved due to the energy dissipation through mode coupling only. Based on this calculation, they also suggest the possibility of a cyclic process of growth, quenching, and decay.

We remark here the difference between the conclusion of Kim and Simon(1969) and Hooper(1970) and that of Sato et al. concerning nonlinear quenching mechanism. This may be due to the fact that they used the different boundary conditions. The boundary condition of Kim and Simon and Hooper is appropriate to laboratory plasma and that of Sato et al. to the ionosphere, maybe.

In a cesium plasma cloud experiment, Davis(1971) observed the cyclic growth and decay process in the discrete spectral features obtained by decameter radar. This result seems to be consistent with the prediction of two-dimensional nonlinear analysis.

Hooper in a series of papers(1970a, 1970b, 1971a, 1971b) studied experimentally the low frequency oscillation in a reflex arc, making use of correlation techniques. His result strengthens the identification of the mode as the cross-field instability, and shows a clear cut transition from coherent to incoherent oscillations when the instability condition is strengthened. A detailed comparison of experiments with the nonlinear results is not possible because experiments are usually performed in cylindrical geometory whereas the nonlinear studies are done in slab geometory. Nevertheless, there are several points to be compared. Hooper notes, first, that primary quasilinear effect is due to the flattening of density profile rather than that of average electric field, as predicted by Kim and Simon. Second, Sato's condition for the onset of strong turbulence, i.e., $E_{ext} > E_{c1}$, are satisfied. Third, the strong turbulence observed in the experiments shows the closest resemblence to computer analysis.

V. Summary

We have given a brief qualitative review of the cross-field instability, attention being paid to nonlinear aspects. It should be remarked that the cross-field instability in question is entirely common phenomenon in the lower ionospheric E layer where dynamo electric field (or other electric field) and the gradient of electron density coexist. If the instability condition is satisfied, even the upper ionosphere is susceptible to this instability.

Nonlinear evolutions observed in experiments in the ionosphere and laboratory are to some extent explained by the computer analysis of Sato et al.. However, it should be remarked that a little inconsistency remains to be settled. Accordingly it is highly desired that a further two-dimensional nonlinear calculation should be carried out, for suitable boundary conditions, in order to observe the competing process between the quasilinear and mode coupling effects and to see the deformation of background quantities. Such an analysis may faciliate comparison with experiments still more.

Chapter 2

ONE - DIMENSIONAL NONLINEAR CROSS - FIELD INSTABILITY

I. Introduction

Present objective is to reveal the time evolution of one-dimensional nonlinear cross-field instability using a computer. We assume that all the variables vary only in $\underset{\sim}{E}_{ext} \times \underset{\sim}{B}_0$ direction, i.e., the direction of wave propagation. This means that we neglect the interaction between the perturbation and zeroth order background quantities (inhomogeneity of the background density ∇n_0 and dc electric field E_{ext}) which sustain the instability.

It is found by linear analysis that the dispersion relation is of decay type because the phase velocity increases with increasing wavenumber. Therefore, the three-wave decay process between different wavenumber components on the same branch in the dispersion curve is important as the mode coupling process, but not the scattering or emission of the waves belonging to other branches.

Strong turbulent state of the cross-field instability in one-dimensional model was investigated by Sato and Tsuda(1967). They found well-developed turbulent irregularity whose amplitude amounts up to about 50 % of the background density, and the nonlinear quenching of the amplitude was achieved in such a way that the energy supply from ∇n_0 and E_{ext} is balanced by the energy dissipation due to mode coupling. Sato et al. (1972) has discussed other aspects of turbulent state. They found that a saw-tooth (shock-like) solution exists for some range of E_{ext}, and that the solution becomes localized and soliton-like for larger E_{ext}. The value of E_{ext} differentiating the solution from the former to the latter agreed well with that of the theory (Sato, 1971).

In this chapter, we investigate nonlinear behavior for E_{ext} far greater than the critical value described above, since the earlier calculations did not analyse the nonlinear evolution in this parameter range.

II. Basic Equations

We consider a compressible, weakly ionized low-β plasma immersed in uniform magnetic and electric fields, and the following fluid-dynamical, electrostatic equations for electrons and ions are used (in MKS units);

$$m_\alpha \frac{d\underset{\sim}{v}_\alpha}{dt} = e_\alpha \left(\underset{\sim}{v}_\alpha \times \underset{\sim}{B}_0 + \underset{\sim}{E}_0 + \tilde{\underset{\sim}{E}} \right) - m_\alpha \nu_\alpha \underset{\sim}{v}_\alpha - \frac{T_\alpha}{n_\alpha} \nabla n_\alpha , \tag{2 · 1}$$

$$\frac{\partial n_\alpha}{\partial t} + \underset{\sim}{\nabla} \cdot (n_\alpha \underset{\sim}{v}_\alpha) = 0 \qquad (\alpha = e, i) , \tag{2 · 2}$$

$$\underset{\sim}{\nabla} \cdot \tilde{\underset{\sim}{E}} = \frac{e}{\varepsilon_0} (n_i - n_e) . \tag{2 · 3}$$

Here, the subscript α denotes electrons (e) and ions (i) and n_α refers to the density, m_α the particle mass, ν_α the collision frequency with neutrals, $\underset{\sim}{v}_\alpha$ the velocity, T_α the temperature in eV, e (>0) the electron charge, ε_0 the permittivity of free space, $\underset{\sim}{B}_0$ the uniform magnetic field. $\underset{\sim}{E}_0$ and $\tilde{\underset{\sim}{E}}$ are the dc and ac electric fields, respectively. Note that we use explicitly Poisson's equation (2.3) in order to check the validity of quasi-neutrality assumption, $n_i \sim n_e$, assumed in the earlier literatures and also to avoid the numerical instability in the initial stage of numerical calculation. We neglect the production and loss of charged particles in Eq (2.2), since these processes are much slower processes than that of the instability.

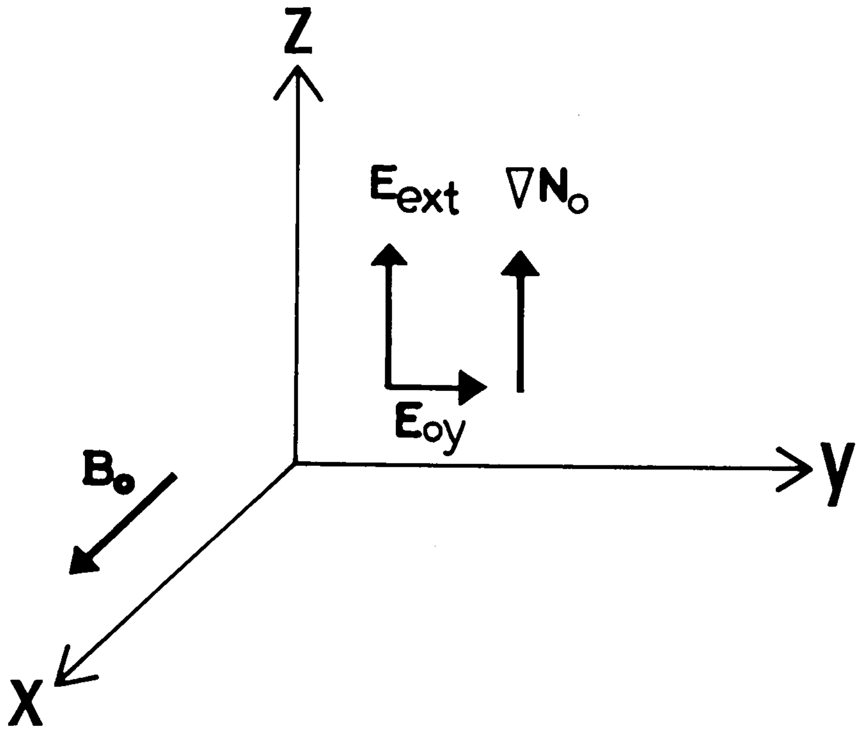

Fig. 2.1. Coordinate system.

III. Description of System

The geometory considered is shown in Fig. 2.1 where the gradient of background plasma density ∇n_0 and $\underset{\sim}{B}_0$ are respectively in the z and x directions, and $\underset{\sim}{E}_0$ lies on the y - z plane, i.e.,

$$\nabla n_0 = (0,\ 0,\ \frac{dn_0}{dz}),\quad \underset{\sim}{B}_0 = (B_0,\ 0,\ 0),\quad \underset{\sim}{E}_0 = (0,\ E_{0y},\ E_{ext})$$

This cofiguration is adopted in most of the previous works of the cross-field instability, and may well correspond to geomagnetic equatorial and auroral regions of the ionosphere and even to a reflex arec.

Since we are interested in one-dimensional model in this chapter, only the y dependence of variables is considered. Accordingly, the induced electric field $\underset{\sim}{\tilde{E}}$ is in the y direction, i.e., $\underset{\sim}{\tilde{E}} = (0,\ \tilde{E}_y(y,t),\ 0)$. As usual the variables n_α, $\underset{\sim}{v}_\alpha$ are divided into two parts in the following way,

$$\begin{aligned} n_\alpha &= n_0(z) + \tilde{n}_\alpha\ (y,t), \\ v_{\alpha y} &= V_{\alpha 0y} + \tilde{v}_{\alpha y}(y,t), \\ v_{\alpha z} &= V_{\alpha oz} + \tilde{v}_{\alpha z}(y,t), \end{aligned} \qquad (2 \cdot 4)$$

where the first terms on the right sides represent the unperturbed state and the second terms the perturbed state from the equilibrium. We assume the background density distribution of exponential type, $e^{\kappa z}$, along the z direction, with scale height κ^{-1}, that is,

$$\frac{1}{n_0}\frac{dn_0}{dz} = \kappa, \quad \text{or } n_0 = N_0\, e^{\kappa z} \quad \text{where } N_0 = n_0(z=0) \qquad (2.5)$$

because this type of distribution is easy to analyze the instability in a linearized version and to compare the growth rate of the linear analysis with that of the computed result. Further, we shall confine ourselves to event with frequency much lower than ν_i and ω_{Hi} (ion cyclotron frequency). The inertia term of electrons in (2.1) can justifiably be neglected, but that of ions is retained for safety.

Under these circumstances, (2.1) to (2.4) give the following equation to be solved,

$$\left.\begin{aligned}
V_{\alpha 0y} &= \mu_p^{\alpha} E_{oy} + \mu_H^{\alpha} E_{ext} - \mu_\alpha B_0 D_\perp^{\alpha}\kappa\,, \\
V_{\alpha 0z} &= -\mu_H^{\alpha} E_{0y} + \mu_p^{\alpha} E_{ext} - D_\perp^{\alpha}\kappa \qquad \alpha = e,\, i\,, \\
\tilde{v}_{ey} &= -\mu_p^{e}\tilde{E}_y - \frac{D^e}{n_e}\frac{\partial \tilde{n}_e}{\partial y} + \mu_e B_0 D_\perp^{e}\left(\frac{1}{n_e}\frac{dn_0}{dz} - \kappa\right), \\
\tilde{v}_{ez} &= -\mu_H^{e}\tilde{E}_y - \mu_e B_0 \frac{D^e}{n_e}\frac{\partial \tilde{n}_e}{\partial y} - D_\perp^{e}\left(\frac{1}{n_e}\frac{dn_0}{dz} - \kappa\right),
\end{aligned}\right\}$$

$$
\left.
\begin{aligned}
\frac{1}{\nu_i}\frac{\partial \tilde{v}_{iy}}{\partial t} &= \mu_i(B_0\tilde{v}_{iz} + \tilde{E}_y) - \tilde{v}_{iy} - \frac{D_i\partial \tilde{n}_i}{\bar{n}_i\partial y}, \\
\frac{1}{\nu_i}\frac{\partial \tilde{v}_{iz}}{\partial t} &= -\mu_i B_0\tilde{v}_{iy} - \tilde{v}_{iz} - D_i\left(\frac{1}{n_i}\frac{dn_0}{dz} - \kappa\right), \\
\frac{\partial \tilde{E}_y}{\partial y} &= \frac{e}{\varepsilon_0}(\tilde{n}_i - \tilde{n}_e),
\end{aligned}
\right\} \quad (2 \cdot 6)
$$

where

$$
\mu_\alpha = \frac{e_\alpha}{m_\alpha \nu_\alpha}, \qquad D_\alpha = \frac{T_\alpha}{m_\alpha \nu_\alpha},
$$

$$
\mu_p^\alpha = \frac{\mu_\alpha}{1 + (\mu_\alpha B_0)^2}: \quad \text{Pedersen mobility,}
$$

$$
\mu_H^\alpha = \mu_p^\alpha(\mu_\alpha B_0) \;:\; \text{Hall mobility,} \qquad (2 \cdot 7)
$$

$$
D_\perp^\alpha = \frac{D_\alpha}{1 + (\mu_\alpha B_0)^2}.
$$

Hereafter we represent dn_0/dz by κN_0.

IV. Machine Calculation

A. Scaling

Before the machine calculation, we perform a scaling of variables appeared in (2.6) as follows;

$$\eta = \frac{y}{L}, \qquad \tau = \frac{V_0}{\varepsilon L} t = \frac{t}{T}, \qquad (2 \cdot 8)$$

where $L = 1/\kappa = (1/n_0 \cdot dn_0/dz)^{-1}$, $V_0 = \mu_H^e E_{ext}$. V_0 is a Hall speed of electrons, and a constant ε is introduced for convenience. Density and electric field are scaled by

$$\rho_i(\eta,\tau) = \frac{\tilde{n}_i(y,t)}{N_0}, \quad \rho_e(\eta,\tau) = \frac{\tilde{n}_e(y,t)}{N_0},$$

$$\sigma(\eta,\tau) = \frac{\tilde{E}_y(y,t)}{E_{ext}}, \quad \sigma_0(\eta,\tau) = \frac{E_{oy}}{E_{ext}}. \qquad (2 \cdot 9)$$

The dimensionless new velocities are

$$\xi_{e0} = \frac{V_{eoy}}{V_0}, \quad \xi_{i0} = \frac{V_{i0y}}{V_0}, \quad \zeta_{e0} = \frac{V_{e0z}}{V_0}, \quad \zeta_{i0} = \frac{V_{i0z}}{V_0},$$

$$\xi_e = \frac{\tilde{v}_{ey}}{V_0}, \quad \xi_i = \frac{\tilde{v}_{iy}}{V_0}, \quad \zeta_e = \frac{\tilde{v}_{ez}}{V_0}, \quad \zeta_i = \frac{\tilde{v}_{iz}}{V_0}.$$

$$(2 \cdot 10)$$

By making use of (2.8) to (2.10), (2.6) is reduced to

$$\xi_{e0} = 1 + \frac{A_1}{A_2} - A_2\sigma_0 ,$$

$$\xi_{i0} = B_3(1 - \frac{B_1}{B_2}) + B_2\sigma_0 ,$$

$$\zeta_{e0} = - A_1 - A_2 - \sigma_0 ,$$

$$\zeta_{i0} = - B_1 + B_2 - B_3\sigma_0 ,$$

$$\left.\begin{aligned}
\xi_e &= - \frac{A_1}{A_2} - A_2\sigma + \frac{A_1}{1 + \rho_e}\left(\frac{1}{A_2} - \frac{1}{\varepsilon}\frac{\partial\rho_e}{\partial\eta}\right) , \\
\zeta_e &= A_1 - \sigma - \frac{A_1}{1 + \rho_e}\left(1 + \frac{1}{\varepsilon A_2}\frac{\partial\rho_e}{\partial\eta}\right), \\
\frac{\partial\xi_i}{\partial\tau} &= C_1\left[\frac{B_3}{B_2}\zeta_i - \xi_i + \left\{1 + \left(\frac{B_3}{B_2}\right)^2\right\}\left(B_2\sigma - \frac{B_1}{1 + \rho_i}\partial\frac{\partial\rho_i}{\partial\eta}\right)\right] , \\
\frac{\partial\zeta_i}{\partial\tau} &= - C_1\left[\frac{B_3}{B_2}\xi_i + \zeta_i + B_1\left\{ 1 + \left(\frac{B_3}{B_2}\right)^2\right\}\left(\frac{1}{1 + \rho_i} - 1\right)\right],
\end{aligned}\right\} \quad (2.11)$$

$$
\left.
\begin{aligned}
\frac{\partial \rho_e}{\partial \tau} &= -\varepsilon \left[\zeta_e + (1 + \rho_e) \frac{\partial \xi_e}{\partial \eta} + (1 + \xi_e) \frac{\partial \rho_e}{\partial \eta} \right], \\
\frac{\partial \rho_i}{\partial \tau} &= -\varepsilon \left[\zeta_i + (1 + \rho_i) \frac{\partial \xi_i}{\partial \eta} + (1 + \xi_i) \frac{\partial \rho_i}{\partial \eta} \right],
\end{aligned}
\right\} \qquad (2.12)
$$

$$
\frac{\partial \sigma}{\partial \eta} = C_2 (\rho_i - \rho_e), \qquad (2 \cdot 13)
$$

where

$$
A_1 = \frac{D^e_\perp \kappa}{V_0}, \quad A_2 = \frac{\mu^e_p}{\mu^e_H}, \quad B_1 = \frac{D^i_\perp \kappa}{V_0}, \quad B_2 = \frac{\mu^i_p}{\mu^e_H},
$$

$$
B_3 = \frac{\mu^i_H}{\mu^e_H}, \quad C_1 = T\nu_i, \quad C_2 = \frac{eN_0}{\varepsilon_0 \kappa E_{ext}}.
$$

Note that (2.11), (2.12) and (2.13) are the equations of motion, continuity, and Poisson's equation, respectively.

B. Numerical Procedure

In the previous work of one-dimensional model by Sato and Tsuda(1967), used was a spatial Fourier transformation of variables. They solved equations under the assumption of quasi-neutrality and therefore did not use Poisson's equation. On the contrary, we integrate (2.11) to (2.13) in real space (y,t). Hence, the wave-wave interaction between harmonic waves cannot be recognized explicitly. For numerical computation, length η and time τ is divided into

$$\eta = m\Delta\eta \qquad m = 0,\ 1,\ 2,\ \cdots\cdots,$$
$$\tau = n\Delta\tau \qquad n = 0,\ 1,\ 2,\ \cdots\cdots,$$

where $\Delta\eta$ and $\Delta\tau$ indicate, respectively, the mesh width and time step. (2.11) to (2.13) are then replaced by finite difference equations. The boundary condition of the y direction is taken to be periodic on a scale length ℓ , i.e.,

$$f(\eta = 0, \tau) = f(\eta = \ell, \tau),$$

where $\ell = M\Delta\eta$. The numerical procedure for the one-time step is as follows. First, initial density perturbations, ρ_e and ρ_i, are substituted in (2.11) with $\sigma = 0$, to obtain ξ_e, ζ_e, ξ_i and ζ_i. Then, (2.12) is solved to know the new ρ_e and ρ_i after $\Delta\tau$ and σ is determined by (2.13). These new variables are again substituted in (2.11) to obtain new velocities. Same procedure is repeated as long as we need.

When the number of cycles of calculation increases, we should always pay attention to the accumulation of errors originating from the unsuitable choice of $\Delta\eta$ and $\Delta\tau$. It is necessary to select $\Delta\tau$ to be far smaller than the shortest characteristic period of the system concerned. This period of our system is the ion oscillation as is easily seen from (2.11) to (2.13). On the other hand, $\Delta\eta$ may be determined from the requirement that how many higher harmonics of fundamental wave is necessary for the manifestation of nonlinear evolution of the instability. That is, the smaller $\Delta\eta$ becomes, the more the number of modes considered increases and inevitably $\Delta\tau$ is required to be smaller. Attention should be paid especially when we want to know the strong turbulence, which is of our interest, originating from mode coupling. Thus, whether or not we have a meaningful solution of equations largely depends on the ability of the computer at hand.

C. Computed Results

Since some numerical computations of one-dimensional model were already performed by Sato et al., we confine ourselves to the larger dc electric field, E_{ext}, than the previous works, and supplement some conclusions in the following section.

Table. 2.1. Parameters of computation.

Parameters	Value
ε	1/90
σ_0	5×10^{-3}
T	16
A_1	1.73×10^{-9}
A_2	2×10^{-3}
B_1	3.92×10^{-8}
B_2	4.55×10^{-2}
B_3	2.08×10^{-3}
C_1	6.4×10^{4}
C_2	4.52×10^{8}
$\Delta\tau$	6×10^{-7} for $\tau=0 \sim 2.52\times10^{-4}$
	6×10^{-6} for $\tau > 2.52\times10^{-4}$
$\Delta\eta$	3.33×10^{-3}
E_{ext}/E_{c0}	1.3×10^{7}

We took $E_{ext} = 2\times10^{-2}$ V/m, $\kappa = 1/(5\times10^5)$/m. Such a large electric field may exist in the auroral ionosphere, though the system concerned in this paper is not necessary pertinent to that region. With $\mu_e B_0 \sim 5\times10^2$, $\mu_i B_0 \sim 4.6\times10^{-2}$, $D_e = 7.6\times10^4$, $D_i = 6.87$, the coefficient A_1 to C_2 are listed in Table 1 where ε and σ_0 are also tabulated.

As the initial condition of densities, ρ_e and ρ_i, we imposed a monochromatic (sinusoidal) disturbance whose wave-number and amplitude are $2\pi/0.08L$ and 0.01 (1 % of the background density), respectively. Note $\Delta\tau$ to be far smaller than the ion oscillation period (5.2×10^{-5} in normalized time). $\Delta\eta = 3.3\times10^{-3}$ means that the fundamental wavelength (0.08L) is divided into 24 meshes. According to linear analysis, the linear growth time is $\tau_L = 4.7$ ($\sim$75 sec in real time).

Shown is the computed result in Fig. 2.2 through Fig. 2.4. It is observed that at the very beginning of the calculation an ion oscillation appeared, but after a few cycle of the oscillation it disappeared due to the ion - neutral collision damping. After the death of the transient ion oscillation, $\Delta\tau$ was increased from 6×10^{-7} to 6×10^{-6}. In such a large electric field as this, the two-stream instability might occur However, its occurrence is inhibited in our case because the wavelength of the two-stream modes is shorter than the mesh size. Further, we could make sure of the equality of ρ_e and

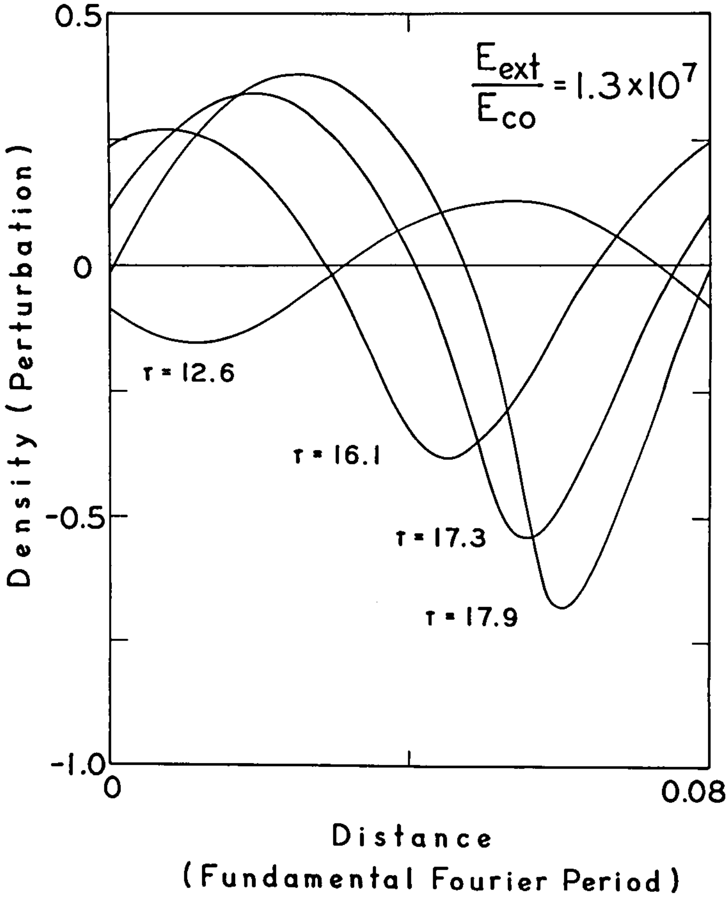

Fig. 2.2. Time evolution of the density perturbation (ρ_e). ρ_e versus distance η is shown for E_{ext}/E_{c0}= 1.3×10^7. The initial perturbation(τ=0) has the wavelength of 0.08. It is seen that the perturbation is localized at τ=17.9.

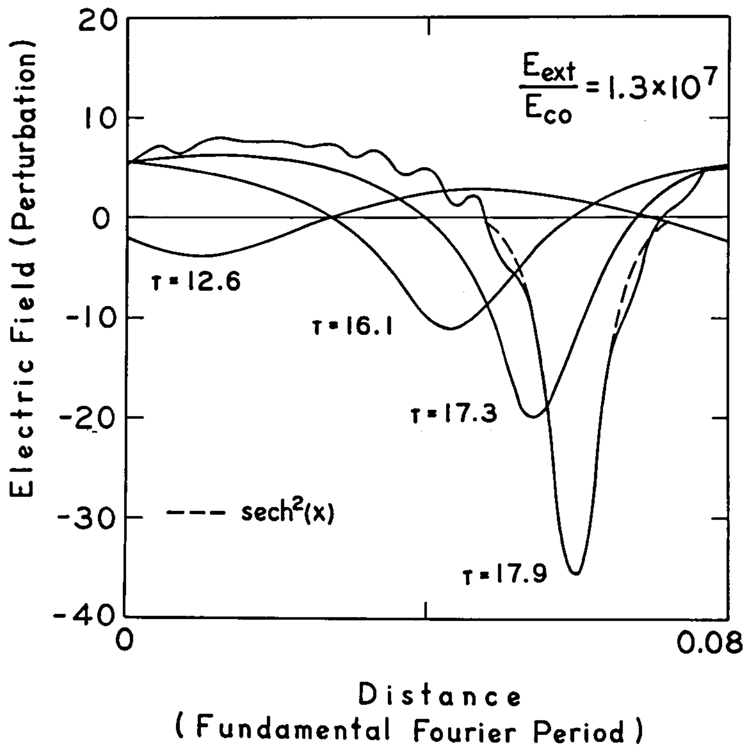

Fig. 2.3. Time evolution of the electric field perturbation (σ). σ versus distance η is shown for $E_{ext}/E_{c0} = 1.3\times10^7$. By comparing with Fig. 2.2, it is seen that the electric field perturbation is more likely to be localized than the density perturbation. Note that the localized form is very similar to the square of a hyperbolic-secant function which is a solution of the Kortweg de Bries equation. The small scale irregularities on the curve of τ=17.9 may be due to numerical instability.

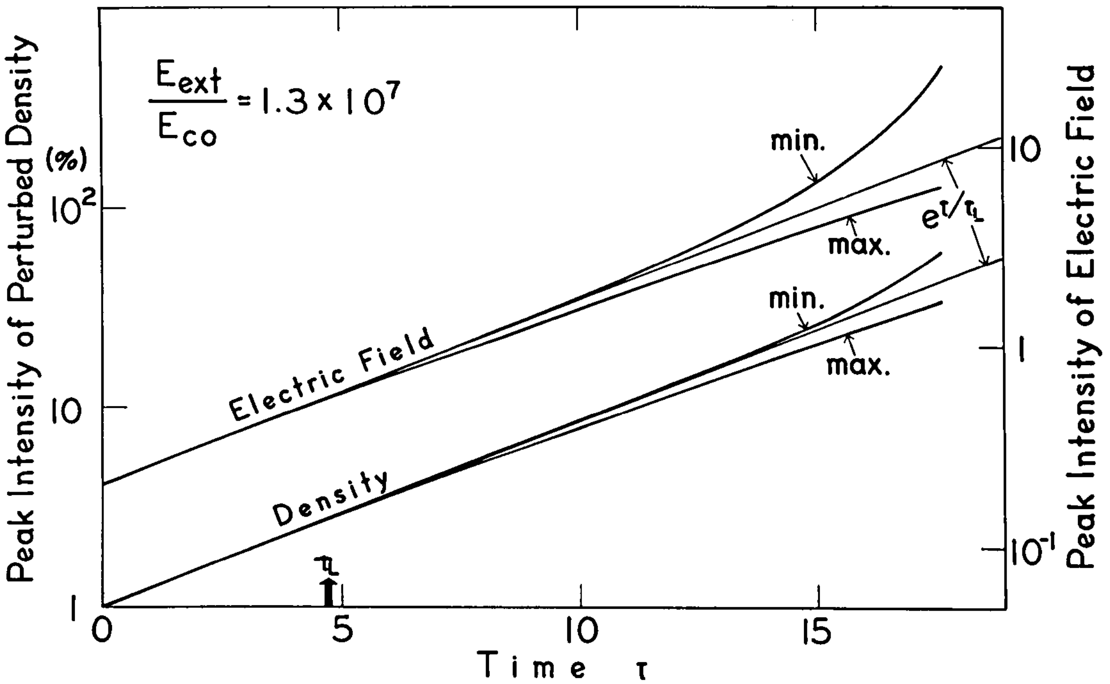

Fig. 2.4. Time evolution of the peak values of the density (ρ_e) and electric field (σ) perturbations. ρ_e and σ versus time τ are shown for $E_{ext}/E_{c0}=1.3\times 10^7$. Absolute values are shown for the minimum. τ_L means the linear growth time. The straight line e^{τ/τ_L} is drawn for the reference. It is seen that after $\tau=\tau_L$ the perturbations grow while gradually deviating from e^{τ/τ_L}.

ρ_i to a high degree (i.e., quasi-neutrality).

Fig. 2.2 shows the time evolution of the density perturbation ρ_e. At the initial stage, up to $\tau = 10$, the perturbation grows with the linear growth time τ_L as it propagates along the η direction: The initial perturbation keeps the sinusoidal shape for a while, though the amplitude is growing. But as times go on further, nonlinear mode coupling between higher harmonics acts so as to deform the shape as seen in Fig. 2.2 and 2.3; at $\tau = 17.9$ the peak amplitude of ρ_e attained to a percentage of several tens of the background. Thereafter the system was broken down by numerical instability.

The time evolution of the electric field perturbation is shown in Fig. 2.3. A curve of the square of hyperbolic-secant function is drawn for reference. From this it is seen that the localized form is soliton-like. Some indication of numerical instability is seen on the curve of $\tau = 17.9$.

Fig. 2.4 shows the time evolution of the peak values of the density and electric field perturbations. Also shown is the straight line e^{τ/τ_L} along which perturbations would grow if the deformation did not occur. The result indicates that at the initial stage the perturbation grows with the linear growth time $\tau_L = 4.7$, but after τ_L it deviates from the linear growth due to the action of the mode coupling as expected.

Though we had a numerical instability after the time $\tau = 17.9$, this instability could be overtaken by taking smaller mesh width $\Delta\eta$. Thus, a pursuit of strong nonlinearity requires the inclusion of more higher harmonics of a fundamental wave (i.e., smaller $\Delta\eta$), accordingly more computational time is needed. Nevertheless, we have some indication of the onset of strong nonlinearity at time $\tau = 17.9$, though we could not know the ultimate fate of the instability.

V. Discussion

We have investigated the time evolution of the cross-field instability for an extremely large external electric field different from the previous works.

Here, we shall review some essential points of theoretical results of the cross-field instability made by Sato(1971). When E_{ext} exceeds a certain threshold value E_{c0}, drift modes lying on a dispersive part of the dispersion curve becomes unstable. Further, when E_{ext} becomes larger than E_{c1} ($> E_{c0}$), the mode coupling acts to destabilize unstable waves, resulting in explosive instability. In this case, the theory fails to give precise information on the fate of unstable modes. The value of E_{c1} is given as a solution of $\mu = 0$, μ being the mode coupling element (see equation (45) of Sato(1971)*)).

*) 3ε of equation (45) should be read as $(5\chi - 6)\varepsilon$.

If E_{ext} is below E_{c0}, all the modes are stabilized by diffusion.

In our case, $E_{c0} = 1.46 \times 10^{-9}$ V/m and $E_{c1} = 39E_{c0}$ V/m. Accordingly $E_{ext} \sim 1.3 \times 10^{7}$ E_{c0} V/m, far greater than E_{c1}. Therefore, theory predicts that the system will suffer explosive instability. Also the theory tells that the system would become explosive at a certain finite rime τ_{exp}. Our parameter used for the numerical computation gives 21 as τ_{exp}. We have already stated that numerical instability occurred at $\tau \sim 18$. Thus the appearance of numerical instability might reflect some indication of the onset of strong mode coupling or a strong turbulent state, and therefore the theoretical explosive time τ_{exp} would be a good indication of the onset time of strong turbulence.

The same calculations were performed for other parameters; E_{ext}/E_{c0} = 3.3, 5.4, 16.5, 33, 54 (Sato et al., 1972. Note $E_{c1} \sim 12$ E_{c0} in these cases). The result was that a sawtooth (shock-like) solution was achieved for $E_{ext}/E_{c0} = 3.3$, 5.4, and that the solution became localized and soliton-like for E_{ext}/E_{c0} = 16.5, 33 and 54. That is, the system underwent a transition from weak to strong nonlinearity when E_{ext} was increased beyond E_{c1}. It should be noted that a localized and soliton-like solution was obtained in our case, though we met a numerical instability after $\tau = 18$. This fact may indicate that the localized perturbation maintain its form and may eventually be collapsed, thereby forming a strongly

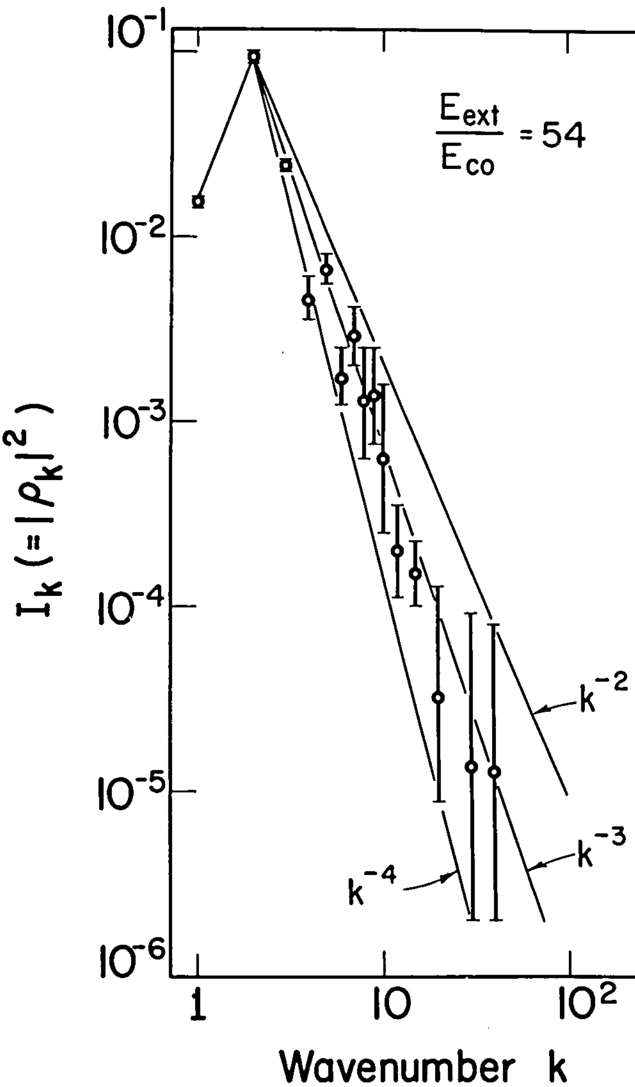

Fig. 2.5. Turbulent power spectrum of density versus wavenumber k for $E_{ext}/E_{c0} = 54$ (Sato, Ogawa and Matsuda, 1972). The error bar means the amplitude distribution in a turbulent state. The figure indicates clearly that the spectrum obeys k^{-3} law.

turbulent state. Fig. 2.5 shows a typical turbulent spectrum of density fluctuations which obeys a power law of k^{-3} as obtained for $E_{ext}/E_{c0} = 54$ (Sato et al., 1972). From this figure it may be inferred that the spectrum for the present case ($E_{ext}/E_{c0} = 1.3 \times 10^{7}$) may also obey a power law of $k^{-\alpha}$, perhaps being harder than that of Fig. 2.5. Note that the spectrum for $E_{ext}/E_{c0} = 3.3$ and 5.4 did not obey a power law but softer than k^{-3}.

VI. Conclusion

Nonlinear evolution of the cross-field instability which occurs in an inhomogeneous, magnetized weakly ionized plasma has been investigated numerically. It is found that for an extremely large external electric field a perturbation grows and results in a localized and soliton-like form in highly turbulent state (strong nonlinearity). Unfortunately, we met a numerical instability. Nevertheless, this numerical instability seems to indicate the onset of an explosive instability through many-mode couplings, whose aspects would be disclosed if we took a smaller mesh size.

Poisson's equation and inertia term of ions were included in computation and we could check the validity of the quasineutral assumption.

The important role of the cross-field instability in an ionospheric irregularity and a laboratory plasma has been pointed out by many authors. In the ion cloud experiments made by Davis(1971), it is found that the turbulent evolution could be well explained by the nonlinear theory of this instability. Auroral arcs, where strong electric field, say of 2×10^{-2} V/m, exists, as well as the equatorial ionosphere, may be susceptible to the instability. All of these can be better understood by the consideration of the nonlinear stage of the cross-field instability.

We have concerned ourselves with one-dimensional model, but two-dimensional solution is highly required in order to know how the nonlinear quenching will be achieved in nature and to compare the theory with the observed results. This is the next problem to be solved.

Chapter 3

TWO - DIMENSIONAL NONLINEAR CROSS - FIELD INSTABILITY

I. Introduction

One-dimensional model has been discussed in the previous chapter. We try here to extend one-dimensional model to two-dimensional one. One-dimensional model was good enough to clarify the role of wave-wave interactions. However, the cross-field instability is essentially two-dimensional as can be seen in its physical picture. Therefore, the nonlinear interaction of unstable waves with the energy reservoirs, ∇n_0 and E_{ext}, must be taken into account.

As was discussed already, the nonlinear quenching of one-dimensional model was achieved only by the balance between the energy supply from reservoirs and the energy dissipation owing to mode coupling. On the other hand, Sato and Tsuda (1968) and Tsuda et al.(1969) showed by their computer analysis that the two-dimensional nonlinear quenching was partly caused by the cancellation of applied electric field due to redistribution of charged particles through mode coupling. Namely, the saturation of growing waves is well correlated with the vanishing of the electric field E_{ext}. They also infer that the system might be transient or recurring. That is, a large amplitude irregularity developed from a small initial fluctuation will decay after the condition of the vanishing of E_{ext} is achieved, because the energy dissipation from smaller to larger wavenumber components due to mode coupling is still operating; at the moment of disappearnace, however, the condition of instability growth may be retrieved. This inference differs from the result of the one-dimensional model that a rather steady state is achieved in such a way as was described previously. These results are quite interesting since they gave a first step to disclose the process of the two-dimensional nonlinear quenching.

Hooper(1970, 1971) studied experimentally the low frequency, rotational oscillation present in a reflex arc. The oscillation observed was identified as arising from the cross-field instability. However, a discrepancy with the computer analysis was found concerning the nonlinear quenching (qausi-linear effect); he states that the instability was shut off by a plateau formation in the density profile whereas Sato and Tsuda's computer analysis says that the quenching is due to the plateau formation in the potential profile. This discrepancy seems, however, to be not so surprising, since the boundary conditions were different each other. The boundaries in Hooper's experiment are electrodes (conductors) but those in the computer analysis are free boundaries. In the latter case, to which the ionosphere may correspond, it may be said that the charge separation, resulting in a plateau formation in the potential profile, is formed more easily than the transport of charged particles by which a plateau in the density profile is formed. In the former case, however, excess charges accumulated at the boundaries will be short-circuited by the external circuit, so that the flattening of the potential profile may not be so significant. Of course we should remember that both processes (i.e., flattening of the density and of the potential) may take place at the same time, depending on the boundary condition used. Also Hooper's experiment found no indication of the recurrence (relaxation-type behavior) inffered from the computer analysis.

Artificial plasma cloud experiments in the ionosphere by Davis(1971) are in favor of the well-developed cross-field instability and show some tendency of the recurrence.

Kim and Simon(1969) developed a quasilinear theory in a weakly unstable limit and found the density flattening. Hooper(1970) studied the convection nature of nonlinear oscillation. His result may well describe the system in the quasilinear regime.

Recently, Sato(1971) has made an analytical study in which discussions were not confined to those of Kim and Simon and Hooper, but a more general case, i.e., the competition between quasilinear effect and mode coupling, was considered. Some important conclusions are as follows: The system experiences two types of transition when the external parameter, E_{ext}, is increased from zero to infinity. Below a critical value E_{c0} of the parameter any perturbations are stabilized, but at the critical point the system makes a soft-type transition. When the parameter E_{ext} is increased beyond the critical point E_{c0} the system meets another transition point E_{c1}. For a certain value of E_{ext} between E_{c0} and E_{c1}, an unstable wave reaches a finite amplitude. Increase E_{ext} beyond E_{c1}, then waves can no longer remain at a finite amplitude but diverge within a finite time; he calls this an explosive instability. This transition is caused by the mode coupling process which acts to destabilize the initial unstable mode. He says also that, when unstable waves retain finite level, both the quasilinear and mode coupling processes stabilize them, and that which process dominates depends upon E_{ext} and upon other two parameters, α and ε where $\alpha = M_p/M_H$, $\varepsilon = E_{amb}/E_{c0} = D_\perp \kappa / M_p$. When $\alpha < 1$, the nonlinear behavior is mainly controlled by the quasilinear process, whereas for larger α and ε the mode coupling process also become important. Though Sato has made a mode coupling calculation under the random phase and single mode approximations, the theory developed shows an attractive example where mode coupling plays an important role in the nonlinear evolution of self-excited plasma waves.

The purpose of this paper is to study, by computer, how both the mode coupling and the quasilinear effect plays parts in the nonlinear quenching of the cross-field instability, and how the turbulent state is achieved. A computer study needs no *ad hoc* assumptions about the time evolution of the system, contrary to the theoretical studies described above. Computed results show that an initial irregularity is developed into strong turbulent state, and that a plateau is formed in the density profile and/or the field depending on boundary conditions. Some tendency of the recurrence is also found.

II. Basic Equations and System

The basic equations considered here are different from those of the one-dimensional model, i.e., the acceleration (inertia terms) can be neglected in the equations of motion of electrons and ions. Poisson's equation is not be taken into account, since the use of quasi-neutrality assumption has been verified in the one-dimensional model. Our concern is to events with frequency far lower than ν_i and ω_{Hi}. This allows the neglection of the acceleration terms. Thus, the governing equations are given by (in CGS EMU units)

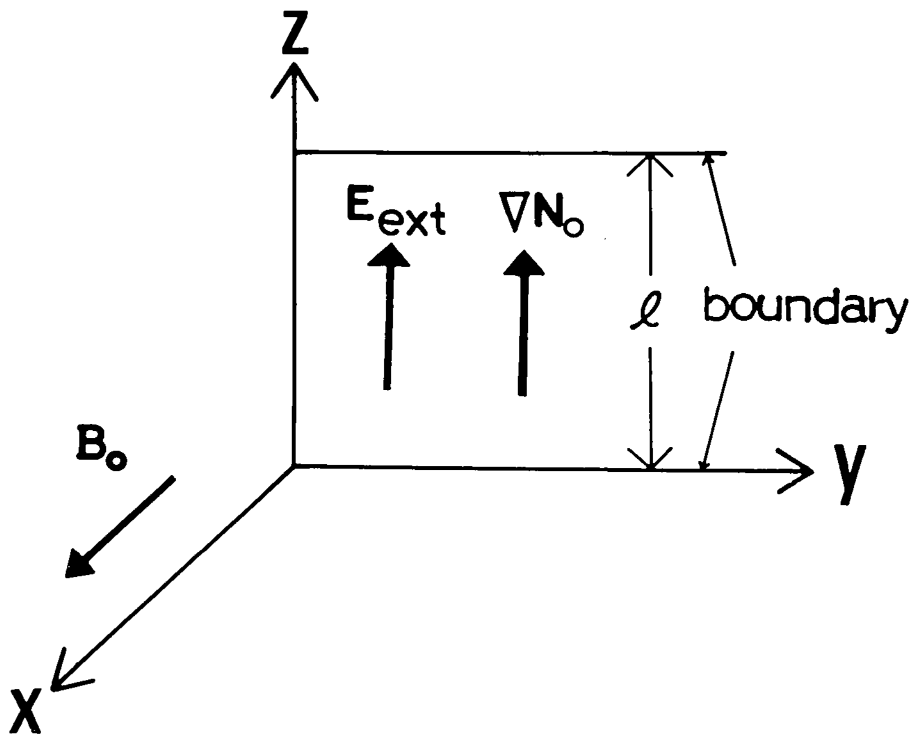

Fig. 3.1. Coordinate system. Two boundaries are set at z=0 and ℓ.

$$nm_\alpha \nu_\alpha \underset{\sim}{v}_\alpha = ne_\alpha \, (\underset{\sim}{v}_\alpha \times \underset{\sim}{B}_0 + \underset{\sim}{E}) - T_\alpha \nabla n, \tag{3·1}$$

$$\frac{\partial n}{\partial t} + \nabla \cdot (n \underset{\sim}{v}_\alpha) = 0 \qquad \alpha = e, i, \tag{3·2}$$

where the same notations are used as in the one-dimensional model, unless otherwise specified. The configuration of the system is shown in Fig. 3.1. Two boundaries are set at $z = 0, \ell$. Note that $\nabla n_0 = (0, 0, \frac{dn_0}{dz})$, $\underset{\sim}{E}_{ext} = (0, 0, E_{ext})$ and $\underset{\sim}{B}_0 = (B_0, 0, 0)$.

In the one-dimensional model, the background density distribution ia assumed to be exponential type $n_0(z) = N_0 e^{\kappa z}$. In the two-dimensional model, however, two types of the background density distribution are considered: One is exponential type and another is hyperbolic tangent type. The difference between these distributions is that dn_0/dz at $z = 0, \ell$ is far greater for exponential type than for hyperbolic tangent one. In the latter distribution we can regard approximately dn_0/dz at $z = 0, \ell$ as zero. This means that as is seen from linear analysis the cross-field instability does not occur near the boundaries. Accordingly, we can see that turbulent state appears all over the regions of z in the exponential distribution but in a restricted region of z, i.e., in the middle region in the hyperbolic tangent distribution. It may be said that the former and the latter distributions are found in laboratory experiment and in the ionospheric E layer, respectively.

We applied a constant E_{ext} along z in the one-dimensional model. This is removed in the two-dimensional model; potential, V, is fixed only at $z = 0, \ell$ (E_{ext} means $E_{ext} = (V_0 - V_\ell)/\ell$, hereafter unless otherwise noted).

(3.1) is rewritten as

$$nv_{\alpha y} = n\mu_p^\alpha E_y + n\mu_H^\alpha E_z - D_\perp^\alpha \frac{\partial n}{\partial y} - \mu_\alpha B_0 D_\perp^\alpha \frac{\partial n}{\partial z}, \qquad (3.3)$$

$$nv_{\alpha z} = -n\mu_H^\alpha E_y + n\mu_p^\alpha E_z + \mu_\alpha B_0 D_\perp^\alpha \frac{\partial n}{\partial y} - D_\perp^\alpha \frac{\partial n}{\partial z}. \qquad (3.4)$$

Substituting (3.3) and (3.4) into (3.2), we have

$$\frac{\partial n}{\partial t} + \mu_p^\alpha \frac{\partial nE_y}{\partial y} + \mu_H^\alpha \frac{\partial nE_z}{\partial y} - \mu_H^\alpha \frac{\partial nE_y}{\partial z} + \mu_p^\alpha \frac{\partial nE_z}{\partial z}$$

$$- D_\perp^\alpha \left(\frac{\partial^2 n}{\partial y^2} + \frac{\partial^2 n}{\partial z^2} \right) = 0 . \qquad (3.5)$$

(3.5) gives a set of equations as follows.

$$\frac{\partial n}{\partial t} - \mu_p^e \frac{\partial nE_y}{\partial y} + \mu_H^e \frac{\partial nE_z}{\partial y} - \mu_H^e \frac{\partial nE_y}{\partial z} - \mu_p^e \frac{\partial nE_z}{\partial z}$$

$$- D_\perp^e \left(\frac{\partial^2 n}{\partial y^2} + \frac{\partial^2 n}{\partial z^2} \right) = 0, \qquad (3.6)$$

$$M_p \frac{\partial n E_y}{\partial y} - M_H \frac{\partial n E_z}{\partial y} + M_H \frac{\partial n E_y}{\partial z} + M_p \frac{\partial n E_z}{\partial z}$$

$$- D_\perp \left(\frac{\partial^2 n}{\partial y^2} + \frac{\partial^2 n}{\partial z^2} \right) = 0 , \qquad (3.7)$$

where $M_p = \mu_p^e + \mu_p^i$, $M_H = \mu_H^e - \mu_H^i$, $D_\perp = D_\perp^i - D_\perp^e$. (3.6) is the equation of continuity of electrons and (3.7) means $\nabla \cdot \underset{\sim}{J} = 0$, $\underset{\sim}{J}$ being current. Hereafter E_y and E_z are replaced by $E_y = -\partial V/\partial y$ and $E_z = -\partial V/\partial z$. Equations to be solved as an initial-boundary value problem are (3.6) and (3.7). However, instead of solving (3.6) and (3.7) we introduce a spatial Fourier transformation with respect to independent variable y, because we are interested in the wave-wave interaction between harmonic waves propagating in the y direction, and in the deformation of background density and potential of the z direction. We note here that in the two-dimensional model of Sato and Tsuda(1968) and Tsuda et al.(1969) they introduce a spatial Fourier transformation with respect to y and z. This treatment may be appropriate to the case of free boundaries.

III. Machine Calculation

A. Scaling

We perform a scaling of variables as follows.

$$\eta = \frac{y}{L}, \qquad \zeta = \frac{z}{\ell}, \qquad \text{(distance)},$$

where L (= $2\pi/k_1$) is the largest wavelength of perturbation, k_1 being a fundamental wavenumber, and ℓ the distance between boundaries,

$$\tau = \frac{t}{T} \quad \text{(time) where} \quad T = \frac{L}{\mu_H^e E_{ext}},$$

$$\rho(\eta,\zeta,\tau) = \frac{n(y,z,t)}{N_0} \quad \text{(charge density)},$$

$$\psi(\eta,\zeta,\tau) = \frac{V(y,z,t)}{LE_{ext}} \quad \text{(potential)},$$

where N_0 is the background charge density at z =0. Two parameters of the length, ε and σ are defined by

$$\varepsilon = \frac{L}{\ell}, \qquad \sigma = \kappa\ell,$$

where κ^{-1} is the scale height of the background charge density. (3.6) and (3.7) are rewritten in dimensionless quantities defined above, as follows.

$$\frac{\partial\rho}{\partial\tau} + \varepsilon\{\frac{\partial}{\partial\zeta}(\rho\frac{\partial\psi}{\partial\eta}) - \frac{\partial}{\partial\eta}(\rho\frac{\partial\psi}{\partial\zeta})\} - A_1\varepsilon^{-1}(\frac{\partial^2\rho}{\partial\eta^2} + \varepsilon^2\frac{\partial^2\rho}{\partial\zeta^2})$$

$$+ A_2\{\frac{\partial}{\partial\eta}(\rho\frac{\partial\psi}{\partial\eta}) + \varepsilon^2\frac{\partial}{\partial\zeta}(\rho\frac{\partial\psi}{\partial\zeta})\}=0 , \qquad (3.8)$$

$$B_1\varepsilon\{\frac{\partial}{\partial\eta}(\rho\frac{\partial\psi}{\partial\zeta}) - \frac{\partial}{\partial\zeta}(\rho\frac{\partial\psi}{\partial\eta})\} - B_2\varepsilon^{-1}(\frac{\partial^2\rho}{\partial\eta 2} + \varepsilon^2\frac{\partial^2\rho}{\partial\zeta 2})$$

$$- B_3\{\frac{\partial}{\partial\eta}(\rho\frac{\partial\psi}{\partial\eta}) + \varepsilon^2\frac{\partial}{\partial\zeta}(\rho\frac{\partial\psi}{\partial\zeta})\} = 0 , \qquad (3.9)$$

where

$$A_1 = \frac{D_\perp^e}{\mu_H^e E_{ext}\ell} , \quad A_2 = \frac{\mu_p^e}{\mu_H^e} , \quad B_1 = \frac{M_H}{\mu_p^e} , \quad B_2 = \frac{D_\perp^e}{\mu_H^e E_{ext}\ell} ,$$

$$B_3 = \frac{M_p}{\mu_H^e} .$$

B. Numerical Procedure

We expand the dependent variables $\rho(\eta,\zeta,\tau)$ and $\psi(\eta,\zeta,\tau)$ into the Fourier series with respect to η , since we are interested in wave-wave interactions along the y direction. Fourier expansion is defined by

$$\rho(\eta,\zeta,\tau) = \sum_{n=-N}^{N} \tilde{\rho}_n(\zeta,\tau)\, e^{i2\pi n\eta},$$

$$\psi(\eta,\zeta,\tau) = \sum_{n=-N}^{N} \tilde{\psi}_n(\zeta,\tau)\ e^{i2\pi n\eta}.$$

We note here that the following relations must be held for $\tilde{\rho}_n$ and $\tilde{\psi}_n$;

$$\tilde{\rho}_n^* = \tilde{\rho}_{-n}\ ,\quad \tilde{\psi}_n^* = \tilde{\psi}_{-n}\ ,$$

where * denotes the complex conjugate. (3.8) and (3.9) are reduced to

$$\frac{\Delta\tilde{\rho}_n}{\Delta\tau} + 2\pi in \sum_{m=-N}^{N} \tilde{\rho}_{n-m}(2\pi imA_2 - \varepsilon\frac{\partial}{\partial\zeta})\ \tilde{\psi}_m$$

$$+ \varepsilon\frac{\partial}{\partial\zeta}\{\sum_{m=-N}^{N} \tilde{\rho}_{n-m}(2\pi im + A_2\varepsilon\frac{\partial}{\partial\zeta})\ \tilde{\psi}_m\}$$

$$- A_1\varepsilon^{-1}(\ -4\pi^2n^2 + \varepsilon^2\ \frac{\partial^2}{\partial\zeta^2})\ \tilde{\rho}_n = 0, \qquad (3.10)$$

$$2\pi in \sum_{m=-N}^{N} \tilde{\rho}_{n-m}(\ 2\pi imB_3 - B_1\varepsilon\frac{\partial}{\partial\zeta})\tilde{\psi}_m$$

$$+ \varepsilon\frac{\partial}{\partial\zeta}\{\ \sum_{m=-N}^{N} \tilde{\rho}_{n-m}(\ 2\pi imB_1 + B_3\varepsilon\frac{\partial}{\partial\zeta})\tilde{\psi}_m\}$$

$$+ B_2\varepsilon^{-1}(\ -4\pi^2n^2 + \varepsilon^2\ \frac{\partial^2}{\partial\zeta^2})\tilde{\rho}_n = 0, \qquad (3.11)$$

$$n,\ m = -N,\cdots, -1,\ 0,\ 1,\cdots,\ N,$$

where $\Delta\widetilde{\rho}_n$ and $\Delta\tau$ are the increment of $\widetilde{\rho}_n$ and the time step, respectively. Wave-wave interactions are described as the convolution terms in the equations. Here, n and m in (3.10) and (3.11) are normalized wavenumbers. Now we divide ℓ into several meshes. A mesh point is represented by

$$\zeta_m = m\,\Delta\zeta = \frac{m}{M}, \quad m = 0,\ 1,\ 2,\ \cdots\cdots\ M.$$

m = 0 and m = M correspond, respectively, to the lower and upper boundary.

The numerical procedure for the equilibrium is as follows: Give firstly the background distribution of an arbitrary form. Then the potential distribution in an equilibrium is obtained by solving (3.11). The procedure for the one-time step is as follows: Initial perturbation of the density is given to solve the potential by (3.11). Then (3.10) is used to know the new value of the density after $\Delta\tau$. This is again substituted in (3.11) to determine the potential.

It is self-evident that N and M should be as large as possible in order to avoid the numerical instability. This demands, however, large memory of computer and much computational time. As for the mode number N, the heuristic argument in one-dimensional model by Sato and Tsuda(1967) shows that the larger wavenumber components ($N = 40 \geq n > 10$) are not energetic enough to change the gross dynamical behavior of the small wavenumber components ($10 \geq n \geq 1$) through

Table 3.1. Parameters of computation.

Parameters	Case 1	Case 2
A_1	9.4×10^{-3}	9.4×10^{-3}
A_2	1.03×10^{-2}	1.03×10^{-2}
B_1	1	1
B_2	1.83×10^{-2}	1.83×10^{-2}
B_3	4.05×10^{-2}	4.05×10^{-2}
α	4.05×10^{-2}	4.05×10^{-2}
ε	2	4×10^{-1}
σ	2×10^{-1}	2×10^{-1}
N	8	8
M	6	8
T	4.4×10^{3}	8.8×10^{2}
$\Delta\zeta$	1.67×10^{-1}	1.25×10^{-1}
$\Delta\tau$	$1.14\times10^{-2} \sim 2.3\times10^{-3}$	$2.8\times10^{-2} \sim 2.3\times10^{-3}$
E_{ext}/E_{c0}	11	110
$\psi_0(1,\tau)$	-0.5	-2.5
$\psi_0(0,\tau)$	0	0
$\rho_0(1,\tau)$	e^{σ}	e^{σ}
$\rho_0(0,\tau)$	1	1
	$\tilde{\rho}_n(0,\tau)=\tilde{\rho}_n(1,\tau)=\tilde{\psi}_n(0,\tau)=\tilde{\psi}_n(1,\tau)=0 \quad n=1 \sim N$	
Initial condition	$\rho_0(\zeta,0)= e^{\sigma\zeta}$ $\mathrm{Re}\ \tilde{\rho}_1(\zeta,0)= 10^{-2}\rho_0(\zeta,0)\times\sin\pi\zeta$ $\mathrm{Im}\ \tilde{\rho}_1(\zeta,0)= 0$ $\tilde{\rho}_n(\zeta,0)= 0 \quad n= 2 \sim N$	

Table 3.1. (cont.).

Parameters	Case 3	Case 4
A_1	4.69×10^{-3}	6.25×10^{-4}
A_2	1.03×10^{-2}	1.03×10^{-2}
B_1	1	1
B_2	9.13×10^{-3}	1.22×10^{-3}
B_3	4.05×10^{-2}	4.05×10^{-2}
α	4.05×10^{-2}	4.05×10^{-2}
ε	5.52×10^{-1}	2.1×10^{-1}
σ	3.91	2.93
N	8	8
M	14	14
T	2.42×10^{3}	2.75×10^{2}
$\Delta\zeta$	7.1×10^{-2}	7.1×10^{-2}
$\Delta\tau$	$1.65\times10^{-2} \sim 8.3\times10^{-3}$	$9.1\times10^{-3} \sim 7.3\times10^{-4}$
E_{ext}/E_{c0}	11	55
$\psi_0(1,\tau)$	-1.82	-4.78
$\psi_0(0,\tau)$	0	0
$\rho_0(1,\tau)$	$0.125(9 + \tanh \frac{\sigma}{2})$	$0.25(5 + \tanh \frac{\sigma}{2})$
$\rho_0(0,\tau)$	$0.125\{9 + \tanh(-\frac{\sigma}{2})\}$	1
	$\tilde{\rho}_n(0,\tau)=\tilde{\rho}_n(1,\tau)=\tilde{\psi}_n(0,\tau)=\tilde{\psi}_n(1,\tau)=0 \quad n=1 \sim N$	
$\rho_0(\zeta,0)$	$0.125\{9 + \tanh\sigma(\zeta-\frac{1}{2})\}$	$0.25\{5 + \tanh\sigma(\zeta-\frac{1}{2})\}$
Initial condition	$\mathrm{Re}\ \tilde{\rho}_1(\zeta,0)= 10^{-2}\rho_0(\zeta,0)\times\sin\pi\zeta$	
	$\mathrm{Im}\ \tilde{\rho}_1(\zeta,0)= 0$	
	$\tilde{\rho}_n(\zeta,0)= 0 \quad n=2 \sim N$	

wave-wave interactions. According to this argument, it is expected that the time evolution of the system may well be pursuited with $N = 8$. The mesh number M of ζ direction is taken 6, 8, and 14.

C. Computed Results

In table 3.1 we list the parameters used in the computation. We calculated four cases, i.e., Cases 1, 2, 3, and 4. In Cases 1 and 2 an intial background density distribution of exponential type, $e^{\kappa z}$, is assumed (see Figs. 3.11 and 3.12). In Cases 3 and 4 hyperbolic tangent type distribution is assumed (see Figs. 3.13 and 3.14). We select the physical constants of the medium as $\mu_e B_0 = 10^2$, $\mu_i B_0 = 3 \times 10^{-2}$, $D_e = 4 \times 10^8$, and $D_i = 1.3 \times 10^5$ which are appropriate to the lower ionospheric E layer. The electric field E_{ext} and the layer width ℓ and fundamental wavenumber k_1 are as follows.

Case 1 $E_{ext} = 20$ emu, $\ell = 1$ km, $k_1 = 3.14 \times 10^{-5}$ /cm,

Case 2 $E_{ext} = 200$ emu, $\ell = 1$ km, $k_1 = 1.57 \times 10^{-4}$ /cm,

Case 3 $E_{ext} = 20$ emu, $\ell = 2$ km, $k_1 = 5.69 \times 10^{-4}$ /cm,

Case 4 $E_{ext} = 100$ emu, $\ell = 3$ km, $k_1 = 10^{-4}$/cm,

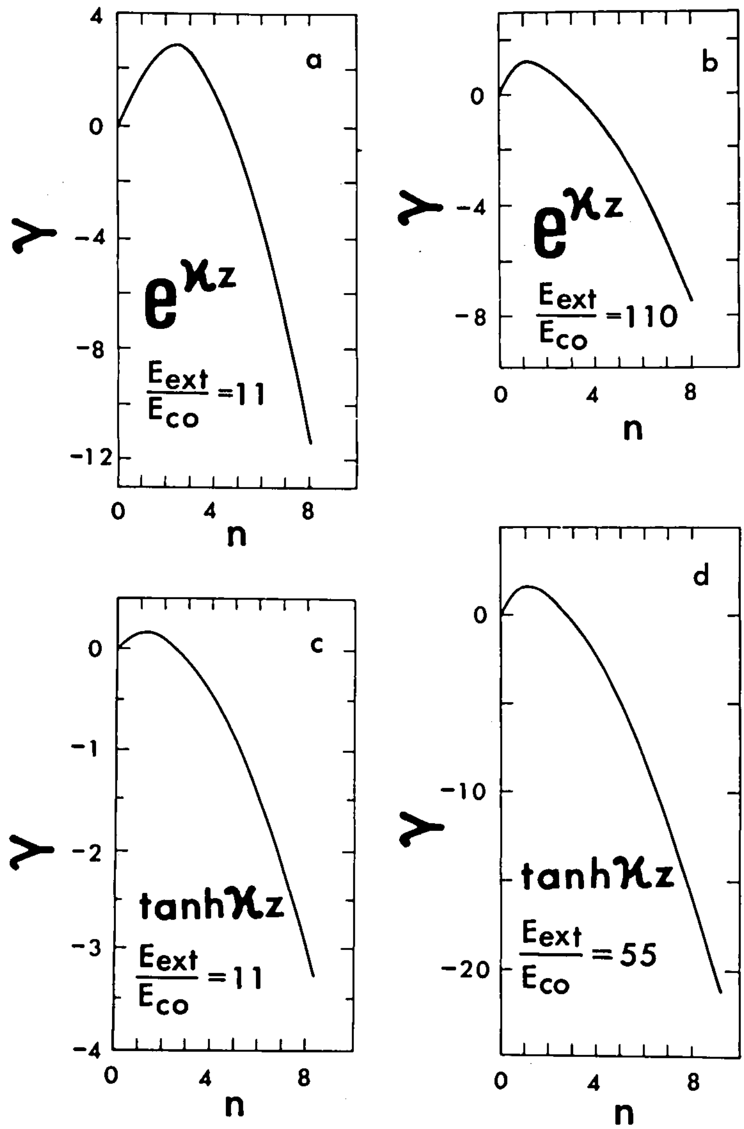

Fig. 3.2. Linear growth rate γ versus normalized wavenumber n. (a) Case 1, (b) Case 2, (c) Case 3, (d) Case 4. Cases 1 and 2 have the background density distribution of exponential type; $e^{\kappa z}$. Cases 3 and 4 have the background density distribution of hyperbolic tangent type; tanhκz. Note that except Case 1 we took the fundamental wavenumber (n=1) approximately equal to the wavenumber at which γ is maximized.

and κ is 2×10^{-6} /cm. E_{c0} in the table is given by $M_H \kappa (\mu_p^i D_\perp^e + \mu_p^e D_\perp^i)/M_p(\mu_p^i \mu_H^e + \mu_p^e \mu_H^i)$ (see, Sato(1971)). The normalized time $\tau = 1$ is T in real time as listed in Table 3.1. Boundary condition (at z = 0 and ℓ) is as follows;

$$\rho(y,0,t) = \rho(y,0,0) = \text{const.},$$

$$\rho(y,\ell,t) = \rho(y,\ell,0) = \text{const.},$$

$$\psi(y,0,t) = \psi(y,0,0) = \text{const.},$$

$$\psi(y,\ell,t) = \psi(y,\ell,0) = \text{const.}.$$

As an initial condition (at t = 0) we give monochromatic perturbation as shown in the table. Fig. 3.2 shows the growth rate versus dimensionless wavenumber $n(= k/k_1)$ calculated by the linear analysis (sato, 1971). In the following, we denote spectral density $|\tilde{\rho}_n|$ of m = i (i = 0,1,2,...,M) as $|\tilde{\rho}_n|_i$ for convenience.

Spectral Density

Case 1 Time evolution of the Fourier amplitude of density wave $|\tilde{\rho}_n|$ is shown in Fig. 3.3 for m = 1, 3 and 5. m =1 and 5 are the mesh points next to the lower and upper boundaries,

Fig. 3.3. Time evolution of Fourier amplitudes of density wave ($|\tilde{\rho}_n|$) for Case 1. $|\tilde{\rho}_n|$ versus time τ is shown. The number labeled on each curve means the normalized wavenumber n.

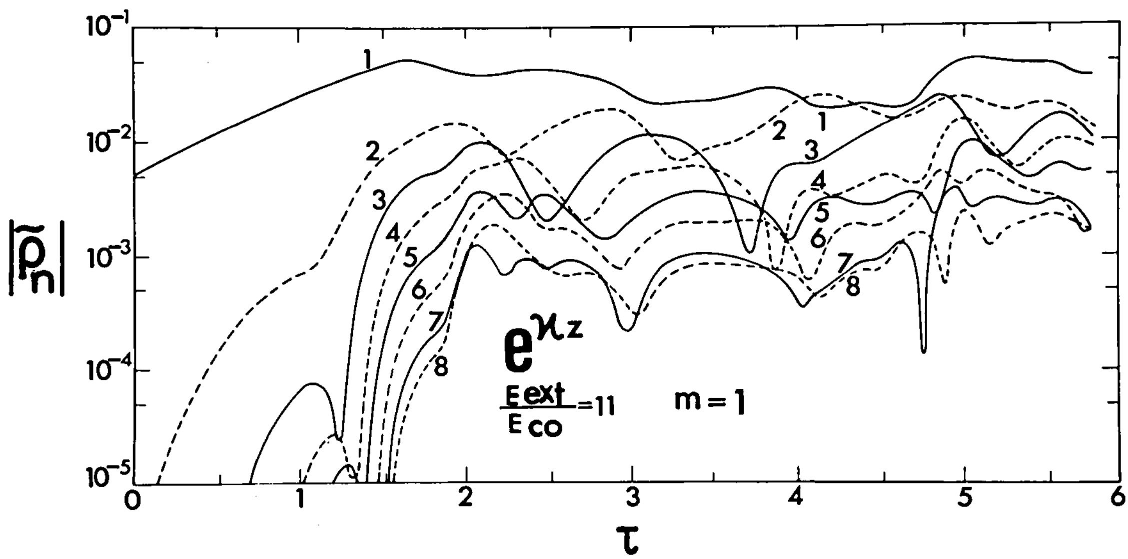

Fig. 3.3a. m=1 (ζ =1/6).

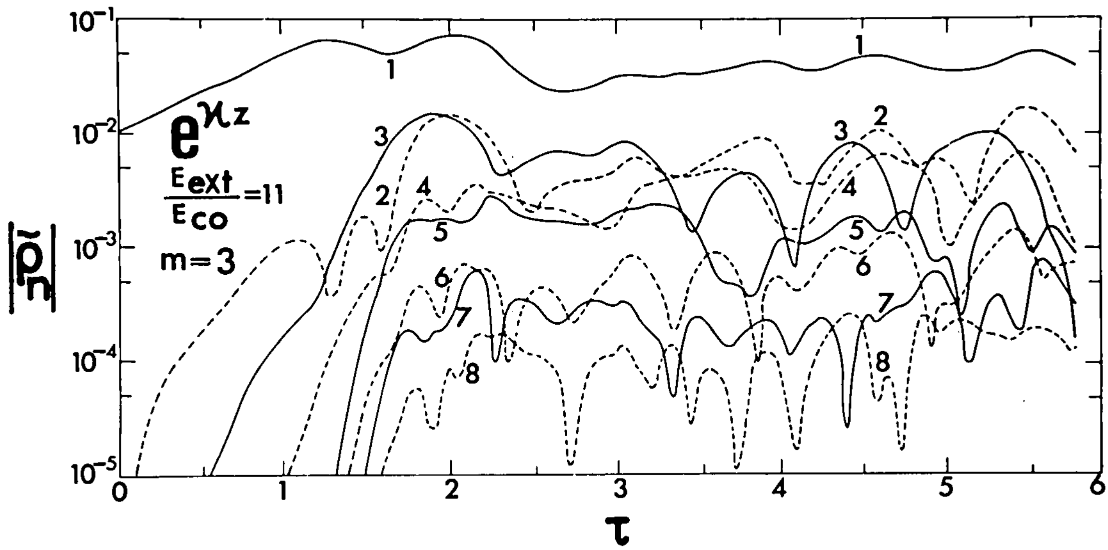

Fig. 3.3b. m=3 (ζ =3/6).

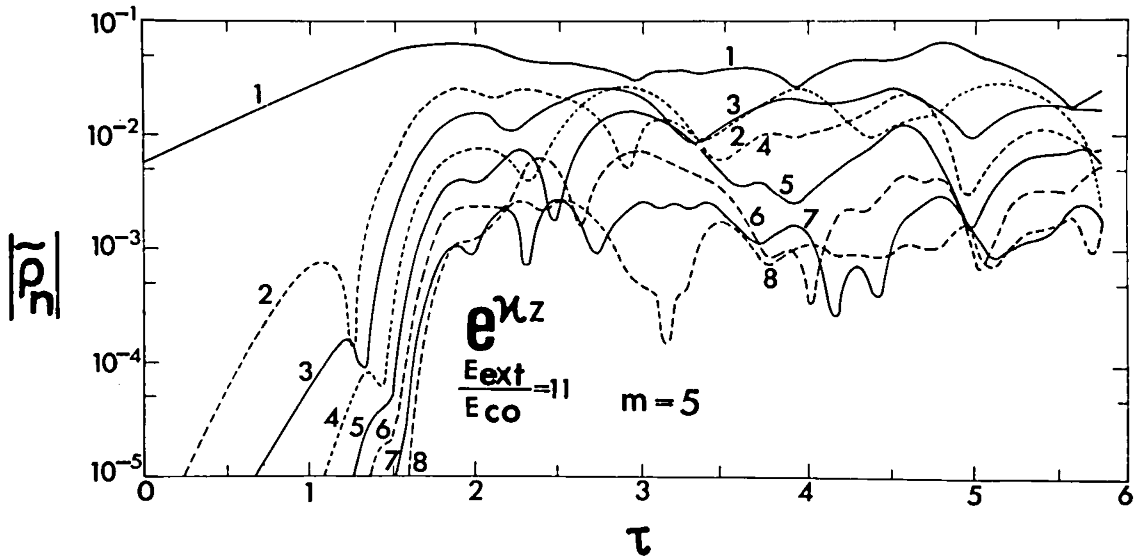

Fig. 3.3c. m=5 (ζ =5/6).

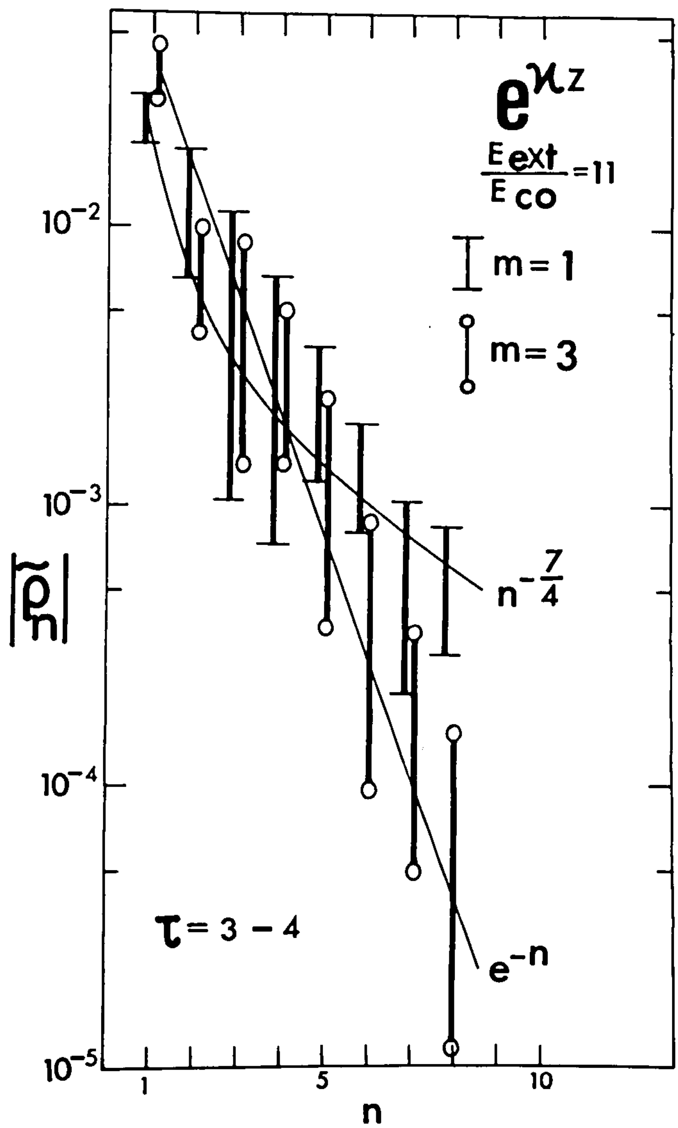

Fig. 3.4. Amplitude distribution of density wave ($|\tilde{\rho}_n|$) for Case 1. $|\tilde{\rho}_n|$ versus normalized wave-number n at m=1 (ζ=1/6) and 3 (ζ=3/6) is shown during τ=3 ~ 4. Two solid curves are drawn for the reference. It is seen that $|\tilde{\rho}_n|$ obeys $n^{-7/4}$ and e^{-n} at m=1 and 3 respectively.

respectively, while m = 3 is the middle point. The fundamental wavelength was taken to be 2 km. After the linear growth, $|\tilde{\rho}_1|$ saturates at $\tau=1.2 \sim 1.8$ and amounts to $5 \sim 7$ % of the background density ρ_0. As is seen, the system keeps rather steady turbulent state after the saturation. Strictly speaking, however, $|\tilde{\rho}_1|_{1,5}$ decreases slowly, and around $\tau = 5$, $|\tilde{\rho}_1|_{1,5}$ starts to increase and is restored to the level of the initial saturation, though $|\tilde{\rho}_1|_3$ has no such indication. The computation was stopped at $\tau = 5.7$ when $|\tilde{\rho}_1|_5$ again starts to decrease. In turbulent state, we find rather regular modulation of $|\tilde{\rho}_n|_{1,5}$, but somewhat irregular modulation of $|\tilde{\rho}_n|_3$. Let us confine ourselves to the behavior of $|\tilde{\rho}_n|_1$ around $\tau = 3$ and 3.7: We find that at $\tau = 3$ $|\tilde{\rho}_1|$ and $|\tilde{\rho}_2|$ are decreasing whereas all other $|\tilde{\rho}_n|$ (n=3,4,....,N) are increasing, and vice versa at $\tau = 3.7$. The same behavior also appears in $|\tilde{\rho}_n|_5$. $|\tilde{\rho}_n|_3$ is not so regular but seemingly random. Noteworthy is that the decrease or increase of $|\tilde{\rho}_1|_1$ and $|\tilde{\rho}_1|_5$ is followed by the increase or decrease of large wavenumber components with a certain delay of time. This indicates an important clue to the mechanism of energy transfer between the modes. By comparing $|\tilde{\rho}_n|_{1,5}$ and $|\tilde{\rho}_n|_3$, it is seen that the mode coupling process is more violent in the vicinity of boundaries, and quasilinear process is more important in central regions. These results are justified judging from the indication of Fig. 3.11 and are consistent with Sato's criterion (Sato, 1971) that if E_{ext}

is below a critical value E_{c1}, both quasilinear and mode coupling processes stabilize the unstable waves; in the present case $E_{ext}/E_{c1} \sim 0.9$ at $\tau = 0$. We note that the quenching of amplitude at $\tau = 1.2 \sim 1.8$ is mainly achieved by the falttening of the background density ρ_0, not by the shielding of the external electric field. Since this point is important, we shall discuss later in more detail.

Fig. 3.4 shows examples of amplitude distribution versus normalized wavenumber n between $\tau = 3 \sim 4$. From the figure it is seen that the turbulent spectrum $I_n = |\tilde{\rho}_n \tilde{\rho}_n^*|$, shows an exponential type $e^{-\alpha n}$ ($\alpha = 1 \sim 2$) at m = 3 and a power type $n^{-\alpha}$ ($\alpha = 3 \sim 4$) at m = 1 (and 5; not shown). Again this indicates that in the neighborhood of boundaries, mode coupling is important but not in the central regions.

Case 2 Fig, 3.5 shows another computed example for an exponential background density. E_{ext} is taken to be ten times larger than that of Case 1. According to the theory, this case corresponds to an explosive instability, because $E_{ext} \gg E_{c1} \sim 12E_{c0}$. $|\tilde{\rho}_1|_4$, of central regions, saturates at $\tau = 1.9$ with the relative amplitude of 6 % and starts to decrease up to the initial state. On the other hand, $|\tilde{\rho}_1|_1$ and $|\tilde{\rho}_1|_7$ near boundaries once saturate at $\tau = 2.1$, again growing to 12 $\sim$ 15 %. Unfortunately, we meet a numerical instability at $\tau = 3.4$, and therefore it is impossible to have

Fig. 3.5. Same as Fig. 3.3, except for Case 2.

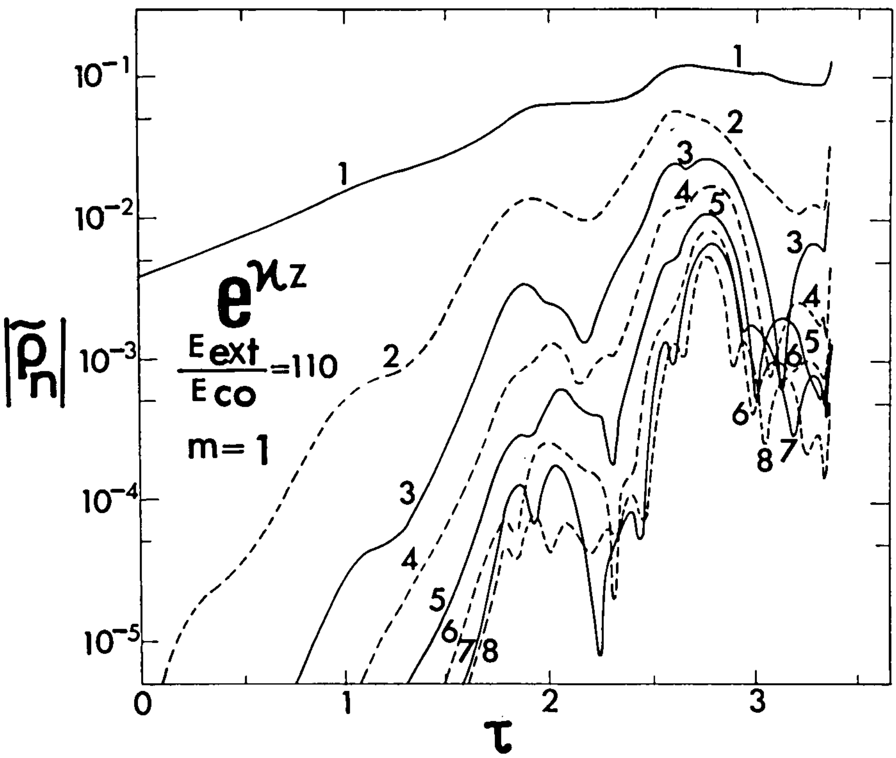

Fig. 3.5a. m=1 (ζ=1/8).

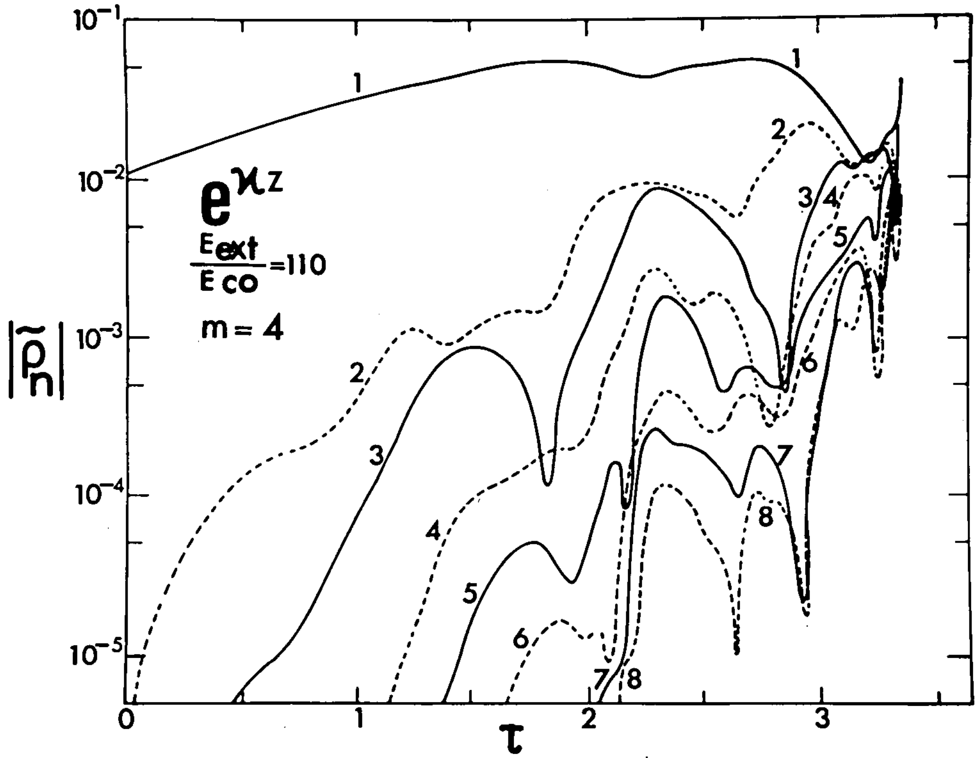

Fig. 3.5b. m=4 (ζ=4/8).

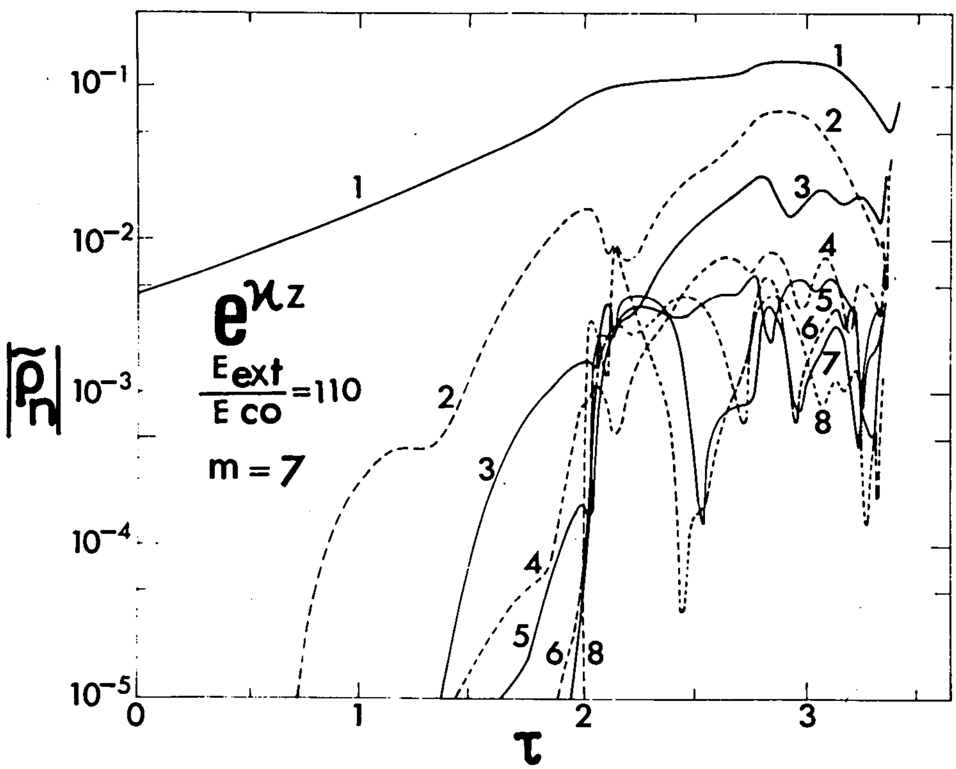

Fig. 3.5c. m=7 (ζ=7/8).

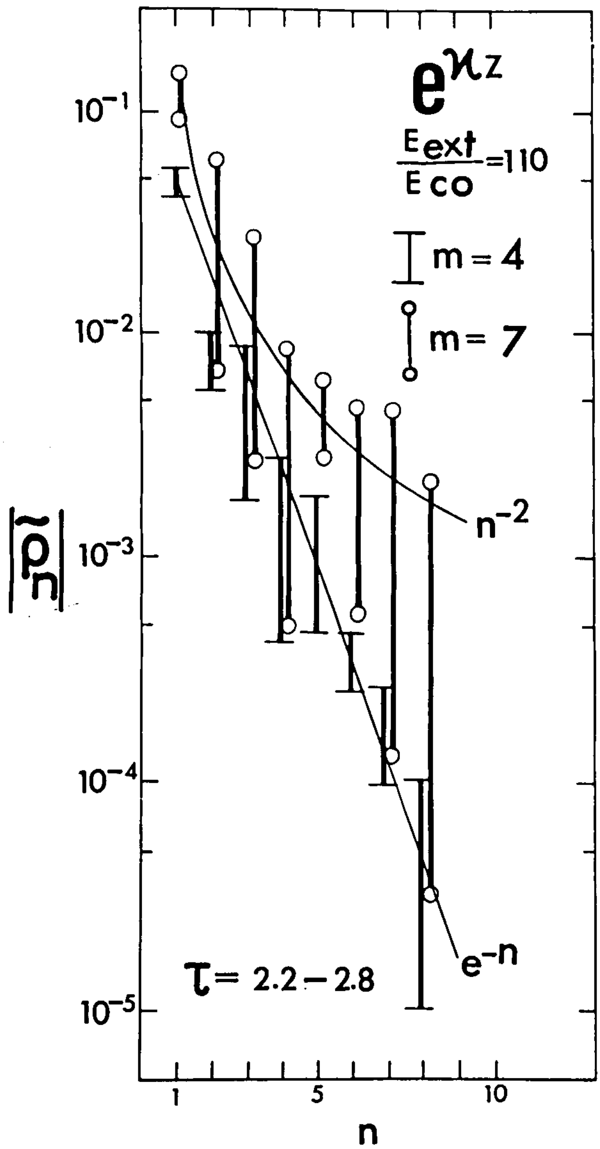

Fig. 3.6. Amplitude distribution of density wave ($|\tilde{\rho}_n|$) for Case 2. $|\tilde{\rho}_n|$ versus normalized wave-number n at m=4 (ζ=4/8) and 7 (ζ=7/8) is shown during τ=2.2 ~ 2.8. It is seen that $|\tilde{\rho}_n|$ obeys e^{-n} and n^{-2} at m=4 and 7 respectively.

subsequent informations. It is not clear whether this numerical instability is due to the coarse mesh width of ζ direction or due to the small N (= 8). Comapring to Case 1, we see that $|\tilde{\rho}_n|_{1,7}$ behaves in a body as a whole; that is, small wavelength components increase when long wavelength components increase and <u>vice versa</u>. Accordingly we cannot recognize the ordered exchange of energies between harmonic waves. This contrasts with Case 1 in which the ordered exchange has been observed. $|\tilde{\rho}_n|_4$, on the contrary, behaves gently as in Case 1. We note that the behavior of $|\tilde{\rho}_n|_1$ shows a close resemblance to Fig. 5 of Sato et al.(1967) in the one-dimensional model ($E_{ext}/E_{c0} = 57$).

Examples of amplitude distribution at m = 4 and 7 between $\tau = 2.2 \sim 2.8$ are shown in Fig. 3.6. It is obtained that $I_n \propto n^{-\alpha}$ ($\alpha \sim 4$) at m = 7, and that $I_n \propto e^{-\alpha n}$ ($\alpha \sim 2$) at m = 4. It is easily seen from Figs. 3.5 and 3.6 that the spectrum is harder near boundaries than around central regions.

We infer that after $\tau = 3.4$ the system becomes more turbulent than before.

<u>Case 3</u> A hyperbolic tangent type distribution is chosen as the background density distribution. In the computation, $\rho_0(1,0)$ was taken as $1.25\,\rho_0(0,0)$, and $\frac{d\rho_0}{d\zeta}$ at $\zeta = 0$ and 1 was taken as $\frac{1}{13}\,\frac{d\rho_0(1/2,0)}{d\zeta}$. Fig. 3.13 ($\tau = 0$) shows such

Fig. 3.7. Same as Fig. 3.3, except for Case 3.

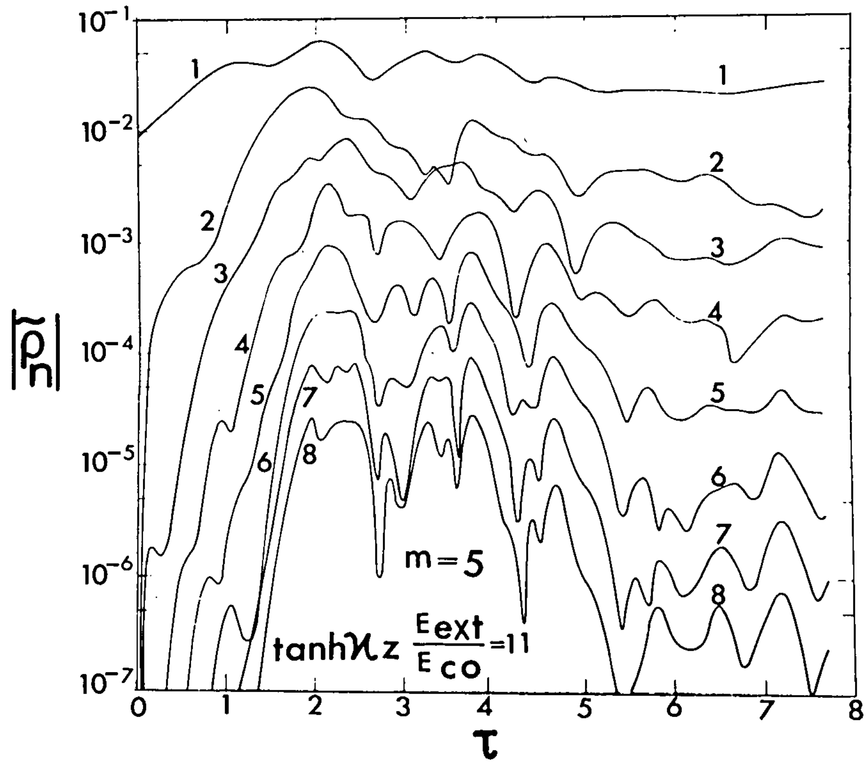

Fig. 3.7a. m=5 (ζ=5/14).

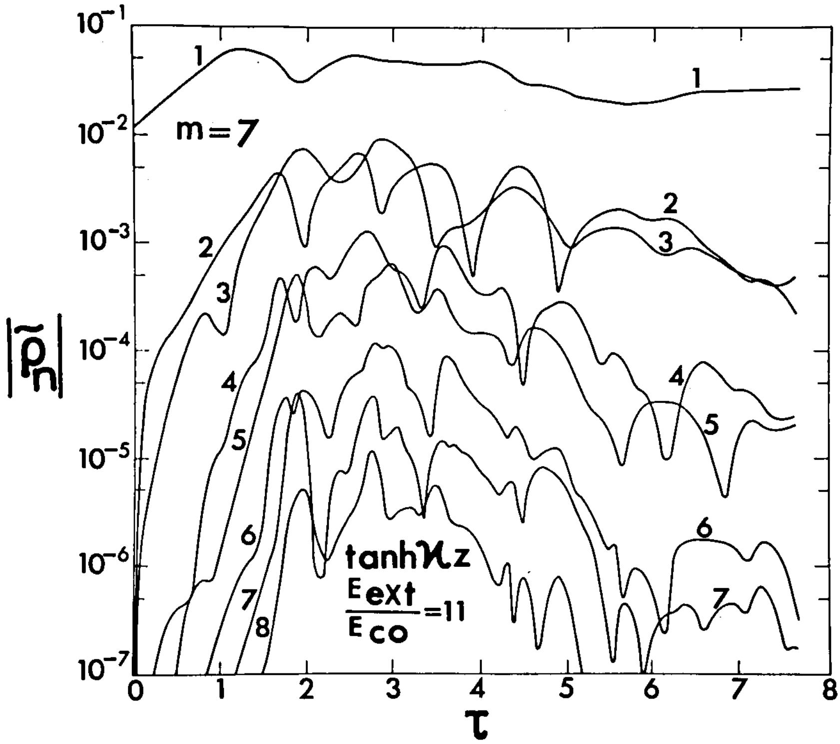

Fig. 3.7b. m=7 (ζ=7/14).

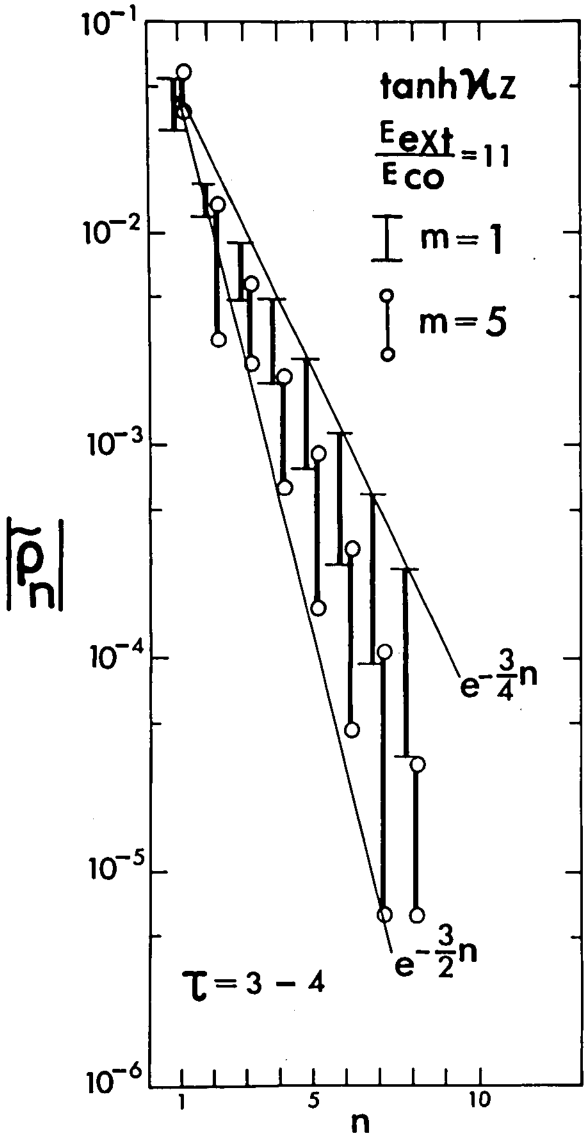

Fig. 3.8. Amplitude distribution of density wave ($|\tilde{\rho}_n|$) for Case 3. $|\tilde{\rho}_n|$ versus normalized wave-number n at m=1(ζ=1/14) and 5(ζ=5/14) is shown during τ=3 ~ 4. It is seen that $|\tilde{\rho}_n|$ obeys $e^{-3n/4}$ and $e^{-3n/2}$ at m=1 and 5 respectively.

a distribution. From this distribution it is expected that the instability would not occur near both boundaries, at least, at the initial stage of the evolution.

Fig. 3.7 illustrates the time evolution of $|\tilde{\rho}_n|_5$ and $|\tilde{\rho}_n|_7$. After the linear growth, $|\tilde{\rho}_1|$ is quenched at $\tau = 1.2$, having an amplitude of 5 %. Thereafter $|\tilde{\rho}_1|$ fluctuates more or less though the average amplitude gradually decreases. Such a trend is seen in the evolution of other higher harmonic waves. After $\tau = 5$, we see that the equilibrium state continues until the computation was stopped at $\tau = 7.7$.

Amplitude distribution between $\tau = 3 \sim 4$ at m = 1 and 5 is shown in Fig. 3.8. From this it is seen that $I_n \propto e^{-\alpha n}$ with $\alpha = 1.5 \sim 3$. Note that the spectrum at m = 1 is harder than at m = 5.

<u>Case 4</u> The background density distribution was modified from that of Case 3 in such a way that $\rho_0(1,0)$ is 1.5 $\rho_0($0,0), and that $\frac{d\rho_0(1,0)}{d\zeta}$ is $\frac{1}{5.5}\frac{d\rho_0(1/2,0)}{d\zeta}$, and that $\frac{d\rho_0(0,0)}{d\zeta}$ is almost the same as $\frac{d\rho_0(1/2,0)}{d\zeta}$. This distribution is shown in Fig. 3.14 ($\tau = 0$). From this figure we expect that the turbulence would appear more easily in the vicinity of the lower boundary than the upper boundary.

In Fig. 3.9 shown are $|\tilde{\rho}_n|_5$ and $|\tilde{\rho}_n|_7$ for comparison. $|\tilde{\rho}_1|_5$ and $|\tilde{\rho}_1|_7$ are quenched at $\tau = 1.6$ and 1.4, respectively, with the amplitude of 10 %. Thereafter $|\tilde{\rho}_n|_5$ ($n \gtrsim 2$) tends to

Fig. 3.9. Same as Fig. 3.3, except for Case 4.

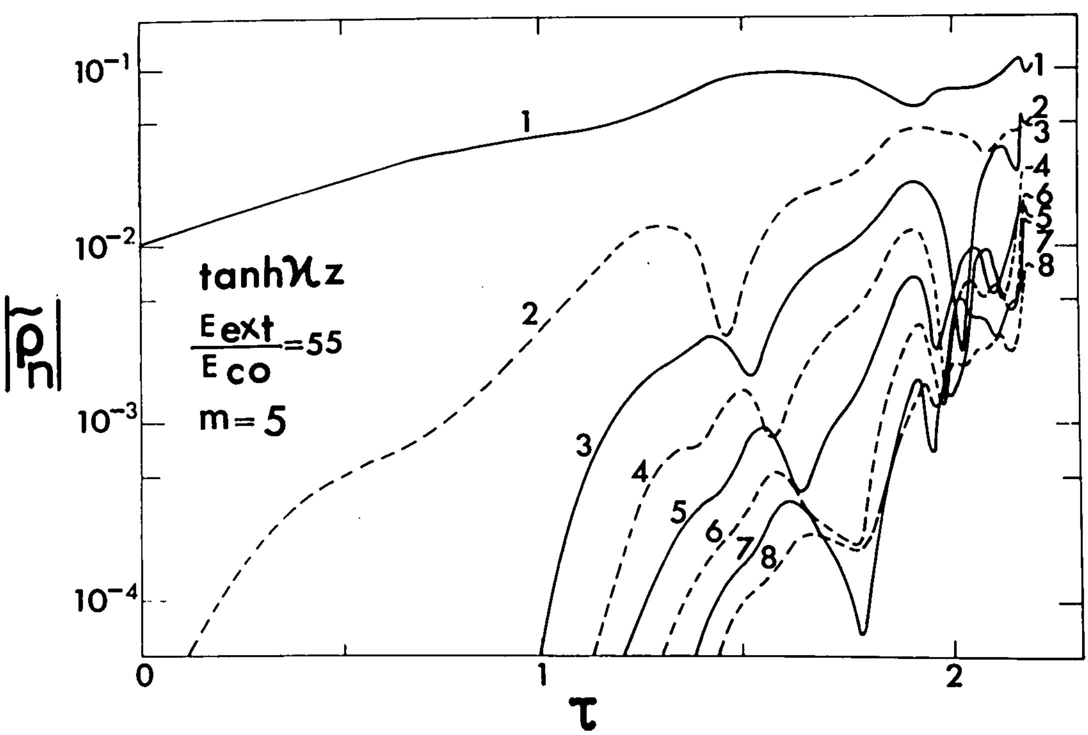

Fig. 3.9a. m=5 (ζ=5/14).

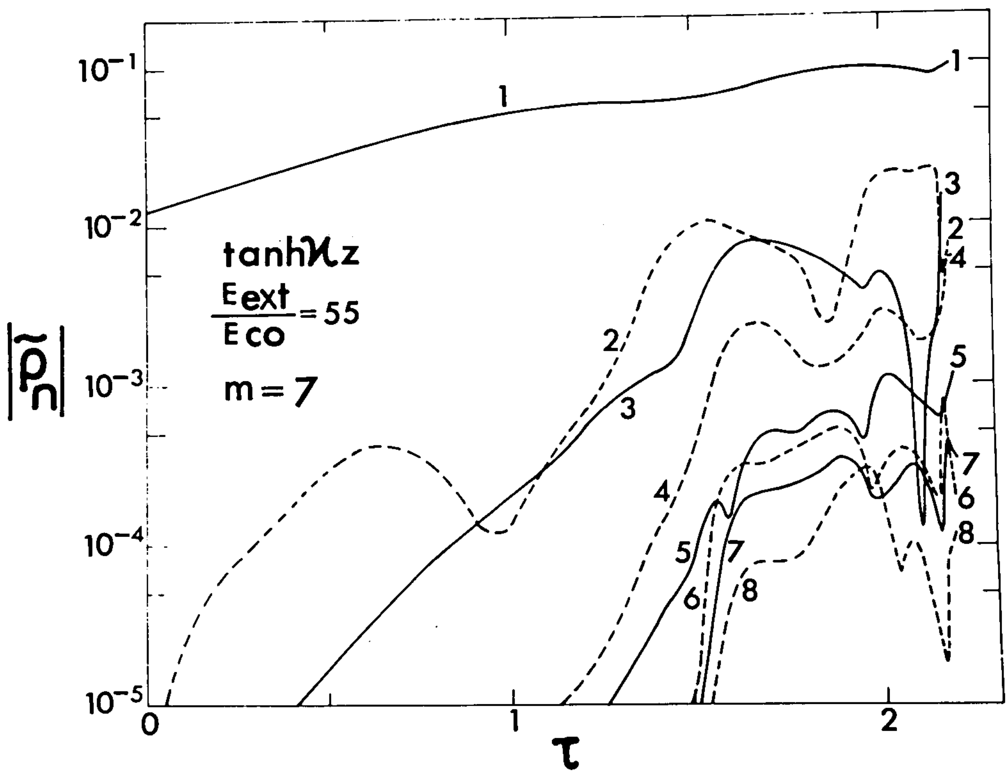

Fig. 3.9b. m=7 (ζ=7/14).

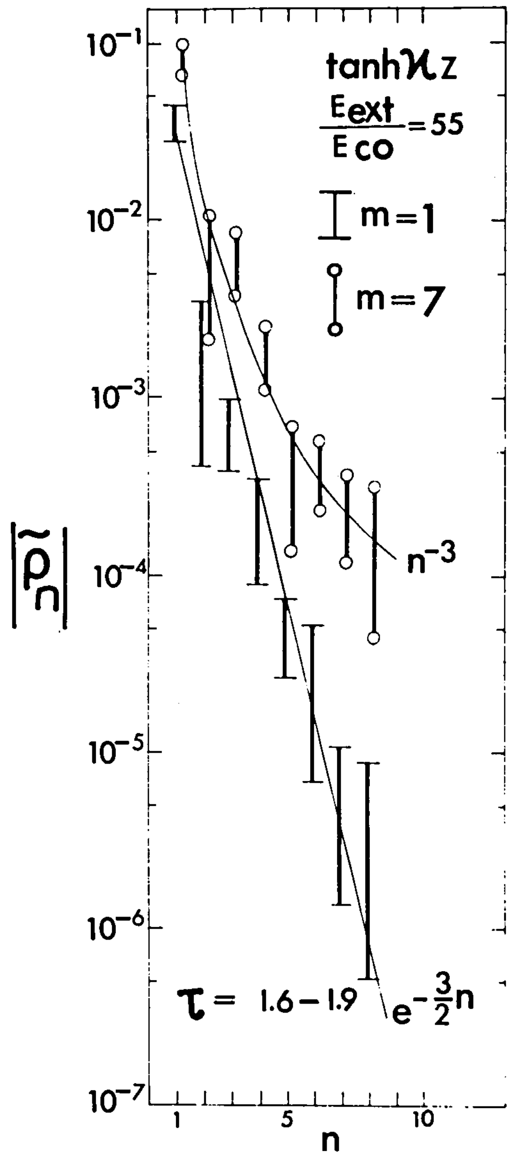

Fig. 3.10. Amplitude distribution of density wave ($|\tilde{\rho}_n|$) for Case 4. $|\tilde{\rho}_n|$ versus normalized wave-number n at m=1(ζ=1/14)and 7(ζ=7/14) is shown during τ=1.6 ~ 1.9. It is seen that $|\tilde{\rho}_n|$ obeys $e^{-3n/2}$ and n^{-3} at m=1 and 7 respectively.

increase as a whole, eventually followed by numerical instability at about $\tau = 2.2$. $|\tilde{\rho}_n|_7$ ($n \gtrsim 2$), however, shows a rather gentle behavior. $|\tilde{\rho}_n|_5$ shows the ordered exchange of energies between harmonic waves for the time between $\tau = 1.2 \sim 1.8$. On the other hand, $|\tilde{\rho}_n|_7$ does not such a behavior. This may be due to the difference of deformed background density distribution from place to place. We note that Case 4 develops into strong turbulence, because $E_{ext}/E_{c0} = 55$.

Fig. 3.10 shows amplitude distributions between $\tau = 1.6 \sim 1.9$ at m = 1 and 7. It is seen that $I_n \propto e^{-3n}$ at m = 1 and that $I_n \propto n^{-6}$ at m = 7, suggesting turbulences to be stronger in central regions than near both boundaries.

In summary we point out a few characteristics of the time evolution of $|\tilde{\rho}_n|$ found by the computations as follows:

1. After a linear growth, $|\tilde{\rho}_1|$ is quenched and its saturation level varies depending on the strength of the electric field. The amplitude of $|\tilde{\rho}_1|$ does not hold a certain level but changes in somewhat regular fashion. $|\tilde{\rho}_n|$ ($n \gtrsim 2$) is also quenched once, and then develops into a turbulent state. When $E_{ext} > E_{c1}$ (Cases 2 and 4), the system results in a strong turbulence. On the other hand, when $E_{ext} < E_{c1}$ (Cases 1 and 3), the system behaves gently for

a long time.

2. We find that the ordered exchange of oscillation energies between harmonic waves is observed in some limited regions in Cases 1 and 4.

3. In a turbulent state, density spectrum I_n obeys a power law or exponential law, depending on conditions; i.e., I_n is given as $n^{-\alpha}$ and $e^{-\alpha n}$ depending on regions to which our concern is confined. We cannot deduce clear dependence of the index α on the external electric field. However, it should be remarked that whether spectrum becomes soft or hard depends largely on profiles of background density and potential which supply the energy to waves.

Deformation of Background Density and Potential

As was described previously, the essential difference between one- and two-dimensional models lies on whether or not interactions between background density $\rho_0(z)$, potential $\psi_0(z)$ and propagating waves in the y direction are taken into account. The most significant profit of the two-dimensional calculation is in that we can visualize a time evolution of $\rho_0(z)$ and $\psi_0(z)$ and know how the nonlinear quenching of $|\tilde{\rho}_n|$ is achieved.

<u>Case 1</u> Fig. 3.11 shows the distribution of ρ_0 and ψ_0 at

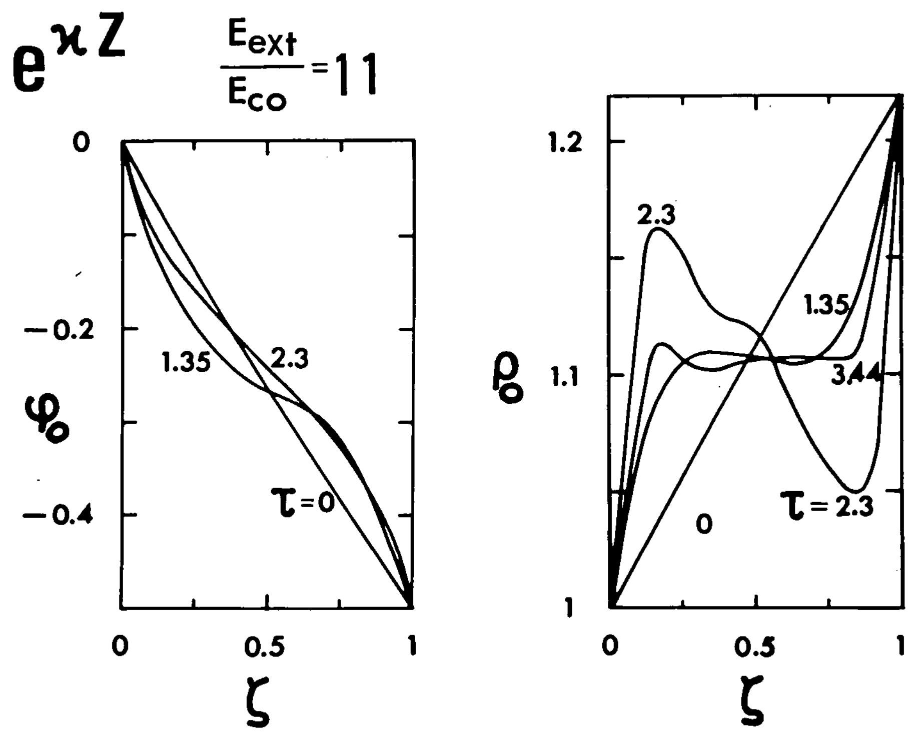

Fig. 3.11. Time evolution of background potential (ψ_0) and density (ρ_0) distributions for Case 1. ψ_0 and ρ_0 versus ζ are shown. Initial distribution is assigned to time τ=0.

several times. Initial distribution is assigned by $\tau = 0$. As time goes on, ρ_0 once flattens in central regions around $\tau = 1.35$ and keeps deforming until $\tau = 2.3$. After this time the distribution starts to return to the previous state, and again flattens (see $\tau = 3.44$). For some time the flattened distribution continues. Around $\tau = 4.5$, it starts again to deform clearly, resulting in somewhat irregular shape. The trend of the flattening is retrieved around $\tau = 5.5$. Thereafter the computation was stopped at $\tau = 5.7$.

On the other hand, the flattening of ψ_0 appears at $\tau = 1.35$ which is not so clear compared to ρ_0. After this time, the distribution keeps the state similar to that of $\tau = 2.3$. Therefore it is concluded that in this case the flattening of the potential is not so important.

Keeping in mind these results, we discuss again the time evolution of $|\tilde{\rho}_k|$ (Fig. 3.3) as follows.

1. The saturation of $|\tilde{\rho}_1|$ seen at $\tau = 1.2 \sim 1.8$ is achieved by both the flattenings of ρ_0 and ψ_0, the former being of much importance for the present case. The decrease of $|\tilde{\rho}_1|_3$ around $\tau = 2.3$ is well correlated with the inverse gradient of ρ_0. The large increase of $|\tilde{\rho}_1|_1$ and $|\tilde{\rho}_1|_5$ around $\tau = 4 \sim 4.7$ is initiated by the deformation of ρ_0, the distribution of which have retained a clear flattening till $\tau = 4$.

2. As was pointed out previously, in a steady turbulent state the energy of $|\tilde{\rho}_1|_1$ or $|\tilde{\rho}_1|_5$ is transferred into smaller wavelength components in a regular fashion. This is understood in terms of the density and/or potential flattenings, i.e., the energy decrease of $|\tilde{\rho}_1|_1$ or $|\tilde{\rho}_1|_5$ appears in accord with the time when the density flattening occurs, and the increase is correlated with a little breakdown of the density flattening. The oscillation energy of $|\tilde{\rho}_1|$ is, through mode coupling, transferred gradually with a time scale of 1 to smaller wavelength components, where the oscillation energy is partly dissipated by classical diffusion. Another part of energy is fed back to ρ_0 and ψ_0 through quasilinear effect. Thus we can recognize the energy flow from the supplier to the consumer.

3. We find rather cyclic growth and decay of $|\tilde{\rho}_n|$, resulting from the deformation of ρ_0 and ψ_0.

4. The density spectrum I_n becomes softer at m = 3 than at m = 1, 5 due to the flattening of ρ_0. This agrees with the previous result; $I_n \propto e^{-\alpha n}$ at m = 3 and $I_n \propto n^{-\alpha}$ at m = 1 and 5.

<u>Case 2</u> This case resulted in a stronger turbulence than Case 1, and eventually we met numerical instability. Fig. 3.12 shows the time evolution of ρ_0 and ψ_0 of Case 2. As is seen in the figure, the trend of the flattenings of ρ_0

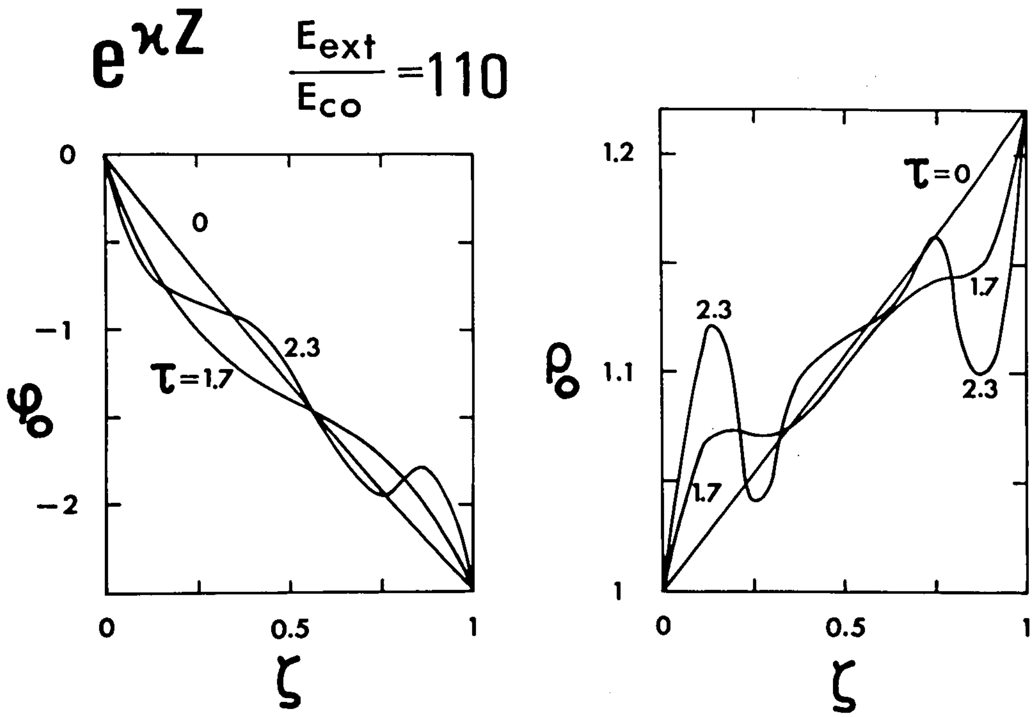

Fig. 3.12. Same as Fig. 3.11, except for Case 2.

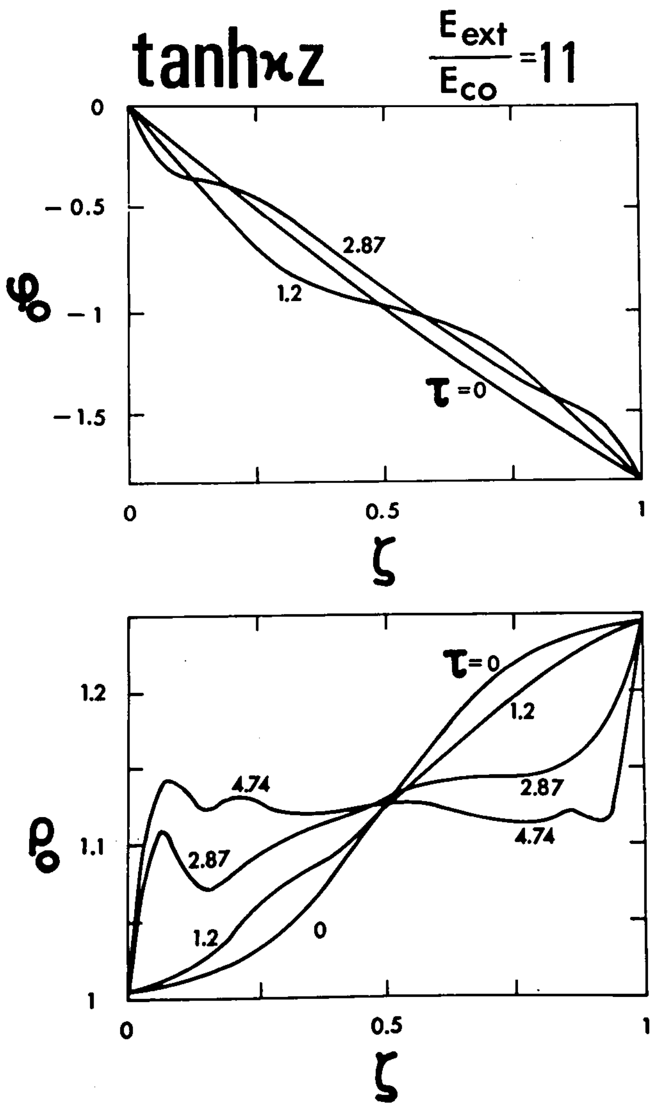

Fig. 3.13. Same as Fig. 3.11, except for Case 3.

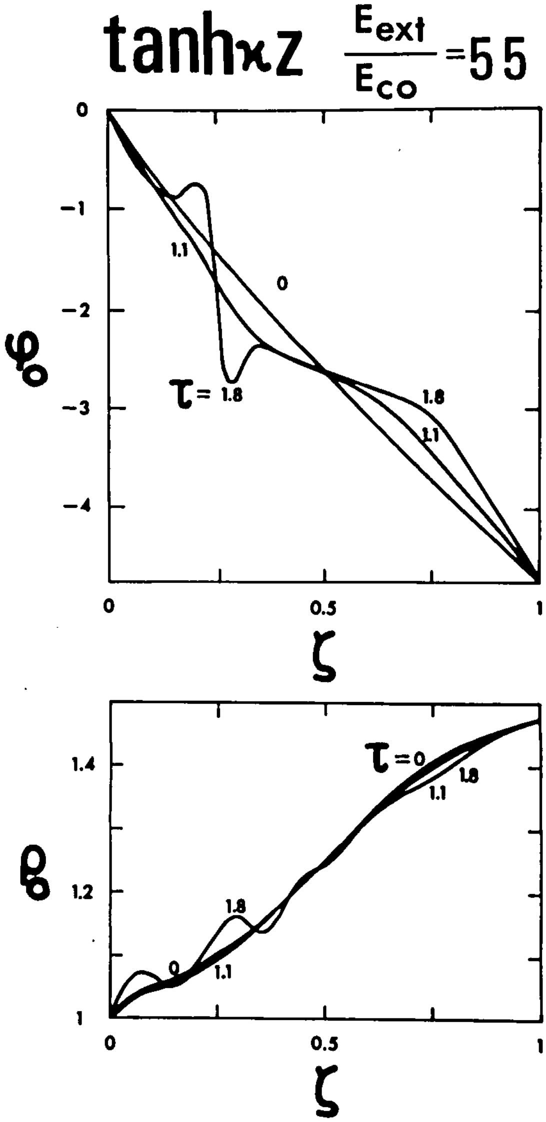

Fig. 3.14. Same as Fig. 3.11, except for Case 4.

and ψ_0 is obvious around $\tau = 1.7$, though not so prominent as Case 1. With the passage of time, both ρ_0 and ψ_0 are deformed in an irregular manner. We cannot tell whether these irregular deformations represent the real behavior of the system or some indication of numerical instability.

<u>Case 3</u> In this case, the evolution of $|\tilde{\rho}_n|$ is rather regular and the amplitude tend to decrease with the passage of time. Fig. 3.13 shows the time evolution of ρ_0 and ψ_0. At $\tau =$ 1.2 when $|\tilde{\rho}_1|$ saturates at first, we cannot see so much the flattening of ρ_0 as that of ψ_0. This result clearly contrasts with that of Case 1. As times go on, however, the flattening of ρ_0 becomes distinguished, while the distribution of ψ_0 fluctuates. We can see the density flattening at $\tau = 4.74$ all over the regions except near both ends. This is the reason why all waves subside gradually.

<u>Case 4</u> Fig. 3.14 shows the time evolution of ρ_0 and ψ_0. This figure indicates that ρ_0 deviates hardly from the initial distribution until $\tau = 1.1$, more to say $\tau = 1.5$ (not shown) and some wavy structure appears and grows as time goes on. ψ_0, on the other hand, continues to be deformed in a clear manner till $\tau = 1.1$ and forms the clear flattening. But the shape is destroyed once ($\tau = 1.45$) and then restores the flattening around $\tau = 1.8$, though partially kinked. After $\tau = 1.8$, ρ_0 becomes irregular. The initial quenching of

$|\tilde{\rho}_1|_5$ and $|\tilde{\rho}_1|_7$ around $\tau = 1.3$ (see Fig. 3.9) in this case is well correlated with the vanishing of the electric field but not that of ρ_0.

As a summary of this subsection, we point out that which flattening, ρ_0 or ψ_0, is more important for the saturation of the instability depends largely on a boundary condition. If either of $d\rho_0/d\zeta$ and $d\psi_0/d\zeta$ remains to be zero, the energy flow to unstable waves is shut off and the amplitude of waves is decreased by the energy cascade to smaller wavelength components. However, it is likely that the profile of ρ_0 and ψ_0 is again deformed by the feedback of oscillating energy to ρ_0 and ψ_0, and/or by some locally existing steep gradient of density. Thus the cyclic behaviors of $|\tilde{\rho}_n|$ as shown in Figs. 3.3, 3.5, 3.7, and 3.9 seem to be caused by the competition between quasilinear and mode coupling effects. When $E_{ext} > E_{c1}$, mode coupling process predominates quasilinear one, so that the flattening is not achieved so much clearly as in the case of $E_{ext} < E_{c1}$. Then we have a strongly turbulent state.

Density Irregularity

Spatial irregularity patterns at a time τ in the (y,z) plane are shown in Figs. 3.15 and 3.16. We have

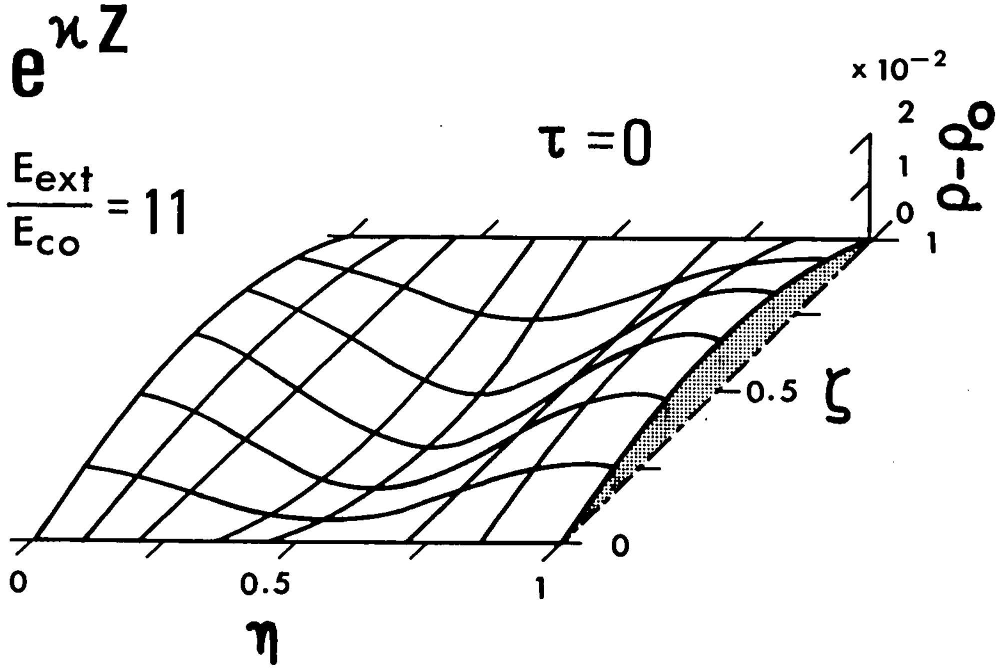

Fig. 3.15. Initial (τ=0), monochromatic perturbation of density in real space for Case 1. The perturbation has the amplitude of 1% of the background density and vanishes at both boundaries (ζ=0 and 1). The same form as this perturbation is used for other cases.

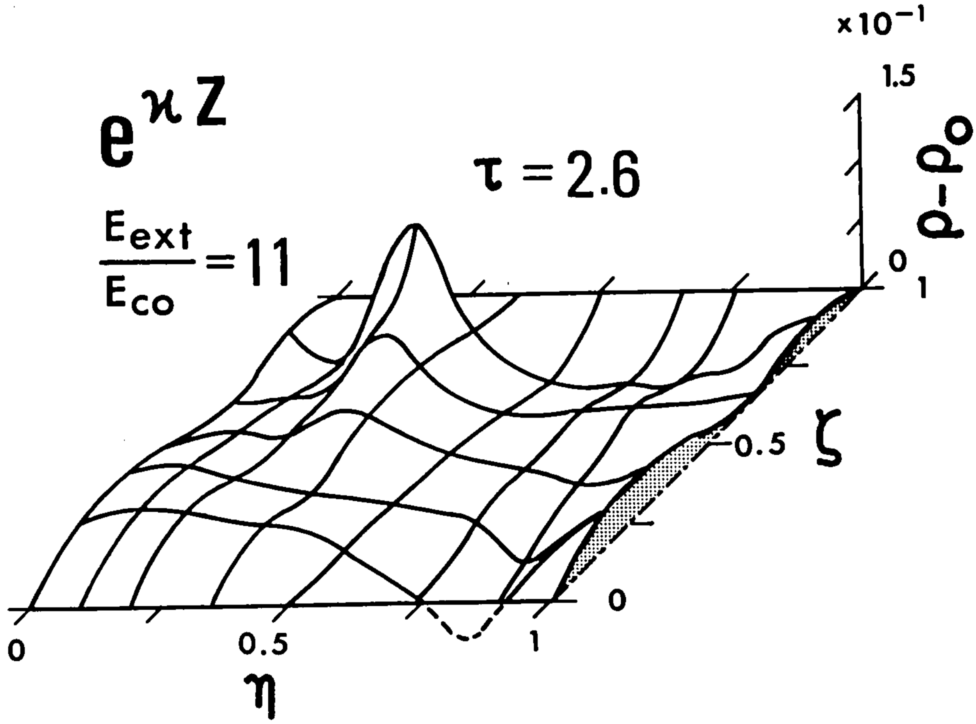

Fig. 3.16a. Density irregularities in real space at τ=2.6 for Case 1. Large irregularities are seen around both boundaries.

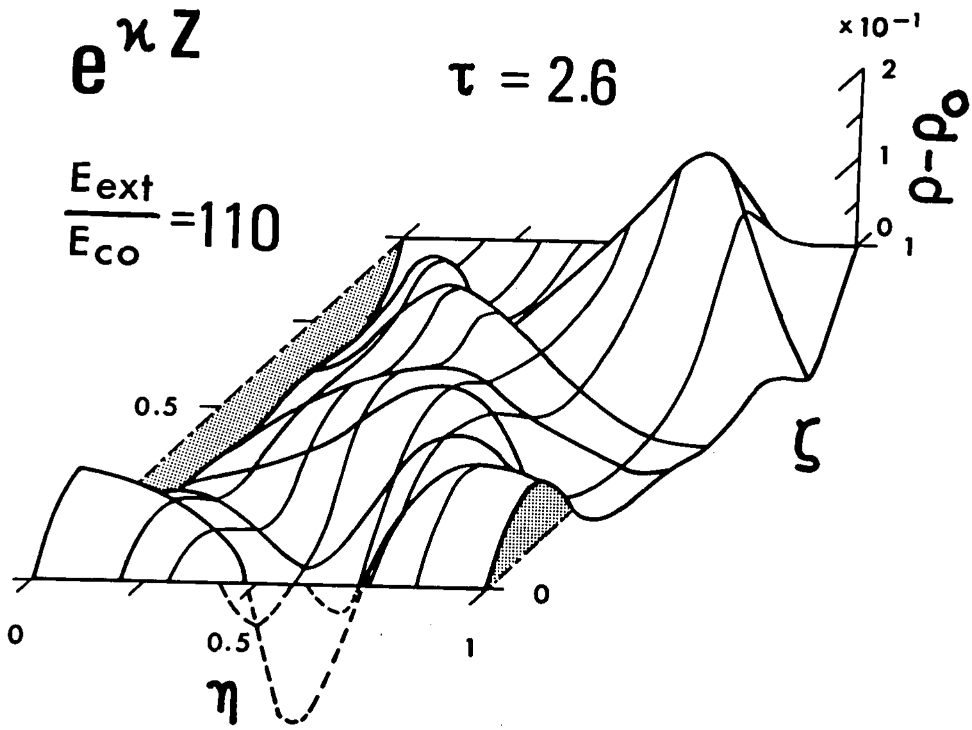

Fig. 3.16b. Density irregularities in real space at τ=2.6 for Case 2. Irregularities are seen all over the regions, being largest around both boundaries.

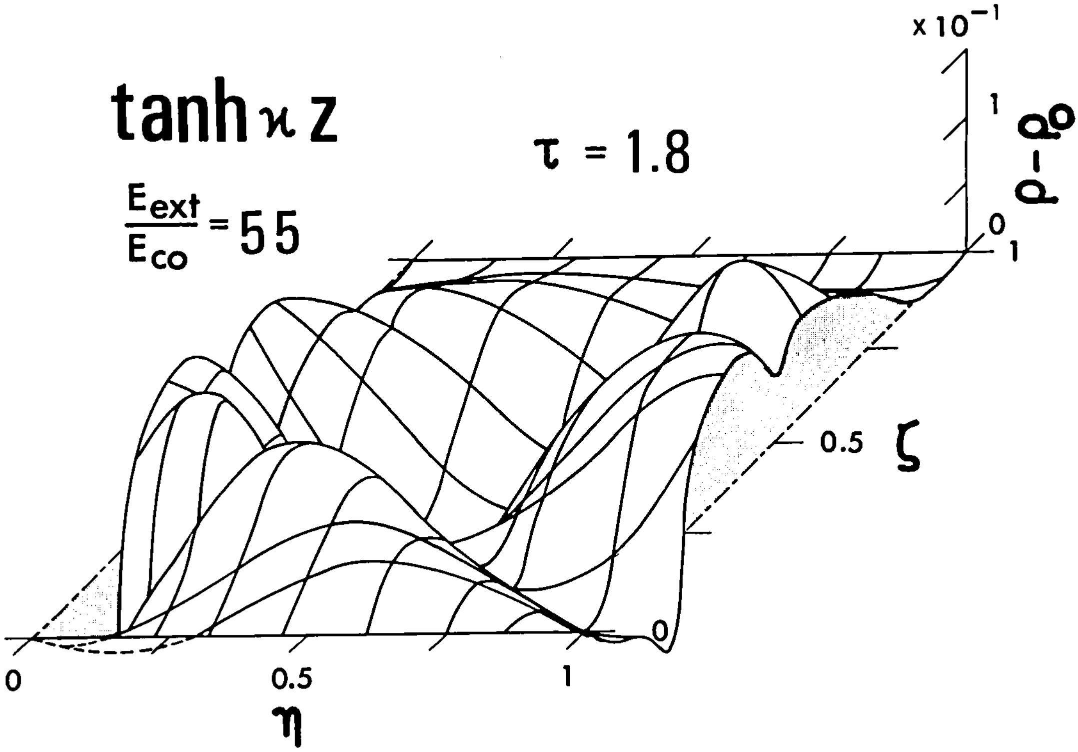

Fig. 3.16c. Density irregularities in real space at τ=1.8 for Case 4. Large irregularities are seen around the middle regions of ζ and vanish around both boundaries.

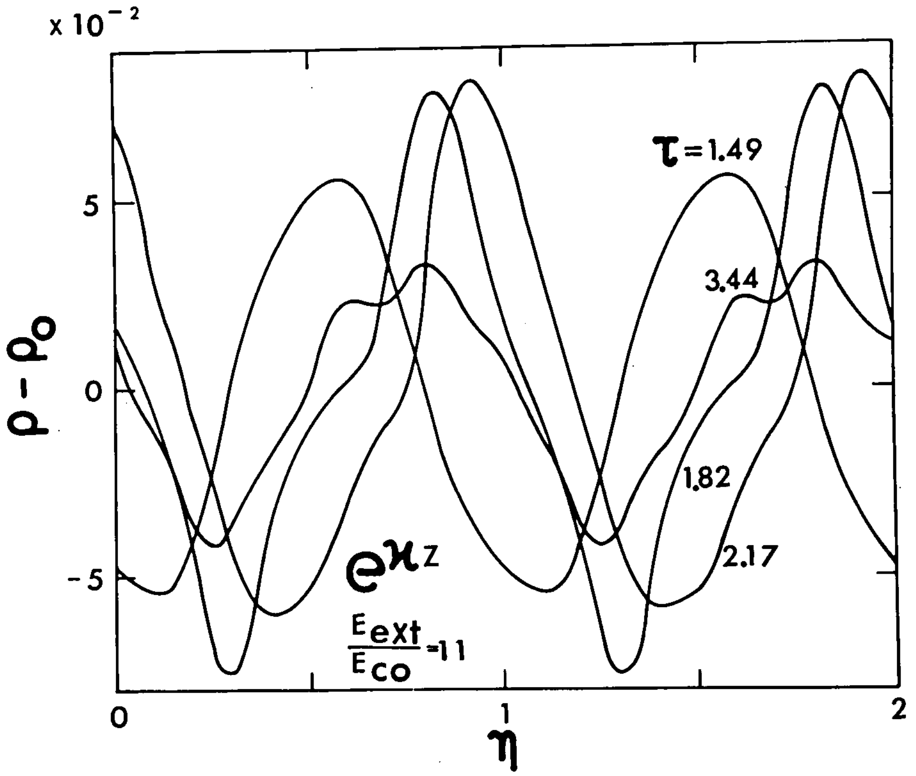

Fig. 3.17. Time evolution of the waveform of density in real space for Case 1. As times go on, the wave propagates to the right with its growing and subsequently decreasing amplitude, and suffers the deformation as shown in the figure.

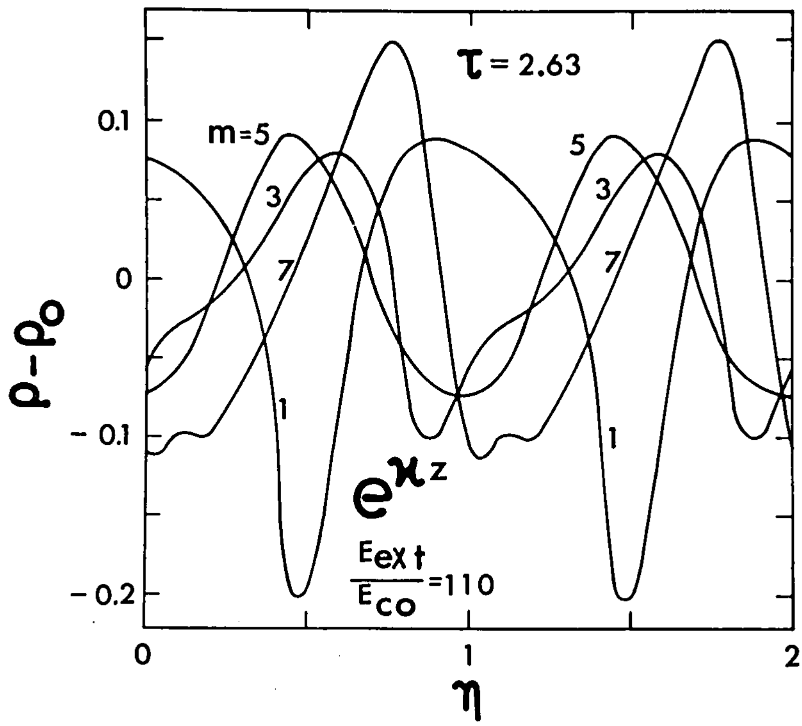

Fig. 3.18. Waveforms of density in real space at τ=2.63 for Case 2. The number labeled on each curve means the distance from ζ=0; m=1, 3, 5, and 7 correspond to ζ=1/8, 3/8, 5/8, and 7/8 respectively. Note that the waveforms of m=1 and m=3,7 are soliton- and sawtooth-like, respectively, while the waveform of m=5 seems to be monochromatic.

already shown the time evolution of ρ_0 in Fig. 3.11 to Fig. 3.14, hence $\rho(\eta,\zeta,\tau)$ - $\rho_0(\zeta,\tau)$ is shown in the figures.

Fig. 3.15 shows a monochromatic initial (τ= 0) perturbation of density with relative amplitude of 1 %, for Case 1. Same types of perturbation as Fig. 3.15 are imposed for other cases. General time evolution of perturbation is as follows. Initial perturbation moves approximately with the Hall speed along η-axis as its amplitude grows. After the nonlinear quenching of amplitude has been achieved, monochromatic shape is destroyed and an irregular form develops. With the passage of time, the amplitude of irregularities oscillates as is seen from the time evolution of the spectral density shown previously.

Fig. 3.16a illustrates the density irregularity at τ= 2.6, for Case 1. Amplitudes of the maximum and minimum are 10 % and -7 % respectively. We see that the irregularity is largely deformed from the monochromatic disturbance especially near the boundaries, but not so much in central regions of where the flattening of ρ_0 is formed. Another example of the density irregularity at τ = 2.6 for Case 2, where a very strong turbulence takes place, is shown in Fig. 3.16b. It is seen that the perturbation is highly irregular, the amplitude of which amounts to $\pm$ 20 % near the boundaries.

Fig. 3.16c shows the example of Case 4. Strong irregularity with the amplitude of $\pm$ 12 % is formed in central regions of ζ.

The details of density irregularity are shown in Figs. 3.17 and 3.18. For Case 1 (Fig. 3.17) we note that as time passes the waveform keeps moving to the right and is localized as the amplitude increases, and becomes broad and irregular as the amplitude decreases. Because E_{ext} is below E_{c1} for Case 1, the waveform is not deformed in so irregular fashion. When E_{ext} is beyond E_{c1}, however, this is not the case. Fig. 3.18 shows waveform of four different positions m = 1, 3, 5 and 7 at $\tau = 2.63$ for Case 2. As is seen, the waveforms of m = 1 and m = 3, 7 are soliton- and sawtooth-like, respectively, and that of m = 5 seems to be monochromatic.

IV. Discussion

Now, we compare the computed results with nonlinear theory of Sato(1971). The comparison is listed in Table 3.2 where τ_L and $\overline{\tau}_L$ indicate the linear growth time by the theory and by the computation, respectively. $|\tilde{\rho}_{k_m}|^s$ represents the theoretical quasilinear saturation amplitude of the mode with wavenumber k_m at which the linear growth rate is maximized. $|\overline{\tilde{\rho}}_{k_1}|^s$ is the computed saturation amplitude of

Table 3.2. Comparison of computed results with theory.

Case		1	2	3	4
Theory	τ_L	0.660	0.925	0.602	0.652
	$\lvert\tilde{\rho}_{k_m}\rvert^s$ (%)	7.1	12	7.1	10
Computed results	$\bar{\tau}_L$	0.646	0.844	0.608	0.648
	$\lvert\bar{\tilde{\rho}}_{k_1}\rvert^s$ (%)	6.1	7.8	5.0	7.0

the mode with wavenumber k_1 (i.e., the fundamental mode). The upper bar means the average quantity over z.

Table 3.2 indicates a good agreement of τ_L and $\overline{\tau}_L$. Some discrepancy between $|\widetilde{\rho}_{k_m}|^S$ and $|\rho_{k_1}|^S$ indicates that the mode coupling plays a role to some extent in stabilization. The discrepancy becomes large as E_{ext} increases. This is because the mode coupling becomes more important for larger E_{ext}.

Concerning the flattening of the density and potential profiles, our computation found that which quasilinear process dominates depends largely on boundary conditions. For an exponential type, i.e., Case 1 where the density gradient exists everywhere along the z direction, the instability is mainly shut off by a plateau formation in the density profile. For a hyperbolic tangent type, i.e., Cases 3 and 4 where the density gradient exists in the middle regions and vanishes at boundaries, the quenching is mainly due to the flattening of the potential profile at least at early stage of time and thereafter both effects become operative. We can infer from the result of the latter type that, if the boundary width ℓ goes to infinite while keeping the density gradient only in the middle regions, the quenching due to the flattening of the potential profile might be important for all the time (Sato and Tsuda, 1968; Tsuda et al., 1969). We remark that Hooper's experiment (1971) in a reflex arc and the quasilinear theory by Kim and Simon(1969) may correspond to Case 1, and that Cases 3 and 4 more or less represent the lower ionospheric condition.

Spectral appearances as shown in Fig. 3.3a, that is to say, $|\tilde{\rho}_2| > |\tilde{\rho}_1|$ around $\tau = 4.2$, and the initial growth and following decay of $|\tilde{\rho}_1|$, may explain the Hooper's experiment. When E_{ext} is far below E_{c1}, we can expect that spectral appearance becomes quite chaotic so that the main mode is not necessarily the leading mode. Ion cloud experiment in the lower ionospheric E layer by Davis(1971) serve a number of results to be compared with the nonlinear analysis. Though not satisfactorily, sporadic appearances of discrete spectrum i.e., cyclic growth and decay of discrete spectrum, are explained by the present analysis. We have shown some indication of the cyclic growth and decay of the instability (see Fig. 3.3).

Rocket observations of sporadic E layers (Smith, 1966; Oya, 1967) and of equatorial E layer (Prakash et al., 1970) seem to support the results of our model. From Fig. 3.16c we have an irregularity with characteristic length of a few hundred meters in both the y and z directions, and of the amplitude of 12 %.

V. Summary and Conclusion

We have shown computer analysis of the two-dimensional nonlinear cross-field instability. Important difference between the one- and two-dimensional models is that the nonlinear saturation of unstable waves is achieved only by the mode coupling in the former, but not only by the mode coupling but also by the quasilinear effect in the latter. The quasilinear process acts to deform background density and potential profiles, that is, to flatten the profiles, thereby shutting off the growth of the instability. We find that which flattening takes place depends on boundary condition. For the density distribution of an exponential type, the flattening of the density profile is more important than that of the potential profile. This is because the excess charges accumulated at boundaries (electrodes) are short-circuited by the external circuit. Our boundary condition imposed on the perturbation is just the case. On the other hand, for the density distribution of a hyperbolic tangent type, in which the density gradient vanishes near boundaries, we find that the flattening of the potential profile plays the leading part in stabilization. The reason is as follows. In this case there are no potential fluctuations to be short-circuited near boundaries, since the fluctuations are concentrated in central regions. We point out that the former and latter cases may correspond to the circumstances of laboratory experiment and to the ionospheric E layers, respectively. This is consistent with the inference of Sato and Tsuda(1968), Tsuda et al.(1969), and Sato(1971).

Another feature to be noted is the cyclic behavior of spectral density $|\tilde{\rho}_n|$. If E_{ext} is a little beyond E_{c0}, the amplitude of $|\tilde{\rho}_1|$ stays at a constant level after a saturation. However, when E_{ext} is increased more, the mode coupling process becomes to be operative to destroy the flattening of density and/or potential profiles. Hence the competition between the quasilinear and mode coupling processes reflects the cyclic growth and decay of $|\tilde{\rho}_n|$. If $E_{ext} \gg E_{c1}$, strong mode coupling process, which stabilize no more the system, predominates the quasilinear process to yield an explosive instability (Sato, 1971). This was confirmed by our computations, although we met a numerical instability, perhaps because of small mode number used.

In conclusion, we recommend that more detailed analysis of two-dimensional model will give better understanding of the behavior of ionospheric irregularities and of laboratory experiments.

Chapter 4

NEW MECHANISM OF AURORAL ARCS

I. Introduction

Auroral displays give us an important clue for study of dynamic couplings between the magnetosphere and the ionosphere. In spite of its simple destiny of visibility, the aurora is a complex, mixed-up, phenomenon associated with a number of dramatic processes, e.g., acceleration of charged particles, precipitation of the accelerated particles into the ionosphere and arc formation.

From the electrical viewpoint, the ionosphere is a current-carrying medium, whereas the magnetosphere usually behaves as a dielectric across the magnetic field lines and as almost a perfect conductor along them. The auroral particles make long excursions over such distant and electrically different media as the magnetosphere and the ionosphere. Such long excursions make it very difficult to solve the charged particle motions associated with auroras.

So far a number of concepts have been presented on the magnetosphere-ionosphere coupling; the so-called Birkeland current system and Alfvén layer may be the first and most basic ones. Schield et al.(1969) pointed out that the

Alfvén layer could be a source of field-aligned currents. Various auroral models have been presented by many authors (for example, Kern, 1962; Fejer, 1963; Boström, 1964, 1968). All these considerations help us to have a deeper understanding of charged particle dynamics.

In those models, however, the ionosphere is usually treated as a passive medium; the ionosphere merely acts as a huge passive screen upon which a magnetospheric picture is drawn, and the magnetosphere plays the leading role in most of the auroral dynamics. Recent rocket-borne and satellite experiment have revealed that the ionospheric current system in the auroral zone is connected with the magnetospheric electric current system via field-aligned currents (Cloutier et al., 1970; Armstrong and Zmuda, 1970; Vondrak et al., 1971; Park and Cloutier, 1971; Choy et al., 1971). This fact suggests that even the ionosphere could be an initiator of aurora formation, though not such a drastic one as the magnetosphere. The purpose of this paper is then to look for a mechanism in which the ionosphere plays an important part in aurora formation.

Among various features of auroral displays, our primary concern is the auroral arcs. It is well known that the aurora often exhibits a multiple character in its curtain-like forms. Akasofu et al.(1967) said that this multiple character would provide significant information on the production mechanism of auroral particles. In fact, Akasofu and Chapman(1961) and Coppi et al.(1966) considered that the multiplicity was a direct consequence of an acceleration mechanism in the magnetosphere; namely the mechanism itself has a multiple structure.

Recently, Atkinson(1970) proposed a different model; the multiple arcs result from nonlinear feedback oscillations of electric currents flowing up and down along the magnetic field lines, which are closed by the magnetospheric polarization current. This model is based on an idea that the auroral arcs caused by a cooperation between the magnetosphere and the ionosphere. However, a question about his treatment of cold electrons flowing up along the magnetic field lines has been raised by Sato and Ogawa(1972).

In this paper we investigate another possibility of multiple arc formation. Our model is constructed on the basis that the multiple character has its origin in the ionosphere, and their development is determined by the ionosphere-magnetosphere coupling.

Akasofu et al.(1966) report that the multiple arcs appear during rather quiet times of auroral activity and that they usually move toward the equator during those times. This fact suggests that the arc formation is a phenomenon pertinent to quiet auroral activity. Therefore, it is not necessarily self-evident that the multiplicity is a simple project of the structure of acceleration mechanism in the magnetosphere, as was considered by Akasofu and Chapman(1961) and Coppi et al. (1966). Rather, it seems likely that the multiplicity is a manifestation of some other process pertinent to quiet times. In this paper we propose a new mechanism of auroral arc formation; the ionospheric irregularities produced by some ionospheric plasma instability trigger a precipitation of auroral particles and result in multiple auroral arcs. In other words, the mechanism is constructed from the following two stages (two- stage theory); first, a macroscopic ionospheric irregularity (arc-to-be) is formed, and secondly, the arcs-to-be are intensified by particle precipitation triggered by some mechanism and result in well-developed arcs.

II. Description of Model

Our model consists of the following two stages:

1. We assume that, during pre-break-up periods, or recovery phase, of the substorm, an appreciable amount of charged particles precipitate rather uniformly into the ionosphere around the midnight. The static electric field directs to the south as a whole (see, for example, Haerendel, 1970). Under these circumstances, the background ionosphere is formed

in such a way that the electron concentration gradually increases towards the morning side (eastwards). Such configuration is subject to a kind of collisional drift-wave instability, the so-called cross-field instability (Tsuda et al., 1966). As a consequence of this instability, there arises a wavy structure in electron concentration as shown in Fig. 4.1.

2. A polarization electric field, E_p, arises across an enhanced part of the irregularity (arc-to-be) as shown in Fig. 4.1. The induced potential ϕ due to E_p drives a field-aligned electric sheet current, possibily terminated by the ionospheric Pedersen conductivity in the opposite hemisphere (Fig. 4.2). Since the electrons have much higher mobilities than the ions, we may consider that the current is carried mainly by the electrons. When the speed of electrons exceeds the critical speed, the ion waves are excited and the ambient electrons will probably be accelerated by some nonlinear wave-particle interactions (Buneman, 1959). Although one does not know the acceleration rate as yet, one may assume that kev electrons are effectively produced by such nonlinear interactions. If such kev electrons are not produced, the original ionospheric irregularity will probably be smoothed out, since the space charges that produce the polarization field E_p may quickly be cancelled by the short-circuit effect along the magnetic field lines. The kev electrons produced by the ion-wave instability however, can produce a great

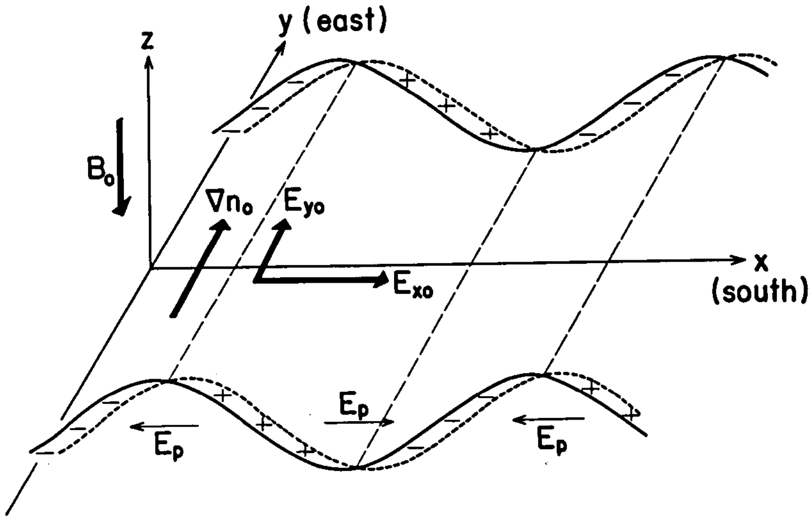

Fig. 4.1. Coordinates and configuration of the system.

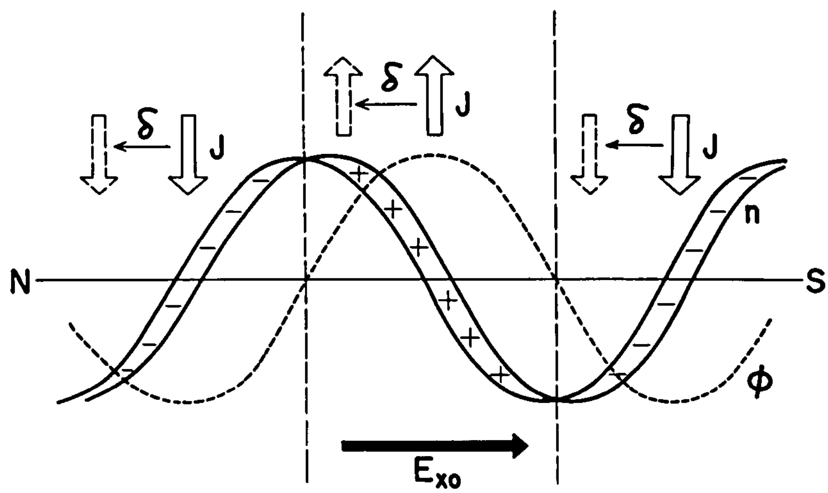

Fig. 4.2a. Schematic view showing the relation between the field-aligned currents j and the ionospheric irregularities of electron concentration n and induced potential ϕ. Note that the positions of the current sheets shift toward the north as the inductance along the magnetic lines of force or δ, increases.

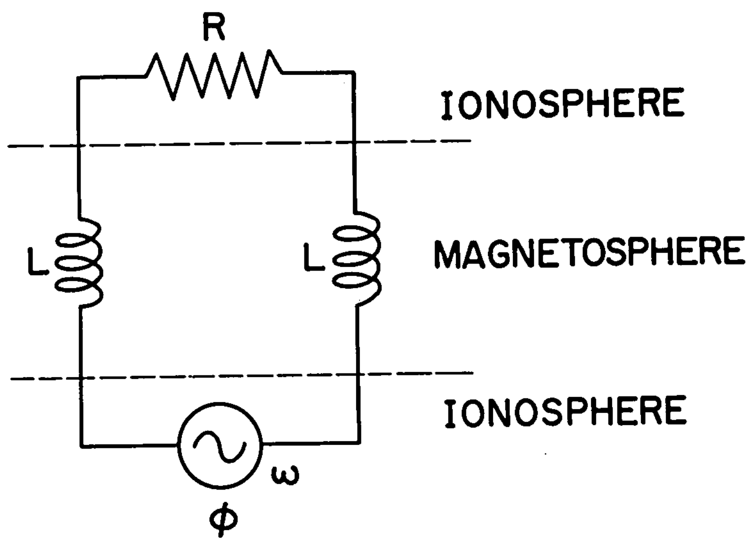

Fig. 4.2b. An equivalent electric circuit connecting the ionospheres of both hemispheres via the magnetosphere. When the ionospheric irregularity moves toward the equator, an alternating voltage arises between two fixed magnetic field lines.

number of ion-pairs down in the ionosphere. Accordingly, the electron concentration is enhanced at places upon which the kev electrons precipitate, namely, at the feet of the field lines along which the ion-wave instability takes place. This enhancement of electron concentration causes an additional polarization field due to the background southward electric field. If this additional field overcomes the short-circuit effect along the field lines, the original irregularity may be enhanced and develop into the auroral arcs.

If the impedance of the closed circuit is purely resistive, the precipitation place of kev electrons (peak of the potential) deviates by one-fourth wavelength from the peak density of the irregularity (see Fig. 4.2a). In this case an intensification of the original irregualrity may not be expected. In actual cases, however, the electrons experience a phase lag during their long excursions because of the inductance along their path, namely along the field lines. This inductance acts to make the precipitation coincident with the peak density of the irregularity. With an appropriate phase lag, therefore, the growth of the irregularity may be maximized, and the original irregularity is expected to develop into multiple auroral arcs. A quantitative discussion is given in the following section.

III. Theory

A. Coordinates and Equations

A right-hand coordinate system (x,y,z) is so chosen that the x, y and z axes in the south, east and upward directions, respectively. For simplicity, we take up the northern hemisphere, so that the geomagnetic field directs downwards (negative z axis).

The governing equations that describe the dynamics of charged particles in the E layer ionosphere (100 - 150 km heights), may well be described by

$$\frac{\partial n}{\partial t} + \nabla \cdot n\underset{\sim}{v}^{\pm} = q^{\pm} - \alpha n^2 , \qquad (4.1)$$

$$n\underset{\sim}{v}^{\pm} = \pm n\mu_{\parallel}^{\pm} (\underset{\sim}{E} + \underset{\sim}{v}^{\pm} \times \underset{\sim}{B}) - D_{\parallel}^{\pm}\nabla n , \qquad (4.2)$$

where the superscripts $\pm$ denote electrons (-) and ions (+); n is the electron concentration (equal to the ion concentration); q is the production rate of charged particles; α is the recombination coefficient; $\mu_{\parallel}$ and $D_{\parallel}$ denote, respectively, the mobility and the diffusion coefficient along the magnetic field lines; $\underset{\sim}{E}$ and $\underset{\sim}{B}$ are the electric and magnetic fields. The Eqs. (4.1) and (4.2) may be sufficient to describe the behavior of charged particles in the E layer ionosphere, since the time scale of interest is much longer than the collision times, the inverse of cyclotron frequencies and the inverse of plasma frequencies, of both the electrons and ions. Further, since the ionosphere is a low-β plasma the change of the magnetic field can be neglected; namely, the electrostatic approximation is valid.

B. Background Distribution

Recently, the techniques of electric field measurements have strikingly been developed and have disclosed that the static field in the ionosphere mainly directs southward in the northern auroral zone, typically 10 to 50 mV/m (see Haerendel, 1970). This southward electric field E_{x0} drives the precipitating particles toward the east, so that the ionization is expected to increase gradually toward the east.

Neglecting the diffusion terms and putting $q^+ = q^- \equiv q$, Eqs. (4.1) and (4.2) are approximately reduced to

$$\frac{\partial n}{\partial t} + v_{y0}\frac{\partial n}{\partial y} = q - \alpha n^2, \qquad (4.3)$$

where

$$v_{y0} = \frac{\mu_p^+\mu_H^- + \mu_p^-\mu_H^+}{\mu_p^+ + \mu_p^-} E_{x0} \sim \mu_H^- E_{x0} ,$$

with $\mu_p^{\pm} = \mu_{\parallel}^{\pm} / [1 + (\mu_{\parallel}^{\pm} B)^2]$ and $\mu_H^{\pm} = \mu_p^{\pm} (\mu_{\parallel}^{\pm} B)$. In deriving Eq. (4.3) we have assumed that the ionization in the precipitation zone distribute uniformly along the north-south direction, since the drift speed of the ionization along this direction may be smaller than v_{y0} ($E_{x0} \gg E_{y0}$). The steady solution of Eq. (4.3) is easily solved as

$$n_0(y) = N_1 \frac{A\exp(2\eta y) - 1}{A\exp(2\eta y) - 1}, \qquad (4.4)$$

where $N_1 = (q/\alpha)^{1/2}$, $\eta = \alpha N_1/v_{y0}$ and $A = (N_1 + N_0)/(N_1 - N_0)$, N_0 being the elctron concentration at the western edge of the precipitation zone, namely, at $y = 0$. For example, we choose the ionospheric parameters during rather quiet times of auroral activity such that

$$N_0 = 10^9\ \mathrm{m}^{-3}, \qquad \alpha = 10^{-13}\ \mathrm{m}^3\mathrm{sec}^{-1},$$

$$q = 10^7\ \mathrm{m}^{-3}\mathrm{sec}^{-1}, \qquad v_{y0} = 200\ \mathrm{msec}^{-1}.$$

Thus we have

$$N_1 = 10^{10}\ \mathrm{m}^{-3} \gg N_0 \quad \text{and} \quad \eta = 5 \times 10^{-6}\ \mathrm{m}^{-1}.$$

Eq. (4.4) is then approximated by

$$n_0(y) \sim N_1 \tanh(\eta y). \qquad (4.5)$$

From Eq. (4.5) it is seen that the ionization monotonically increases towards the east from N_0 up to N_1 and that the scale length (e-folding distance) is approximately $\eta^{-1} \sim$ 200 km for the present case.

Next, we shall show that the above configuration is subject to the cross-field instability, resulting in a large scale irregularity of electron concentration (arc-to-be) whose fronts are roughly parallel to the east-west direction.

C. Irregularity Formation (1st srage)

We put the layer width of the ionosphere under consideration as h, 50 km, say, and discuss the problem with the quantities averaged over this layer. This is equivalent to regarding the ionosphere as a horizontal plane.

Combining Eqs. (4.1) and (4.2), we obtain

$$\frac{\partial n}{\partial t} - \mu_H^{\pm}\left[\frac{\partial}{\partial x}(nE_y) - \frac{\partial}{\partial y}(nE_x)\right] \pm \mu_p^{\pm}\left[\frac{\partial}{\partial x}(nE_x) + \frac{\partial}{\partial y}(nE_y)\right]$$

$$- D_\perp^{\pm}\left(\frac{\partial^2 n}{\partial x^2} + \frac{\partial^2 n}{\partial y^2}\right) = q - \alpha n^2 - \frac{D_\parallel^{amb}}{h^2}[n - n_0(y)], \qquad (4.6)$$

where the last term on the right represents an equivalent diffusion loss along the magnetic field lines (across the ionosphere plane); $D_\perp^\pm = D_\parallel^\pm / [1 + (\mu_\parallel^\pm B)^2]$.

Linear analysis of Eq. (4.6) gives the growth rate as (see Appendix)

$$\Gamma \simeq \frac{\xi \tilde{k}^2[(\beta - \tan\theta)E_{x0} + (1 + \beta\tan\theta)E_{y0}]}{\tilde{k}^2(1 + \tan^2\theta) + (1 - \beta\tan\theta)^2}$$

$$- \tilde{k}^2 \frac{\kappa^2 D_\perp^{amb}}{\beta^2} - \frac{D_\parallel^{amb}}{h^2} - 2\alpha n_0 , \qquad (4.7)$$

where $\beta = M_p/M_H$ (= Pedersen/Hall conductivity) with $M_p = \mu_p^+ + \mu_p^-$ and $M_H = \mu_H^- - \mu_H^+$; $\xi = \kappa M_H M/M_p^2$; $M = \mu_p^+ \mu_H^- + \mu_p^- \mu_H^+$; $D_\perp^{amb} = (\mu_p^+ D_\perp^- + \mu_p^- D_\perp^+)/M_p$ and $D_\parallel^{amb} = (\mu_\parallel^+ D_\parallel^- + \mu_\parallel^- D_\parallel^+)/(\mu_\parallel^+ + \mu_\parallel^-)$; $\tilde{k}$ is the normalized wavenumber defined by $\tilde{k}^2 = k^2 \beta^2/\kappa^2$, $\kappa = d(\ln n_0)/dy \sim \eta$ and k being the wave-number; θ is the angle between the x axis and the wave vector $\underset{\sim}{k}$, measured toward the y axis. In Eq. (4.7) we may neglect the term of E_{y0} since $|E_{y0}| \ll |E_{x0}|$. Then we have

$$\Gamma \simeq \tilde{k}^2 \left[\frac{\xi(\beta - \tan\theta)E_{x0}}{\tilde{k}^2(1 + \tan^2\theta) + (1 - \beta\tan\theta)^2} - \frac{\kappa^2 D_\perp^{amb}}{\beta^2} \right]$$

$$- \frac{D_\parallel^{amb}}{h^2} - 2\alpha n_0 . \qquad (4.8)$$

From Eq. (4.8) it is seen that, when $\tilde{k}^2$ is fixed, the growth rate Γ is maximized at

$$\tan\theta = \beta - [1 + \beta^2 + \frac{1 - 3\,\beta^2}{\beta^2 + \tilde{k}^2}]^{1/2} \equiv \tan\theta_m . \qquad (4.9)$$

When, on the other hand, the angle θ is fixed, Γ is maximized at

$$\tilde{k}^2 = \cos^2\theta\{[(\beta - \tan\theta)(1 - \beta\tan\theta)^2\frac{E_{x0}}{E_{c0}}]^{1/2}$$

$$- (1 - \beta\tan\theta)^2\} \equiv k_m^2 , \qquad (4.10)$$

where $E_{c0} = M_H \kappa D_{\perp}^{amb}/M$. For example, we put the parameters as follows:

M_H	$\sim$	10^4	$m^2V^{-1}sec^{-1}$
M_p	$\sim$	5×10^3	$m^2V^{-1}sec^{-1}$
M	$\sim$	10^8	$(m^2V^{-1}sec^{-1})^2$
$D_{\parallel}^{amb}$	$\sim$	2×10^2	m^2sec^{-1}
$D_{\perp}^{amb}$	$\sim$	5	m^2sec^{-1}
α	$\sim$	10^{-13}	m^3sec^{-1}
κ^{-1}	$\sim$	200 $(\sim\eta^{-1})$	km
E_{x0}	$\sim$	10^{-2}	Vm^{-1}
n_0	$\sim$	5×10^9	m^{-3}.

Then we have

$$\beta = 0.5, \quad \xi = 0.2 \quad \text{and} \quad E_{c0} \sim 2.5 \times 10^{-9}\ \mathrm{Vm}^{-1}.$$

Thus Eq. (4.10) is approximated by

$$\tilde{k}_m^2 \sim \cos^2\theta_m [(\beta - \tan\theta_m)(1 - \beta\tan\theta_m)^2 \frac{E_{x0}}{E_{c0}}]^{1/2} >> 1. \quad (4.11)$$

Since $\tilde{k}_m^2 \gg \beta^2$, Eq. (4.9) is reduced to

$$\tan\ \theta_m \simeq \beta - (1 + \beta^2)^{1/2} < -1, \qquad (4.12)$$

i.e.,

$$-45^0 < \theta_m < 0^0.$$

For the present parameters, we have $\theta_m \sim -30^0$. From Eq. (4.11) the wavelength λ_m for maximum growth rate is estimated to be about 20 km. By using above approximations and assuming $\beta \lesssim 1$, the maximum growth rate Γ_m, is approximately given by

$$\Gamma_m \sim \xi E_{x0} - \frac{D_{\parallel}^{amb}}{h^2} - 2\alpha n_0. \qquad (4.13)$$

We see from Eq. (4.13) that the instability can arise when the electric field E_{x0} exceeds a certain critical value.

For the present parameters we have $\Gamma_m \sim 10^{-3}$ sec^{-1}. Of course we can obtain different values of θ_m, λ_m and Γ_m by choosing other set of parameters. If we put $\beta \sim 1$, then we have

$$\theta_m \sim -23^0, \quad \lambda_m \sim 30 \text{ km} \quad \text{and} \quad \Gamma_m \sim 10^{-3} \text{ sec}^{-1}.$$

From the above discussions, it may be said that the cross-field instability can produce the ionospheric irregularity whose spatial dimension is coincident with the spacing of auroral arcs and whose fronts are roughly parallel to the east-west direction but tilt somewhat in a northwest direction.

It is to be noted that nonlinear studies have shown the amplitude of unstable waves can reach to, say, 50 % of the background concentration (Sato and Tsuda, 1967; Tsuda et al., 1969; Sato, 1971).

D. Formulation of Arc Formation (2nd stage)

In this section, we formulate the process by which the irregularity caused by the plasma instability develops into the auroral arcs. For simplicity, we will here concern ourselves with one-dimensional case; the wave front of the irregularities are parallel to y axis.

As stated in Section II, we assume that the electrons come into and go out of the ionosphere in proportion to the potential ϕ arising in the irregularity.

The continuity equations are then given by

$$\frac{\partial n}{\partial t} + \frac{\partial}{\partial x}(nv_x^-) = S_d(\gamma_d + 1)\phi(x) - \alpha(n^2 - n_0^2) \quad \text{for } \phi \geq 0,$$

$$\frac{\partial n}{\partial t} + \frac{\partial}{\partial x}(nv_x^-) = S_u(1 - \gamma_u)\phi(x) - \alpha(n^2 - n_0^2) \quad \text{for } \phi \leq 0, \tag{4.14}$$

and

$$\frac{\partial n}{\partial t} + \frac{\partial}{\partial x}(nv_x^+) = S_d\gamma_d\phi(x) - \alpha(n^2 - n_0^2) \quad \text{for } \phi \geq 0,$$

$$\frac{\partial n}{\partial t} + \frac{\partial}{\partial x}(nv_x^+) = -S_u\gamma_u\phi(x) - \alpha(n^2 - n_0^2) \quad \text{for } \phi \leq 0, \tag{4.15}$$

where $S_d|\phi|$ and $S_u|\phi|$ ($S_d > 0$, $S_u > 0$) represent the rates of coming-down and going-up electrons proportional to the potential of the irregualrity; γ_d and γ_u are the ion-pair creation rates of the kev electrons associated with the coming-down and going-up electron flows.

The flow equations may be given by

$$v_x^- = -\mu_p^-[E_{x0} - \frac{\partial\phi(x)}{\partial x}] - \mu_H^- E_{y0},$$

$$v_x^+ = \mu_p^+[E_{x0} - \frac{\partial\phi(x)}{\partial x}] - \mu_H^+ E_{y0}. \tag{4.16}$$

Eqs. (4.14) and (4.15) are rewritten as

$$\frac{\partial n}{\partial t} + \frac{\partial}{\partial x}(nv_x^-) = \begin{cases} S_d(\gamma_d + 1)\phi(x) - \alpha(n^2 - n_0^2) & \text{for } \phi \geq 0, \\ S_u(1 - \gamma_u)\phi(x) - \alpha(n^2 - n_0^2) & \text{for } \phi \leq 0, \end{cases} \tag{4.17}$$

and

$$\frac{\partial I_x}{\partial x} = \begin{cases} -eS_d\phi(x) & \text{for } \phi \geq 0, \\ -eS_u\phi(x) & \text{for } \phi \leq 0, \end{cases} \tag{4.18}$$

where $I_x = en(v_x^+ - v_x^-)$. To exclude the charge accumulation, we add the following neutrality condition:

$$S_d\int_{\phi>0}\phi(x)\,dx + S_u\int_{\phi<0}\phi(x)\,dx = 0 .$$

Since

$$\int_{\phi>0}\phi(x)\,dx + \int_{\phi<0}\phi(x)\,dx = 0,$$

we have $S_d = S_u \equiv S_e$.

When we take into account the phase relation between the potential $\phi(x)$ and the sheet current, we must replace $\phi(x)$ by $\phi(x+\delta)$, where δ represents the phase lag. Thus, Eqs.

(4.17) and (4.18) are again rewritten as

$$\frac{\partial n}{\partial t} + \frac{\partial}{\partial x}(n\bar{v}_x) = \begin{cases} S_e(\gamma_d + 1)\phi(x+\delta) - \alpha(n^2 - n_0^2) & \text{for } \phi \geq 0\,, \\ S_e(1 - \gamma_u)\phi(x+\delta) - \alpha(n^2 - n_0^2) & \text{for } \phi \leq 0\,, \end{cases} \tag{4.19}$$

and

$$\frac{\partial I_x}{\partial x} = -eS_e\phi(x+\delta)\,. \tag{4.20}$$

Eqs. (4.16), (4.19) and (4.20) give a set of governing equations.

Since we are concerned with the behavior of auroral arcs during rather quiet times, we may consider that the magnetic field lines are closed and hence connected with the ionosphere in the other hemisphere. Therefore, the equivalent circuit may be given by Fig. 4.2b. The resistance R in the ionosphere may be given by (see Fig. 4.3)

$$R \sim \frac{1}{neM_p} \times \frac{d}{h\ell}\,, \tag{4.21}$$

where ℓ is the arc length (dimension of an arc in the east-west direction) and d is an average distance between the neighboring upward and downward current sheets, or the width of a current sheet in the north-south direction, which is approximately a half of the wavelength λ_m. The total sheet current J is roughly given by

$$J \sim eS_e \phi h \ell d. \tag{4.22}$$

From the relation $\phi \sim RJ$ and Eqs. (4.21) and (4.22), we have

$$S_e \sim \frac{nM_p}{d^2} . \tag{4.23}$$

The phase lag δ normalized by the wavelength λ_m(=2d) may be given by

$$\delta \sim \tan^{-1}\frac{\omega L}{R} , \tag{4.24}$$

where L is the inductance of the sheet and ω is the frequency of the alternating voltage $\phi(x)$ between two neighboring current sheets, which is equivalent to the characteristic frequency of the irregularity with wavelength λ_m, namely, $\omega = 2\pi V/\lambda_m$, V being the velocity of the irregularity toward the south (equator), which may be driven by the (small) westward electric field E_{y0}.

When we put d = 15 km, h = 50 km, ℓ = 500 km, V = 20 m/sec (E_{y0} = -2 mV/m) and L = 50 H, we obtain from Eqs. (4.21), (4.23) and (4.24) as

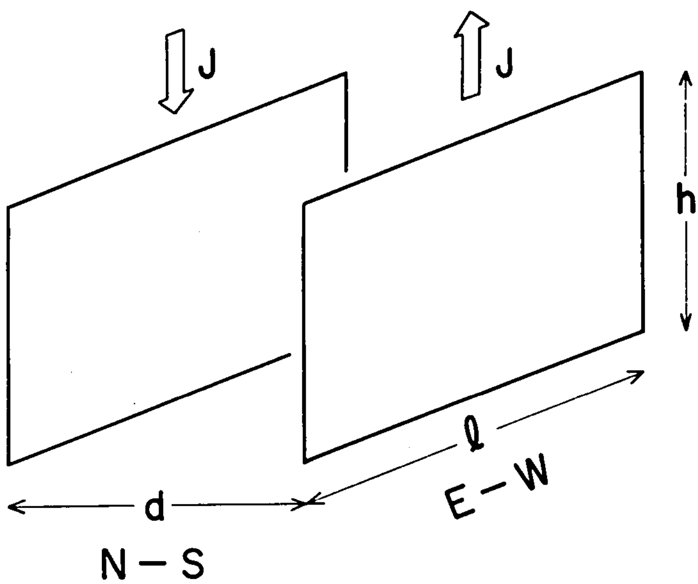

Fig. 4.3. Scales of the width, length and height of an arc-to-be.

$$R \sim 0.4 \text{ ohm}, \quad S_e \sim 10^5 \quad \text{and } \delta \sim \pi/4.$$

The value of the inductance L naturally depends on the configuration of an arc. Boström (1968) estimated the value for two models. According to his estimation, we may regard the value of L as roughly 100H. Akasofu et al.(1966) report that the typical spacing between neighboring arcs is 30 - 40 km, so that λ_m = 30 km, hence d = 15 km, is also reasonable.

In the following section we solve numerically a set of Eqs. (4.16), (4.19) and (4.20) as an initial-value problem and demonstrate whether or not a well-developed arc results from an ionospheric irregularity.

IV. Numerical Results

In subsections III(B) and (C) we have shown that the auroral zone ionosphere is susceptible to the cross-field instability. Since the evolution of this instability has already been studied in detail elsewhere (for example, Sato, 1971; see also Chapters 2 and 3 of theis thesis), we begin our calculation with an initial state that a periodic irregularity of electron concentration has already arisen in the ionosphere.

In order to see the essence of our model, we may reasonably put that $E_{y0} \simeq 0$. Further, we put that $\gamma_u = 0$. The validity of the assumption of $\gamma_u = 0$ is discussed in Sec. VI. After such simplification, the governing equations, i.e., Eqs. (4.16), (4.19) and (4.20), are characterized by the following parameters; E_{x0}, S_e, γ, δ, ε and $\mu \frac{+}{p}$, where $\gamma = \gamma_d$ and ε (%) denotes the initial amplitude of the irregularity relative to the background concentration.

Calculations are performed for 15 sets of parameters which are tabilated in Table 4.1. Typical examples that lead to a growth and damping of the initial irregularity are shown in Figs. 4.4 and 4.5. From these figures it is seen that the irregularity can either be intensified or suppressed depending on the values of parameters. In Figs. 4.6a and 4.6b an evolution of the peak density of the irregularity is drawn for 14 examples of Table 4.1. The movement of its peak position is also shown in Fig. 4.7. These figures give us a deeper understanding of how the development of the irregularity is related to the values of parameters. In order to visualize more clearly the evolution of the irregularities, several examples, other than Figs. 4.4 and 4.5, are given in Figs. 4.8

Table 4.1. Parameters of Computation

No.	(Figure)	E_{x0} (mV/m)	S_e	γ	δ ($\times\pi/5$)	ε (%)	V_f* (m/sec)	Result
1		10	10^4	10^2	0	5		Decaying
2	Fig.4.5	10	10^4	10^2	1	5		Decaying
3		10	10^4	10^2	2	5		Decaying
4		10	10^5	10	1	5		Decaying
		10	10^5	10^2	0	5		**
5	Fig.4.4	10	10^5	10^2	1	5	24	Growing
6	Fig.4.8	10	10^5	10^2	1	20	24	Growing
7	Fig.4.9	10	10^5	10^2	2	5	7	Growing
8		10	10^5	10^3	1	5	53	Growing
9		10	10^5	10^3	2	5	7	Growing
10		50	10^4	10^2	0	5		**
11	Fig.4.10	50	10^5	10^2	0	5		***
12	Fig.4.11	50	10^5	10^2	1	5	40	Growing
13		50	10^5	10^2	1	20	40	Growing
14†	Fig.4.12	10	10^5	10^2	1	5	24	Growing

Other parameters are chosen as follows (in MKS units):

$E_{y0} = -10^{-4}$ V/m, $\mu_p^- = 35$, $\mu_p^+ = 800$, $\mu_H^- = 2\times10^4$, $\mu_H^+ = 36$.

† In this case the ion mobilities are chosen as

$\mu_p^+ = 5\times10^3$, $\mu_H^+ = 800$.

* V_f means the final (steady-state) speed of an arc.

** The perturbation neither grows nor decays. The waveform is complex.

*** The perturbation grows but the waveform is complex.

The initial perturbation is taken in the form, $\varepsilon n_0 \sin^{16}(\ x/L)$, where L is chosen 30 km.

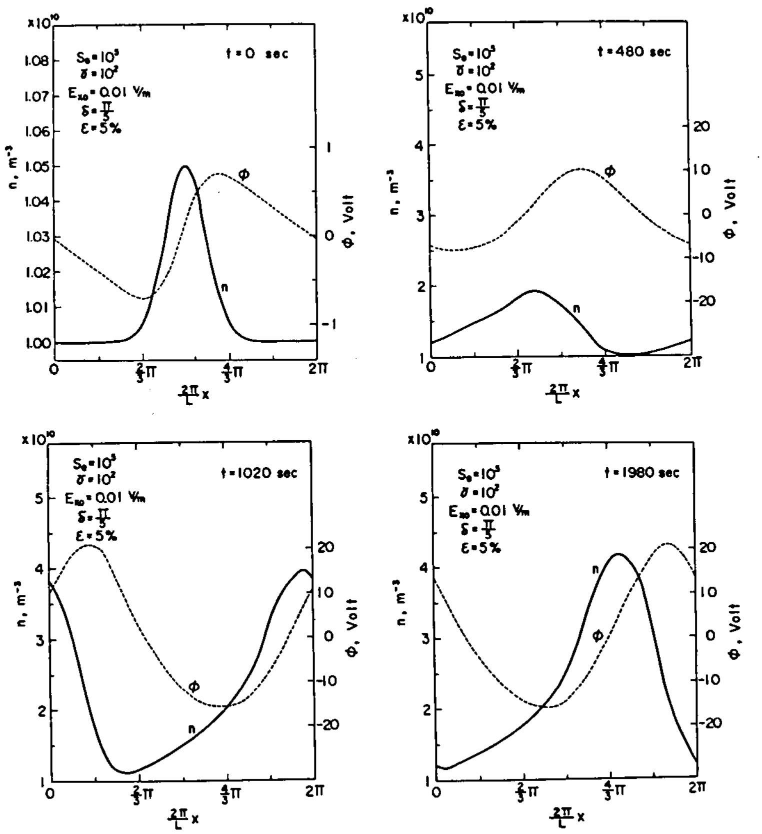

Fig. 4.4. Example of a growing irregularity: Spatial distributions of the irregularity concentration n and potential ϕ at four different times. The values of parameters for calculation are given in the row of No.5 in Table 4.1. The label L in the figure denotes the characteristic spacing of the irregularity ($\sim\lambda_m$): In computation we choose L= 30 km (the same value was used for other computations, Figs. 4.5 - 4.12).

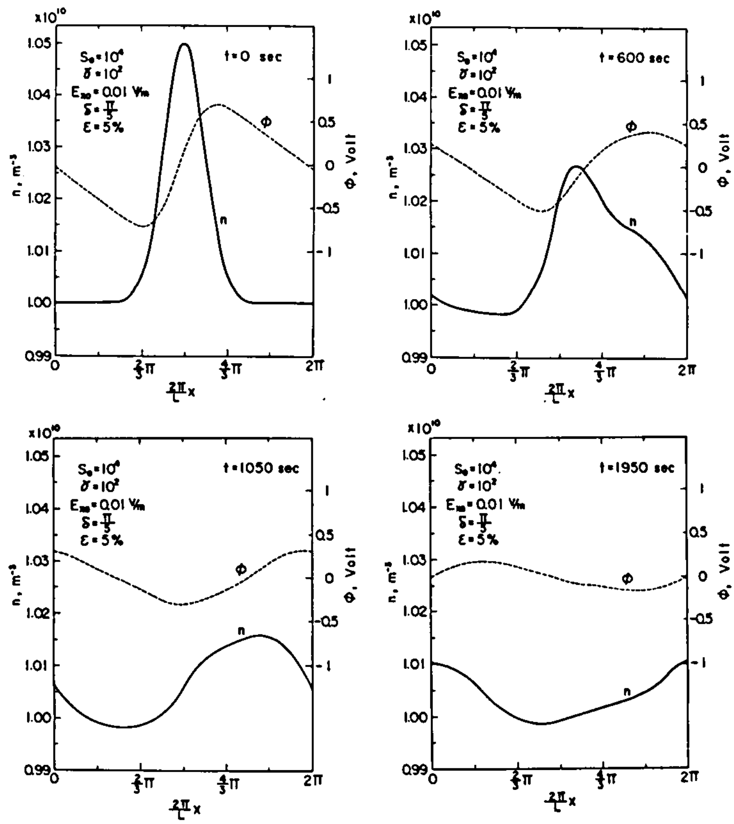

Fig. 4.5. Example of a decaying irregularity: Spatial distributions of the irregularity concentration n and potential ϕ at four different times. The values of parameters used for calculation are given in the row of No.2 in Table 4.1.

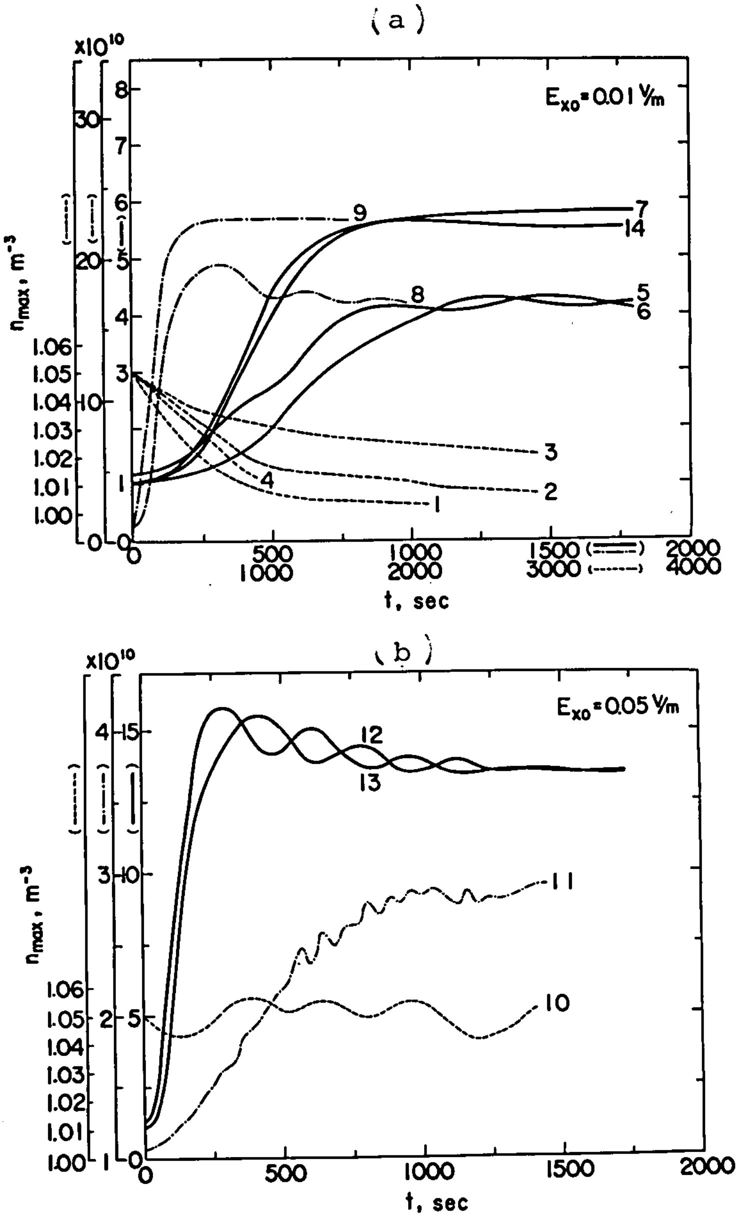

Fig. 4.6. Development of the peak concentration of an irregularity. The number on each curve corresponds to the case with the number given in Table 4.1: (a) Cases of E_{x0}= 0.01 V/m, and (b) cases of E_{x0} = 0.05 V/m. Note that there exists a steady solution.

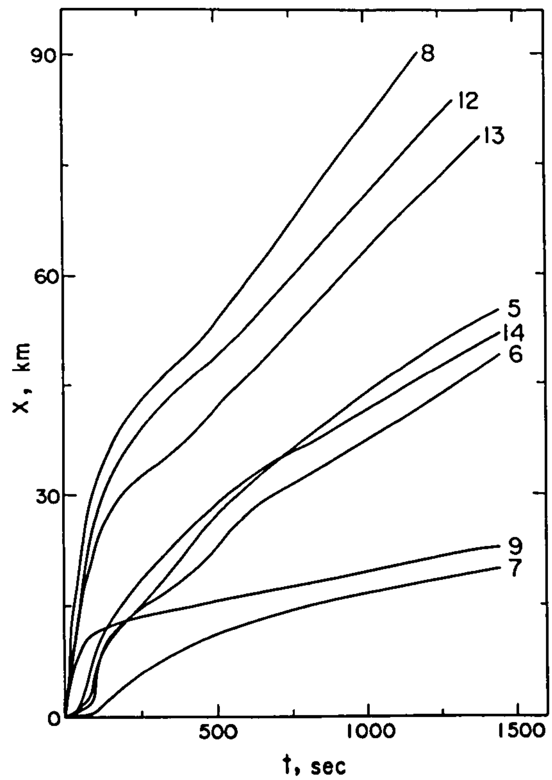

Fig. 4.7. Movement of the peak position of an irregularity. The number on each curve corresponds to the case with the number given in Table 4.1. Note that the irregularity moves toward the equator with a rather high speed during the early stage of its development but with a slower (constant) speed after its amplitude saturates.

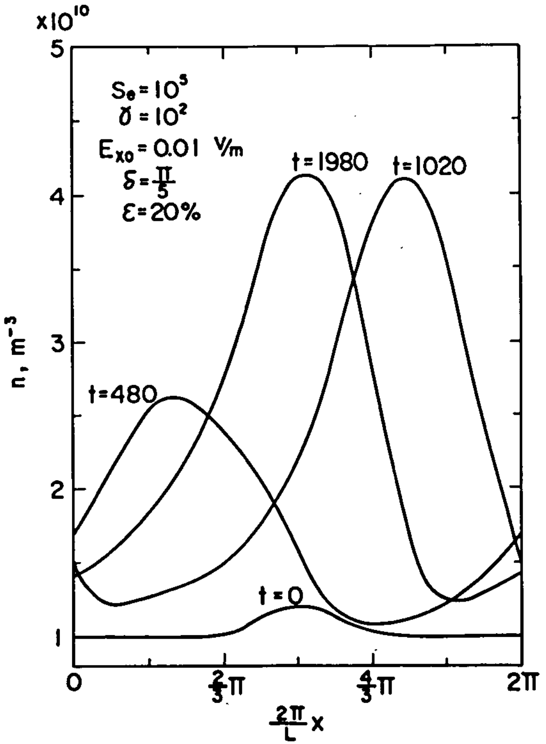

Fig. 4.8. Development of an arc for the case of No. 6 in Table 4.1. Compare with Fig. 4.4 in which ε = 5 %.

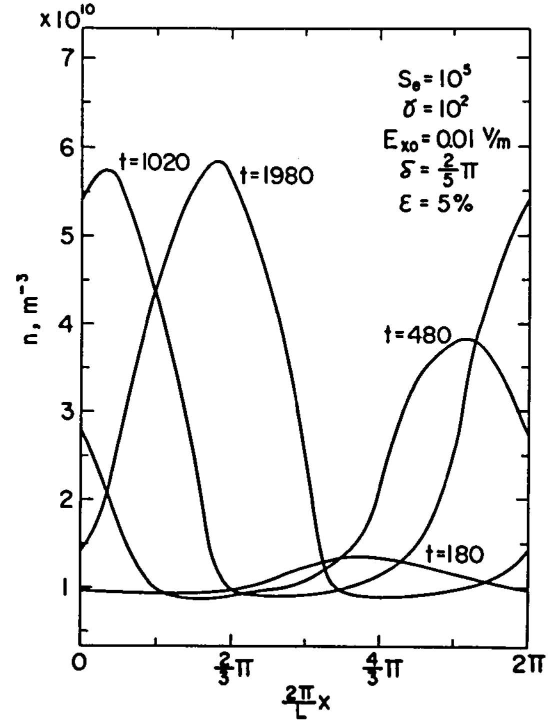

Fig. 4.9. Development of an arc for the case of No.7 in Table 4.1. Compare with Fig.4.4 in which δ= π/5.

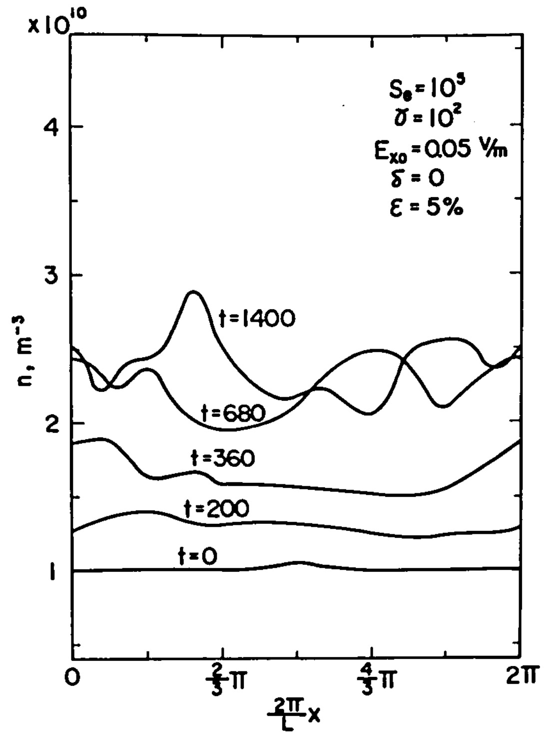

Fig. 4.10. Development of an arc for the case of No.11 in Table 4.1. Note that the electron concentration n increases rather uniformly with time when $\delta = 0$, but a small peak appears.

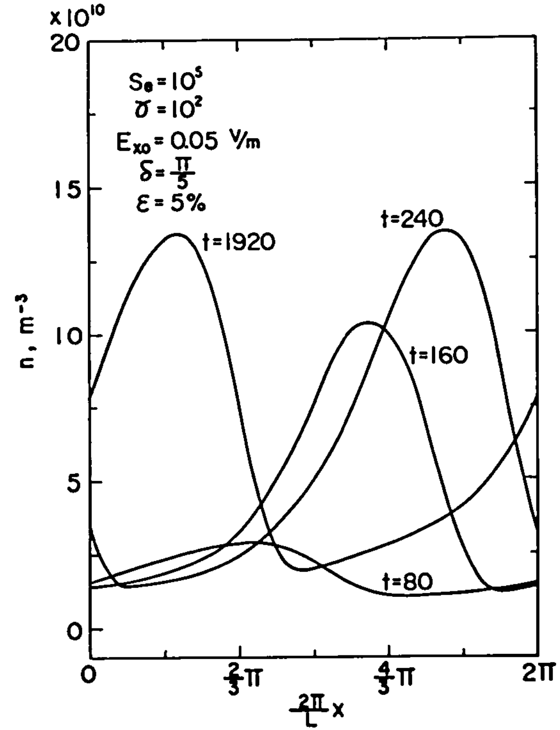

Fig. 4.11. Development of an arc for the case of No.12 in Table 4.1. Compare with Fig. 4.4 in which $E_{x0} = 0.01$ V/m.

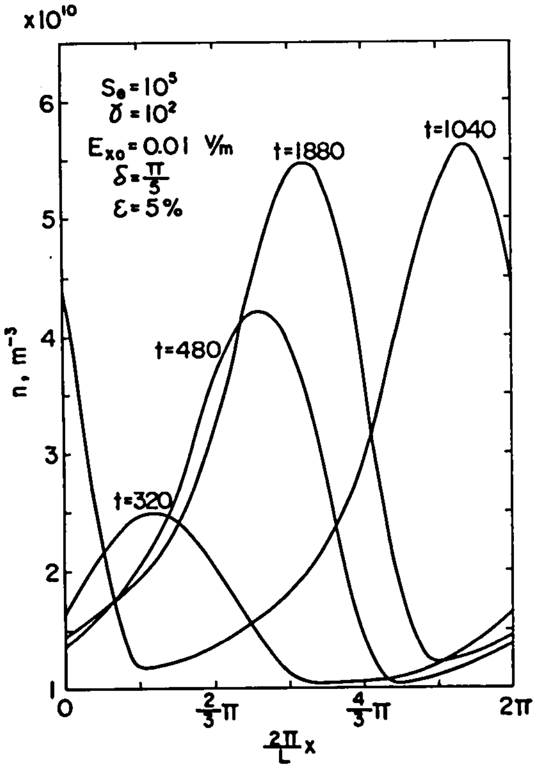

Fig. 4.12. Development of an arc for the case of No.14 in Table 4.1. Note that the irregularity can grow more largely as the Pedersen conductivity, or M_p, increases (compare with Fig. 4.4).

- 4.12.

We summarize the characteristics involved in the figures in the following way:

1. The ionospheric irregularities, which may be caused by the cross-field instability, or, possibly, by some other process, can result in arc-like forms by the present mechanism.

2. Generally speaking, the larger the values of S_e, γ, δ and E_{x0}, the more strongly the irregularities develop.

3. The role of the inductance along the magnetic field lines plays an important part in arc formation. For arc formation, the reactance due to the magnetospheric inductance must be as large at least as the ionospheric Pedersen resistance.

4. The initial amplitude ε little affects the final form as can be seen by comparing the curves 5, 12 with the curves 6, 13 in Fig. 4.6, and Fig. 4.4 with Fig. 4.8.

5. As can be seem from Fig. 4.7, the steady arcs move toward the equator with constant speeds, roughly 7 - 50 m/sec for present parameters. In their developing phases, their speeds are much faster; they reach up to 300 m/sec. They are largely controlled by δ, E_{x0}, S_e and γ.

6. When the phase lag δ is relatively small, there appear oscillatory behaviors in amplitude; compare the curves 5, 6, 8, 12 and 13 with $\delta = \pi/5$ with those 7, 9 with $\delta = 2\pi/5$. The periods of the amplitude oscillations are roughly 500 -

1000 sec for the present cases.

7. By comparing the curve 5 with the curve 14, it is seen that for larger μ_p^+, hence M_p, the arcs become larger. This may be due to the fact that the larger value of M_p, the larger the induced potential. Thus the effect of increasing M_p may be equivalent to that of increasing the external field E_{x0}. The value of M_p in the auroral zone seems much larger than those used for calculations of No.1 - No.13 in Table 4.1. Therefore, it seems that in actual cases an arc is much more likely to take place. The example of No.14 may well fit the real case.

V. Deformation of Arcs

We shall now discuss the stability of well-developed auroral arcs. By looking at the configuration of the arcs, we immediately notice a possibility that arcs suffer from the cross-field instability (Hooper and Walker, 1971).

Let us consider the case in which the arcs are homogeneous and parallel to the east-west direction. By changing the coordinates in such a way that the positive x and y axes are in the west and south directions, it is known that the Eq. (4.7) can be used as it stands for discussing the instability criterion. Since the electric field mainly directs to the south, i.e., $|E_{x0}| \ll |E_{y0}|$ in the present coordinates, Eq. (4.7) is approximated by

$$\Gamma \simeq \tilde{k}^2 [\frac{\xi(1 + \beta\tan\theta)E_{y0}}{\tilde{k}^2(1 + \tan^2\theta) + (1 - \beta\tan\theta)^2} - \frac{\kappa^2 D_\perp^{amb}}{\beta^2}]$$

$$- \frac{D_\parallel^{amb}}{h^2} - 2\alpha n_0 . \qquad (4.25)$$

Here it is noted that the index of the iohomogenity κ shows the steepness of an arc; κ is positive for the northern slope of an arc and negative for the southern slope. Further, it is noted that the angle θ is measured from the west (positive x axis) toward the south.

Now consider the case in which the electric field is in the south direction, i.e., $E_{y0} > 0$. For the northern slope of an arc, i.e, $\xi > 0$ $(dn_0/dy > 0)$, we obtain after some manipulation as

$$\tilde{k}_m^2 \sim (E_{y0}/E_{c0})^{1/2},$$

$$\tan\theta_m \sim [(1 + \beta^2)^{1/2} - 1]/\beta \sim \frac{\beta}{2} \text{ for } \beta < 1, \qquad (4.26)$$

where the suffix m implies the maximum growth rate. The maximum growth rate Γ_m corresponding to relations (4.26) is approximately given by

$$\Gamma_m \sim \xi E_{y0} - \frac{D_{\parallel}^{amb}}{h^2} - 2\alpha n_0 - \frac{\kappa^2 D_{\perp}^{amb}}{\beta^2}(E_{y0}/E_{c0})^{1/2}. \qquad (4.27)$$

For the southern slope of an arc, i.e., $\xi < 0$, we have

$$\tilde{k}_m^2 \sim \beta^2 \left[(E_{y0}/E_{c0})^{1/2} - 3 \right],$$
$$\tan\theta_m \sim - \left[(1 + \beta^2)^{1/2} + 1 \right] / \beta \sim - \frac{2}{\beta} \quad \text{for } \beta < 1. \qquad (4.28)$$

The maximum growth rate corresponding to ralations (4.28) is given by

$$\Gamma_m \sim - \frac{\beta^2 \xi E_{y0}}{4} - \frac{D_{\parallel}^{amb}}{h^2} - 2\alpha n_0$$
$$- \kappa^2 D_{\perp}^{amb} [(E_{y0}/E_{c0})^{1/2} - 3]. \qquad (4.29)$$

Let us now evaluate these characteristic values. For example, we put that $|\kappa^{-1}| \sim 10$ km and that the other paramaters are the same as given in Sec. III. Then we have

$$\lambda_m \sim 1 \text{ km}, \quad \theta_m \sim 14^\circ \quad \text{and} \quad \Gamma_m \sim 0.04 \text{ sec}^{-1},$$

for the northern slope, and

$$\lambda_m \sim 2\ \text{km}, \quad \theta_m \sim -76^\circ \quad \text{and} \quad \Gamma_m \sim 10^{-3}\ \text{sec}^{-1},$$

for the southern slope.

From these results it can be said that an arc is deformed by the cross-field instability; its northern slope suffers from a rather small-scale irregularity which propagates roughly in the east direction with a speed of about the electron Hall speed and the southern slope is deformed in a very different way, though more slowly. A sketch of the deformed arc is illustrated in Fig. 4.13.

In reality the deformed auroral arcs exhibit complex forms, and hence several distortion machanism may be operative simultaneously. According to recent observations, Hallinan and Davis(1970) have attributed the most commonly observed curls to the Kelvin-Helmholtz instability.

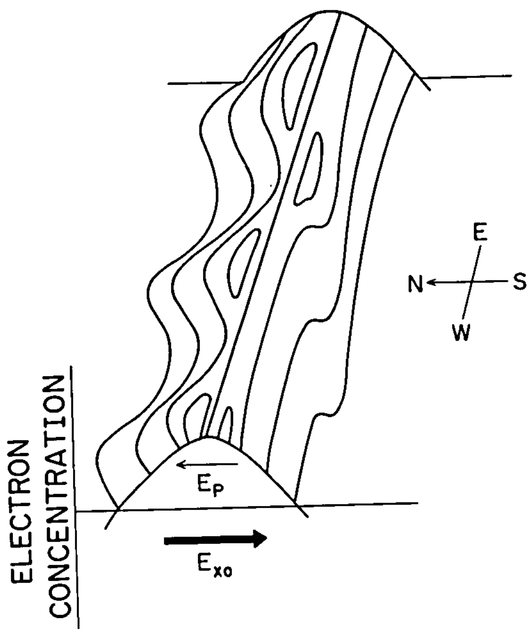

Fig. 4.13. Sketch of an arc deformed by the cross-field instability. Note that both sides of the arc suffers from deformation, though in a different fashion.

VI. Discussion and Conclusion

The main purpose of this paper is to point out a possibility that the ionospheric irregularities could be a seed of the multiple auroral arcs. First, we have shown that the ionosphere is not a specular but a bumpy (irregular) medium which is scratched by some plasma instability such as the cross-field instability. Then we have presented a mechanism that leads to enhance ent of the irregularities, and have numerically shown that they certainly develop into striped auroral arcs under certain assumptions.

One of the basic assumptions on which we relied is that the Kev electrons could be produced by a field-aligned current driven by the irregularity potential. The critical current, j_c, beyond which the ion waves are excited, may be in the following range:

$$nev_s \leq j_c \leq nev_{eT},$$

where v_s is the ion-sound velocity and v_{eT} is the electron thermal velocity; the upper limit correspond to the case of equal electron- ion temperature and the lower limit corresponds to the case of infinite electron-to-ion temperature ratio (Jackson, 1960). Assuming the equal electron-ion temperature, Swift(1965) gave the critical current such that

$$j_c = 3.8 \times 10^{-5} \ \mathrm{amp/m^2},$$

for $n = 10^9 m^{-3}$. This value may be the upper limit of the critical current. In the higher magnetosphere, the electron concentration n is expected to reduce by one or two orders. Further, the electron temperature may be much larger than the ion temperature during pre-break-up or recovery phases. In this case, the critical current reduces roughly by the square root of the proton-to-electron mass ratio, i.e., by about 40 times. Therefore, the minimum critical current may reduce to 10^{-8} amp/m^2.

The field-aligned current density j under consideration is roughly given by

$$j \sim eS_e \phi h.$$

When we put that $S_e \sim 10^5$ and $h \sim 50$ km, the current becomes roughly $10^{-9} \phi$ amp/m^2 (ϕ in volt). In this case the minimum potential for instability is given by

$$\phi \sim 10 \ \mathrm{V}, \quad \text{i.e.,} \ E_p \sim \phi / d \sim 5 \times 10^{-4} \ \mathrm{V/m}.$$

Since the induced field E_p is roughly given by $E_p \sim \varepsilon E_{x0}$, this value is quite understandable. It is likely, therefore, that the ion waves are excited by the field-aligned current under consideration. However, the question still remains whether the Kev electrons can with certainty be produced by such instability. Carlqvist and Boström(1970) have recently pointed out the possibility that the electric fields associated with space charges caused by intense field-aligned currents can produce Kev electrons.

Another basic assumption is that the Kev electrons are produced by the coming-down electrons alone, i.e., $\gamma_d \neq 0$ and $\gamma_u = 0$. In the above paragraph, attention was paid only to the current density in order to discuss the instability criterion. Strictly speaking, whether the instability takes place or not depends upon the speed of electrons. In other words, the ion waves are excited if the electron speed exceeds a certain critical speed. From this fact it is resonably inferred that the instability is more likely to take place in the sheets of coming-down electrons than those of going-up electrons. This is because the coming-down electrons may be composed of faster or hotter electrons than the going-up electrons of the ionospheric origin.

Alternatively, we may consider that the electrons in the magnetosphere are directly triggered by the (positive) irregularity potential and precipitate into the ionosphere. In these cases, we need not introduce any plasma instability in order to produce the Kev electrons. Further, the condition of $\gamma_d \neq 0$ and $\gamma_u = 0$ is automatically satisfied without any <u>ad hoc</u> assumptions. Such a situation may be realized in a case where the initial potential of ionospheric irregularity is large enough to control the high energy electrons.

It is reported that the thickness of a visible arc is typically 1 km (see, for example, Maggs and Davis, 1968). The thickness of the calculated (ionization) arcs, on the other hand, is broader than the observed results. However, this discrepancy is insignificant. The reasons are three-fold: First, recent observation of <u>quiet</u> arcs by Cloutier et al. (1970) shows that the thickness of the electrojet was about 10 km. The second reason is that, if the initial irregularity is localized, then it is expected that the arcs become narrower. In fact, nonlinear calculations of the cross-field instability (Tsuda et al., 1969; see also chapter 3 in this paper) indicate that the nonlinear waves have a tendency to localize. The third is as follows: In our analysis we have assumed that the precipitation is proportional to the potential ϕ. Actually, however, the ion waves may be excited only in a very restricted region corresponding to the peak potential where the intensity of field-aligned currents is strong. Therefore, it is expected that the region of precipitation is localized and hence the thickness of an arc is narrowed.

In the equivalent electric circuit shown in Fig. 4.2b, the effect of the capacitance across the magnetic field lines, namely, the polarization current, was not taken into account explicitly. If necessary, however, we can include this effect into the inductance in such a way as to reduce it. According to Dewitt(1968), the time constant CR for polarization of the magnetosphere is estimated to be roughly unity. Since ω is about 4×10^{-3} sec^{-1} for $\lambda_m = 30$ km and $V = 20$ m/sec, we have $\omega CR \sim 4 \times 10^{-3} \ll 1$. Therefore, we may neglect the magnetospheric capacitance C.

In calculations, we have assumed that all the parameters such as the resistance R and the frequency ω are constant throughout the evolution. In reality, this may not be true so they should be regarded as variables, since the situation changes as the irregularities evolve. Among the parameters, the variation of the resistance along the field lines may be significant. When a plasma instability sets in, the resistivity may increase. Such an anomalous resistivity has been considered by many authors (for instance, Buneman, 1959; Kadomtsev, 1965; Sagdeev and Galeev, 1969; Sizonenko and Stepanov, 1970). By using Buneman's formula, Swift(1965) estimated the anomalous conductivity $\tilde{\sigma}_{\parallel}$ in the magnetosphere to be 10^{-2} mho/m for $n = 10^9$ m^{-3}. This formula may be applicable in the regime of electron waves associated with Buneman's instability (two-stream instability). For ion wave instability, the conductivity may be somewhat less than this value. Using Sizonenko and Stepanov's formula, $\tilde{\sigma}_{\parallel}$ is estimated to be 10^{-3} mho/m for $n = 10^{8}$ m^{-3}. If we assume that the instability takes place over the distance of $L_{\parallel}$ along the field lines, the resistance along the field lines, $R_{\parallel}$, is given by

$$R_{\parallel} \sim \frac{1}{\sigma_{\parallel}} \frac{L_{\parallel}}{d} \frac{B}{B_0}$$

where B_o is the magnetic field intensity at the ionospheric level and B is the average intensity of the magnetic field under consideration. When we choose $L_{\parallel} \sim 10^{4}$ km, we have $R_{\parallel} \sim 1.3 \times (B/B_o)$ ohm. Since $(B/B_o) < 1$, we may regard that $R_{\parallel} \leq R \sim 0.4$ ohm. Thus, the increase of the resistivity due to instability may not be so significent as to change our results.

We further assumed immobile ions along the field lines. Strictly speaking, the ion currents must also be taken into account. Observations, however, suggest that the currents may be carried by electrons (Cloutier et al., 1970; Armstrong and Zmuda, 1970), so that the assumption of immobile ions may also be allowed.

The most distinctive feature of our model is the fine structure of field-aligned currents. Our model suggests that two equal anti-parallel field-aligned currents exist across an auroral arc (cf. case 2 of Boström, 1964). Cloutier et al.(1970) and Park and Cloutier(1971) have reported the exsistence of such anti-parallel sheet currents. This strongly supports the possibility of the proposed mechanism. Let us now evaluate the current density. The intensity of the induced field E_p in an arc may reach to that of the external field E_{x0} for an extremely developed arc; in that case the total field in the arc completely vanishes. Then the induced potential amounts to 300 V for $E_{xo} = 0.01$ V/m and $\lambda_m = 30$ km. In this case the field-aligned current becomes 3×10^{-7} amp/m^2 for $S_e \sim 10^5$ and 3×10^{-5} amp/m^2 for $S_e \sim 10^7$. Cloutier et al.(1970) estimated the intensity peak of the net field-aligned current to be 2×10^{-5} amp/m^2. Thus our model can fairly well account for the observation. However, the directions of the currents are inconsistent; in our model the upward current lies in the southern side of an arc, whereas it lies in the northern side in the observation. Haerendel(1970a, 1970b) explains that the case of Cloutier et al.(1970) may be a special case in which the external field is in the west direction. The coincidence of precipitated electrons with upward current sheet, rather than downward current sheet, is also in agreement with the prediction of our theory. Further, the thickness of the current sheets, roughly 5 km and 7 km, are coincident with our model. It is further worth noting that the downward sheet current consists of lower-energy electrons escaping from the ionosphere.

According to simultaneous observations of auroras at magnetically conjugated points (Belon et al., 1969), it is said that the auroras appear in both hemisphere having a good conjugacy, especially during quiet times. Our model is also not inconsistent with this conjugacy of auroras.

We have proposed and analyzed a new mechanism of multiple auroral arcs at rather quiet times. As a result, it is found that the ionospheric irregularities can develop into auroral arcs via field-aligned currents driven by the induced potential associated with the irregularities. The spacing of the arcs is determined by that of the irregularities. As a potential candidate capable of producing such irregularities in the ionosphere, attention is paid to the cross-field instability. Linear analysis has shown that the instability can certainly produce such irregularities that their spatial form fits the arc configuration. In addition, it is found that a developed arc is deformed by the cross-field instability.

Chapter 5

SUMMARY AND CONCLUSION

We have discussed the role of the cross-field instability as a formation mechanism of the density irregularities seen in irregularity-type sporadic E layers, artificial plasma clouds, auroral arcs, and even in laboratory experiments. Our main concern was the nonlinear aspects of the cross-field instability. By computer analysis, the nonlinear differential equations of a macroscopic fluid-type plasma were solved as an initial-boundary value problem. A good agreement between the computed results and the theory was found.

First, we have treated the one-dimensional, nonlinear cross-field instability. The instability condition was more strengthened compared with the previous works. As a result, we found strongly unstable waves, i.e., an explosive instability.

Second, the time evolution of the two-dimensional, nonlinear cross-field instability has been demonstrated. By this, the competing process between quasilinear and mode coupling effects was clarified, i.e., the background distributions of electric field and density were, more or less, deformed to result in the saturation of the amplitude of ubstable waves. This contrasts with the one-dimensional model in which the saturation is achieved only by the mode coupling. It was found that which deformation of the electric field and density distributions dominates might depend on the boundary condition. Another important result caused by the competition between quasilinear and mode coupling processes was that the system showed the cyclic growth and decay of waves.

Common features in the one- and two-dimensional models were as follows: When E_{ext} is below E_{c1} (critical electric field), the system behaves gently. In this case, two - dimensional model succeeded in obtaining the fully-developed turbulent state. On the other hand, when E_{ext} is far beyond E_{c1}, the system develops into strong turbulent state. Unfortunately, we had a numerical instability in this case. It is, however, easy to infer that very strong wave-wave interactions take place. The numerical instability may be due to the smallness of the number of harmonic waves taken in the computation.

In the ionosphere, it is controversial whether E_{ext} is beyond E_{c1} or not, because E_{c1} is the function of many ionospheric parameters of which we do not know the all values at this stage and is theoretically derived under some assumptions described previously. Therefore, we should regard E_{c1} as the rough measure beyond which the system becomes violent and large density irregularities are formed. Anyhow, we can expect the validity of our model as a cause of the ionospheric irregularities. The other supports of our two-dimensional model are two: One is the cyclic growth and decay of unstable waves as observed in artificial plasma clouds in the lower ionosphere. This was confirmed partly by our model. Another is the flattening of the density profile observed in laboratory experiments (reflex arcs). We could obtain the clear flattening of the density profile under the boundary condition pertinent to the laboratory experiments. It was also pointed out that the flattening of the potential profile may be more important in the ionosphere than in laboratories. This point may be clarified in the future by sounding rockets passing the sporadic E layers, for example.

From a view-point of plasma physics, nonlinear cross-field instability presents an attractive example of wave-wave interactions. We found that the waveforms became saw-tooth or soliton-like. This fact indicates that the system equation may approximately be reduced to the Burgers or Kortweg de Vries equation, respectively. The turbulent power spectrum of the density wave was approximately k^{-3} or softer in our cases, being consistent with the previous works in one-dimensional model. The energy exchange between the supplier and the consumer was also discussed: The energy from the background quantities (density gradient and external electric field), which sustain the instability, flows continuously to shorter wavelength components, while the part of the energy of unstable waves feeds back to the supplier. Thus, we could understand the dynamics of nonlinear wave-wave interactions, to some extent. We believe that this computational approach will contribute to the understanding of plasma turbulence, more or less.

The third part of this thesis was devoted to the application of the cross-field instability to the auroral ionospheric irregularities, i.e., auroral arcs which are most beautiful, dramatic phenomenon that man has ever found in the world. Our concern was a formation mechanism of auroral arcs in rather quiet times. This study was based on the idea that the auroral arcs may have their orogin in the ionosphere rather than in the magnetosphere in magnetically quiet times; that is to say, density fluctuations in the ionosphere grow resulting in a wavy irregularity of ionization by the action of the cross-field instability (1st stage), and thereafter such an irregularity (arc-to-be) develops into auroral arcs under the influence of field-aligned currents (Birkeland currents) triggered by an induced potential across an arc-to-be (2nd stage). Now, there is no doubt of the important relationship between field-aligned currents and auroral arcs, as has been observed by sounding rockets in quiet auroral arcs. The possibility of the cross-field instability in the formation of quiet auroral arcs is controversial. Of course, we cannot deny other possibilities which must be sought in the future. Nevertheless, we hope that this work gives a first step to the understanding of electrodynamic coupling between the ionosphere and the magnetosphere.

Appendix

Let us evaluate the stability criterion of an infinitesimal disturbance. To this end, it is first required that the steady-state solution be found. Since the governing Eq. (4.6) are nonlinear differential equations and, in addition, the boundary condition is not clear, it is difficult to find the exact solution. For the sake of mathematical tractability and without loss of generality, therefore, we assume a simple background distribution; the zero-order electric fields, E_{xo} and E_{yo}, external plus ambipolar, are constant and the zero-order electron concentration $n_o(y)$ increases toward the east with a constant rate κ, where $\kappa = d(\ln n_o)/dy$. These assumptions may be valid for short wave disturbance, namely, for $k \gg \kappa$. For the ionosphere of our concern, this condition is a posteriori satisfied (see Eq. (4.11)).

Under these assumptions, we shall impose upon the quiescent ionosphere an electrostatic disturbance such that

$$n = n_0(y) + \tilde{n}\exp(ik_x x + ik_y y - i\omega t),$$

$$E_x = E_{x0} - \frac{\partial}{\partial x}\tilde{\phi}\exp(ik_x x + ik_y y - i\omega t), \qquad \text{(A.1)}$$

$$E_y = E_{y0} - \frac{\partial}{\partial y}\tilde{\phi}\exp(ik_x x + ik_y y - i\omega t),$$

Upon substituting (A.1) into (4.6) and linearizing it, we obtain

$$[\, - i\omega - ik_x(\mu_H^{\pm}E_{y0} \mp \mu_p^{\pm}E_{x0}) + ik_y(\mu_H^{\pm}E_{x0} \pm \mu_p^{\pm}E_{y0})$$

$$+ D_{\perp}^{\pm} k^2 + \frac{D_{\parallel}^{amb}}{h^2} + 2\alpha n_0]\, \tilde{n}$$

$$+ [\, \pm\mu_p^{\pm}k^2 n_0 - i(\mu_H^{\pm}k_x \pm \mu_p^{\pm}k_y)\frac{dn_0}{dy}\,]\, \tilde{\phi} = 0, \qquad \text{(A.2)}$$

where $k^2 = k_x^2 + k_y^2$. From (A.2) the dispersion equation can easily be derived. The growth rate Γ $[= \mathrm{Re}(-i\omega)]$ is then obtained as

$$\Gamma = \frac{M\kappa k^2}{M_p^2 k^2(1 + \tan^2\theta) + (M_H - M_p\tan\theta)^2\kappa^2}$$

$$\times\{[(M_p - M_H\tan\theta)E_{x0} + (M_H + M_p\tan\theta)E_{y0}] + \frac{\kappa}{M_p}(D_{\perp}^{-} - D_{\perp}^{+})$$

$$\times(M_H - M_p\tan\theta)\} - 2\alpha n_0 - \kappa^2 D_{\perp}^{amb} - \frac{D_{\parallel}^{amb}}{h^2}\, . \qquad \text{(A.3)}$$

For the parameter set given in the text, we have

$$|E_{xo}| \sim 10^{-2} \gg \left|\frac{\kappa}{M_p}(D_{\perp}^{-} - D_{\perp}^{+})\right| \sim 5\times 10^{-9},$$

so that the diffusion term in the curly bracket can be neglected compared with the E_{xo} term. Accordingly, the growth rate Γ is approximately given by Eq. (4.7).

References

Akasofu, S.-I. and D.S. Kimball, J. Atmos. Terr. Phys. 26, 205(1964).

Akasofu, S.-I. znd S. Chapman, Phil. Trans. Roy. Soc. London A253, 359(1961).

Akasofu, S.-I., S. Chapman and P.C. Kendall, Aurora and Airglow (Ed. B.M. McCormac) pp.281, Reinhold, New York (1967).

Akasofu. S.-I., D.S. Kimball and C.-I. Meng, J. Atmos. Terr. Phys. 28, 627(1966).

Armstrong, J.C. and A.J. Zmuda, J. Geophys. Res. 75, 7122(1970).

Atkinson, G., J. Geophys. Res. 75, 4746(1970).

Belon, A.E., J.E. Maggs, T.N. Davis, K.B. Mather, N.W. Glass, and G.F. Hughs, J. Geophys. Res. 75, 1(1969).

Boström, R., J. Geophys. Res. 69, 4983(1964).

Boström, R., Annls. Geophys. 24, 681(1968).

Buneman, O., Phys. Rev. 115, 503(1959).

Carlqvist, P. and R. Boström, J. Geophys. Res.75, 7140(1970).

Chimonas, G., J. Geophys. Res. 74, 4091(1969).

Choy, L.W., R.L. Arnoldy, W. Potter, P. Kintner and L.J. Cahill, Jr., J. Geophys. Res. 76, 8279(1971).

Cloutier, P.A., H.R. Anderson, R.J. Park, R.R. Vondrak, R.J. Spiger and B.R. Sandel, J. Geophys. Res. 75, 2595 (1970).

Coppi, R., G. Lavel and R. Pellat, Phys. Rev. Lett. 16, 1207 (1966).

Cunnold, D.M., J. Geophys. Res. 74, 5709(1969).

Davis, J.R., J. Geophys. Res. 76, 5292(1971).

Dewitt, R.N., J. Geophys. Res. 73, 6307(1968).

Fejer, J.A., J. Geophys. Res. 68, 2147(1963).

Haerendel, G., MPI/PAE-Extraterr. 44/70 presented at Internat. Symp. on'Solar Terrestrial Physics' Leningrad, May 1970(1970a).

Haerendel, G., Private communication (1970b).

Hallinan, T.J. andT.N. Davis, Planet. Space Sci. 18, 1735(1970).

Hoh, F.C., Phys. Fluids 6, 1184(1963).

Hooper, E.B., Jr., Phys. Fluids 13, 96(1970); Plasma Phys. 12, 855(1970); ibid. 13, 1(1971).

Hooper, E.B., Jr. and J.C.G. Walker, J. Atmos. Terr. Phys. 33, 1441(1971).

Hooper, E.B., Jr. and S.M. Girvin, J. Appl. Phys. 42, 4832 (1971).

Jackson, E.A., Phys. Fluids 3, 786(1960).

Kato, S., J. Atmos. Terr. Phys. 27, 373(1965); Radio Sci. 7 (to appear in March issue, 1972).

Kato, S. and Y. Hirata. Rept, Ionosp. Space Res. Japan 21, 85(1967).

Kadomtsev, B.B., Plasma Turbulence, Academic Press, New York (1965).

Kern, J.W., J. Geophys. Res. 67, 2649(1962).

Kim, J.J. and A. Simon, Phys. Fluids 12, 895(1969).

Linson, L.M. and J.B. Workman, J. Geophys. Res. 75, 3211(1970).

Maeda, K., T. Tsuda and H. Maeda, Rept. Ionosp. Space Res. Japan 17, 147(1963).

Maggs, J.E. and T.N. Davis, Planet. Space Sci. 16, 205(1968).

Martyn, D.F., Proc. IRE. 47, 147(1959).

Morse, D.L., Phys. Fluids 8, 1339(1965).

Ogawa, T. and T. Sato, Planet. Space Sci. 19, 1393(1971).

Oya, H., J. Geomag. Geoele. 19, 267(1967).

Park, R.J. and P.A. Cloutier, J. Geophys. Res. 76, 7714(1971).

Prakash, S., S.P. Gupta and B.H. Subbaraya, Planet. Space Sci. 18, 1307(1970).

Rao, P.B. and W.H. Russell, Radio Sci. 6, 221(1971).

Reid, G.C., J. Geophys. Res. 73, 1627(1968).

Sagdeev, R.Z. and A.A. Galeev, Nonlinear Plasma Theory pp.94, Benjamin, New York (1969).

Sato, T., J. Geophys. Res. 73, 2941(1968).

Sato, T., Phys. Fluids 14, 2426(1971).

Sato, T. and T. Tsuda, Phys. Fluids 10, 1262(1967) (Erratum 11, 259(1968)).

Sato, T. and T. Tsuda, Conf. Proc. 2nd Seminar on Cause and Structure of Temperate Latitude Sporadic-E, ESSA Research Laboratory, Boulder, Colo. (1968).

Sato, T. and T. Ogawa, J. Geophys. Res. 77, 1994(1972).

Sato, T., T. Tsuda and K. Maeda, Radio Sci. 3, 529(1968).

Sato, T. and T. Tsuda, Radio Sci. 7 (to appear in March issue, 1972).

Sato, T., T. Ogawa and Y. Matsuda, Phys. Fluids 15, in press (1972).

Schield, M.A., J.W. Freeman and A.J. Dessler, J. Geophys. Res. 74, 247(1969).

Sizonenko, V.L. and K.N. Stepanov, Nucl. Fusion 10, 155(1970).

Simon, A., Phys. Fluids 6, 382(1963).

Smith, L.G., Radio Sci. 1, 178(1966).

Swift, D., J. Geophys. Res. 70, 3061(1965).

Tsuda, T. and T. Sato, Phys. Fluids 11, 677(1968).

Tsuda, T., T. Sato and K. Maeda, Radio Sci. 1, 212(1966).

Tsuda, T., T. Sato and S. Matsushita, J. Geophys. Res. 74, 2923(1969).

Vondrak, R.R., H.R. Anderson and R.J. Spiger, J. Geophys. Res. 76, 7701(1971).

Wescott, E.M., J.D. Stolarik and J.P. Heppner, J. Geophys. Res. 74, 3469(1969).

Whitehead, T.D., J. Atmos. Terr. Phys. 29, 1285(1967); ibid 30, 1563(1968); Rev. Geophys. Space Phys. 8, 145(1970a); J. Atmos. Terr. Phys. 32, 1283(1970b); J. Geophys. Res. 76, 3116(1971).

Williams, R.H. and J. Weinstock, J. Geophys. Res. 75, 7217(1970).